Publication Year	2021
Acceptance in OA	2025-03-17T11:24:36Z
Title	Turbulence transport in the solar corona: Theory, modeling, and Parker Solar Probe
Authors	Zank, G. P., Zhao, L. L., Adhikari, L., TELLONI, Daniele, Kasper, J. C., Bale, S. D.
Publisher's version (DOI)	10.1063/5.0055692
Handle	http://hdl.handle.net/20.500.12386/36847
Journal	PHYSICS OF PLASMAS
Volume	28

REVIEW ARTICLE | AUGUST 03 2021

Turbulence transport in the solar corona: Theory, modeling, and Parker Solar Probe

Special Collection: Papers from the 62nd Annual Meeting of the APS Division of Plasma Physics , Reviews and Tutorials in Heliospheric and Astrophysical Plasmas

G. P. Zank ; L.-L. Zhao ; L. Adhikari; D. Telloni ; J. C. Kasper ; S. D. Bale

Phys. Plasmas 28, 080501 (2021)
https://doi.org/10.1063/5.0055692

Physics of Plasmas REVIEW scitation.org/journal/php

Turbulence transport in the solar corona: Theory, modeling, and Parker Solar Probe

Cite as: Phys. Plasmas **28**, 080501 (2021); doi: 10.1063/5.0055692
Submitted: 1 May 2021 · Accepted: 12 July 2021 ·
Published Online: 3 August 2021

G. P. Zank,[1,a),b)] L.-L. Zhao,[2] L. Adhikari,[3] D. Telloni,[4] J. C. Kasper,[5] and S. D. Bale[6]

AFFILIATIONS

[1] Center for Space Plasma and Aeronomic Research (CSPAR) and Department of Space Science, The University of Alabama in Huntsville, Huntsville, Alabama 35805, USA
[2] Department of Space Science, The University of Alabama in Huntsville, Huntsville, Alabama 35805, USA
[3] Center for Space Plasma and Aeronomic Research (CSPAR), The University of Alabama in Huntsville, Huntsville, Alabama 35805, USA
[4] National Institute for Astrophysics Astrophysical Observatory of Torino Via Osservatorio 20, I-10025 Pino Torinese, Italy
[5] BWX Technologies, Inc., Washington, DC 20002, USA and Department of Climate and Space Sciences and Engineering, University of Michigan, Ann Arbor, Michigan 48109, USA
[6] Physics Department, University of California, Berkeley, California 94720-7300, USA

Note: This paper is part of the Special Collection: Papers from the 62nd Annual Meeting of the APS Division of Plasma Physics.
Note: Paper BI1 1, Bull. Am. Phys. Soc. **65** (2020).

[a] Invited speaker.
[b] **Author to whom correspondence should be addressed:** garyp.zank@gmail.com

ABSTRACT

A primary goal of the Parker Solar Probe (PSP) Mission is to answer the outstanding question of how the solar corona plasma is heated to the high temperatures needed for the acceleration of the solar wind. Various heating mechanisms have been suggested, but one that is gaining increasing credence is associated with the dissipation of low frequency magnetohyrodynamic (MHD) turbulence. However, the MHD turbulence models come in several flavors: one in which outwardly propagating Alfvén waves experience reflection from the large-scale flow and density gradients associated with the solar corona, and the resulting counterpropagating Alfvén waves couple nonlinearly to produce quasi-2D turbulence that dissipates and heats the corona, thereby driving the solar wind. The second approach eschews a dominant outward flux of Alfvén waves but argues instead that quasi-2D turbulence dominates the lower coronal plasma and is generated in the constantly upwelling magnetic carpet, experiencing dissipation as it is advected through the corona and into the solar wind, yielding temperatures in the corona that exceed a million degrees. We review the two turbulence models, describe the modeling that has been done, and relate PSP observations to the basic predictions of both models. Although PSP measurements are made in the super-Alfvénic solar wind, the observations are close to the coronal region, thus providing a glimpse into the likely properties of coronal turbulence. Observations of low-frequency MHD turbulence by PSP in the super-Alfvénic solar wind allow us to place constraints on models of the turbulently heated solar corona that drive the supersonic solar wind.

I. INTRODUCTION

The Parker Solar Probe (PSP), launched in August 2018 and designed to reach a radial distance of $\sim 10R_\odot$ (solar radius) above the solar surface,[1] has completed seven orbits around the Sun. The outstanding question of how the solar corona is heated and the solar wind accelerated is central to the PSP mission.[2,3] The solar wind is classified typically into two classes according to the plasma flow velocity observed at 1 astronomical unit (au): fast solar wind with a velocity $\geq$ 500 km/s and slow solar wind with a velocity $\leq$ 500 km/s. It is generally accepted that the fast solar wind originates from coronal holes with open magnetic field lines, but the origin of slow solar wind streams is still debated.[4,5] Central to the coronal heating problem, whether in fast or slow wind, is the transport of waves and turbulence beyond the photosphere. Several models for heating the solar corona and the subsequent driving of the solar wind have been advanced, the two most popular being the dissipation of low frequency magnetohydrodynamic (MHD) turbulence or the dissipation of ion cyclotron waves. The MHD turbulence models can be further distinguished by a two class classification of the physical models as introduced by Cranmer and van Ballegooijen.[6] The first is described as "wave/turbulence-driven" (W/T-) models and the other as "reconnection/loop-opening" (RLO-) models.

PSP is currently measuring plasma and magnetic fields above the Alfvén surface. Although these measurements are made in the super-Alfvénic solar wind, the observations bring us closer to the surface of the Sun than ever before, thus providing us with our best glimpse so far into the likely properties of coronal turbulence. As we describe below, observations of low-frequency MHD turbulence by PSP allow us to now begin constraining models of the turbulently heated solar corona that drives the supersonic solar wind. These models postulate a source of turbulence at a base location, perhaps just above the photosphere or, more typically for wave-turbulence models, just above the chromosphere. By modeling the evolution of MHD turbulence in the corona, through the Alfvén surface, and into the supersonic solar wind (identifying further possible *in situ* sources of turbulence), the constraints inferred from PSP observations can now be applied to the models. Although preliminary, these new observational constraints on the models already shed considerable light upon the origin of coronal and solar wind turbulence, the heating of coronal plasma, and the origin of the fast and slow solar wind.

This motivates us, in this Review, to focus on the possible turbulence mechanisms thought to be responsible for the heating of the solar corona and hence the driving of the fast and slow solar wind. We do not focus extensively on the underlying theory as much as we discuss observational signatures revealed by PSP that may allow us to distinguish between the various turbulence models of coronal heating and solar wind driving. Two sets of observations identify a central conundrum for the turbulence models that has to be addressed. The first is that in highly magnetic field-aligned solar wind flows near 1 au, Wang *et al.*[7] and Telloni *et al.*[8] found that Alfvén waves were propagating uni-directionally (normalized cross-helicity $|\sigma_c| \simeq 1$) and that the spectrum was a power law with spectral index $-5/3$, i.e., $k_\parallel^{-5/3}$, where $k_\parallel$ is the wave vector parallel to the mean magnetic field. Second, Zhao *et al.*[9] reported Parker Solar Probe observations identifying highly magnetic field-aligned coronal flows that exhibited uni-directionally propagating Alfvén waves with a corresponding Kolmogorov-like spectrum $k_\parallel^{-5/3}$. Of course, uni-directionally propagating Alfvén waves do not interact nonlinearly, requiring counterpropagating Alfvén waves for a nonlinear cascade in wave number space to occur, and hence there should not be a Kolmogorov-like spectrum for uni-directionally propagating Alfvén waves nor should there be any related dissipation of Alfvén waves and hence heating of the solar wind or solar corona. Resolving this puzzle is essential if turbulence models are argued to be responsible for the heating of the solar corona and hence driving of the solar wind.

We discuss below two turbulence models advanced to explain the heating of the solar corona and draw particular attention to the conundrum outlined above. We further take the view that the slow wind and fast wind are both subject to the same underlying heating mechanism but that the geometry of the large-scale magnetic fields (open coronal holes and large-scale loops) mediates the nature of the wind in important ways. Illustrated in Fig. 1 is a cartoon showing one perspective of the expansion of (left) the fast solar wind from the base of a coronal hole and (right) the slow solar wind from higher up in the corona. In both cases, as we describe, the mechanism heating the open coronal hole plasma and the loop plasma is the same but the processes by which the plasma eventually forms the wind are different.

The W/T-model advanced originally by Matthaeus *et al.*[10] assumes that a broad spectrum of low-frequency MHD Alfvén waves carries kinetic and magnetic energy from the photosphere into the solar corona. The waves are generated by rapid displacements of open magnetic flux tubes that are advected by motion in the photosphere. An important concern is the difficulty that Alfvén waves have in propagating from the chromosphere, across the transition region, into the

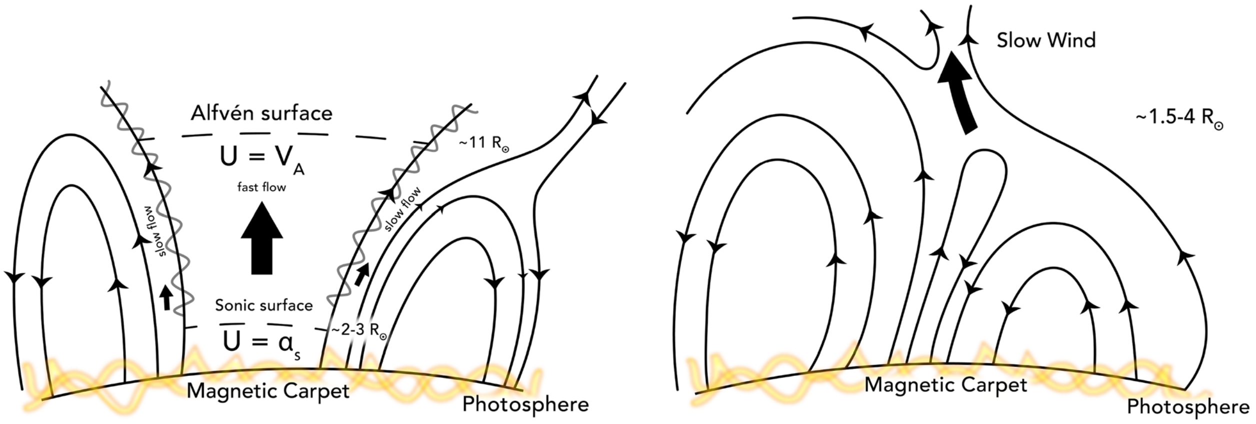

FIG. 1. Left: cartoon illustrating the possible origin of the fast solar wind from a coronal hole driven by turbulence associated with the magnetic carpet. Additional sources of turbulence in the corona, below and above the Alfvén surface, may be due to Kelvin–Helmholtz instabilities on the edges of coronal regions that separate fast coronal flows from adjacent slow flows associated with closed magnetic field regions as illustrated. The sonic and Alfvén surfaces are identified, i.e., surfaces at which the coronal flow transitions from subsonic to supersonic and sub-Alfvénic to super-Alfvénic, respectively. Right: a possible model describing the origin of the slow solar wind. Large-scale loop plasma is heated via turbulence associated with the magnetic carpet, and interchange reconnection at higher altitudes, possibly 2–5 $R_\odot$ above the photosphere, leads to the release of hot loop plasma. The hot plasma expands into higher open magnetic field coronal regions to reach supersonic and super-Alfvénic speeds thereafter.

corona. Since $\ll 1\%$ of the incident Alfvénic flux [perhaps as little as $4 \times 10^{-2}\%$ (Refs. 11–14)—see below] is thought to be transmitted across the transition region, this requires extremely high Alfvén wave fluxes emanating from the photosphere. Once through the transition region, the upwardly propagating Alfvén waves in W/T models experience partial non-Wentzel-Kramers-Brillouin (WKB) reflection off the large-scale density and magnetic field gradients of the solar corona and the counterpropagating Alfvénic modes interact nonlinearly to generate quasi-2D fluctuations that cascade to smaller scales and eventually dissipate, thus heating the coronal plasma.

An alternative turbulence model, described as quasi-2D turbulence models, identifies the "magnetic carpet,"[15] a region of both open and closed magnetic fields that is distributed uniformly across the solar surface, as the source of predominantly quasi-2D MHD turbulence that acts to heat the solar corona. The mixed polarity small-scale loops that form the magnetic carpet rise from below the photosphere and interact on a replenishment timescale of about 40 h.[15] Interspersed with the small-scale loops in the magnetic carpet are large-scale magnetic field lines, which could either be open as in coronal holes or closed as with large coronal loops. The constant stirring and mixing of the magnetic carpet loops generate small-scale quasi-2D turbulence above the photosphere[16] through the interaction of emerging and evolving carpet magnetic field. Zank *et al.*[17] argued that quasi-2D turbulence[18,19] generated by the magnetic carpet is advected through the chromosphere, across the transition region without reflection, and into the solar corona. Quasi-2D advected turbulence obviously does not suffer the losses that a corresponding flux of Alfvén waves would experience across the transition region. The dissipation of the quasi-2D turbulence is shown to be sufficient to heat the underlying plasma to temperatures in excess of 10^6 K. They argue that the basic mechanism for coronal heating via the dissipation of quasi-2D advected turbulence applies to both the fast wind and slow solar wind. The fast wind is heated by the dissipation of quasi-2D turbulence originating from the magnetic carpet and is advected by the heated expanding coronal flow.

Remote observations offer some general if inconclusive insights into the two classes of turbulence models for the solar corona. The transverse displacement of spicules in the chromosphere with amplitudes of 10–25 km/s and periods 100–500 s was observed by De Pontieu *et al.*,[20] for which they estimated an energy flux of $\sim$100 W m^{-2}. These fluctuations were interpreted as Alfvén waves with energy flux "sufficient to drive the solar wind,"[20] but this interpretation was disputed by Ref. 21 who favored an interpretation as kink modes. The debate has not been settled by either further observations[22–27] or further theory, modeling, and analysis.[28,29] Indeed, estimates for the energy content and flux of the waves are highly uncertain observationally.[30–35] Finally, note that waves with periods greater than $\sim$30–100 s are thought not to propagate energy efficiently from the coronal base.[12,13,36]

Zank *et al.*[17] estimated the observed magnitude of quasi-2D turbulent magnetic field fluctuations in an effort to determine whether there is sufficient energy to power coronal heating in polar coronal holes. In the center of a polar coronal hole, the unperturbed magnetic field is very nearly radial, and at $1.03R_\odot$ (i.e., $0.03R_\odot$ above the surface), its strength is about 10 G. The upward energy flux required at $1.03R_\odot$ to sustain coronal heating above this height along the radial field in the center of a polar coronal hole is about 3×10^5 erg cm^{-2} s^{-1}.[37] Averaged over several hours, the outflow speed of the corona at $1.03R_\odot$ in a polar coronal hole is no more than 10 km s^{-1}. On assuming a 10 km s^{-1} outflow at $1.03R_\odot$, if an energy flux of 3×10^5 erg cm^{-2} s^{-1} in magnetic field fluctuations ($B_\perp$) orthogonal to the average radial field is to be carried into the corona above, then a $B_\perp$ of about 1.9 G is required. This implies that the total field vector at $1.03R_\odot$ undergoes angular deviations of about 11° around the radial direction. De Pontieu *et al.*[20] and Moore *et al.*[38] reported oscillatory swaying motions of the open field with amplitudes of order 15° and periods of about 5 min at $1.03R_\odot$ in polar coronal holes. These observations correspond to a $B_\perp$ of 2.7 G, suggesting that there is sufficient magnetic energy flux corresponding to perpendicular magnetic field components to heat the solar corona and possibly drive the solar wind.

An interesting alternative for the origin of 2D turbulence that might be advected through the transition region derives from the reflection of Alfvén waves at the transition layer. Recall[11–14] that if the density changes discontinuously from the chromosphere to the corona by a factor of $r_d \sim 10^{-8}$ within $1\text{–}2 \times 10^3$ km, the transmitted Alfvén flux[11,14] $\sim 4\mathscr{F}_A\sqrt{r_d} \sim 4\mathscr{F}_A \times 10^{-4}$ for an incident flux $\mathscr{F}_A$. For $\mathscr{F}_A \simeq 10^8$ ergs cm^{-2} s^{-1} (which may be a somewhat high value for Alfvénic fluctuations $>10^3$ km—see Mullan[14]), this implies a transmitted flux $<4 \times 10^4$ ergs cm^{-2} s^{-1}, which is less than 5×10^5 ergs cm^{-2} s^{-1} required to heat the corona to the necessary temperature to drive a supersonic solar wind.[17,37] However, the Alfvén flux reflected at the transition region is now counterpropagating with respect to the upward flux, thereby initiating a nonlinear cascade that generates 2D zero frequency nonpropagating modes below the transition region. For an incident flux $\mathscr{F}_A$ as high as 10^8 ergs cm^{-2} s^{-1}, approximately 9.996×10^7 ergs cm^{-2} s^{-1} will be reflected and propagate counter to the incident Alfvén flux. The nonlinear interaction between the counter propagating Alfvénic fluxes will generate zero-frequency nonpropagating quasi-2D fluctuations. Taking conservatively a generation rate for 2D turbulence of just 1% of the counterpropagating slab turbulence, this process could well yield a flux of 2D magnetic turbulence that exceeds 10^6 ergs cm^{-2} s^{-1} being advected across the transition region into the corona.[39] This may be an alternative source of quasi-2D turbulence at the base of the corona.

As discussed in detail in Sec. III, a model invoking a dominant quasi-2D turbulent component[17,40] accelerates the solar wind to supersonic speeds within 2–4 $R_\odot$, consistent with observations,[41,42] and to super-Alfvénic speeds within $\sim$10–11 $R_\odot$. Further factors that need to be incorporated into this model are super-radial expansion and the possibility that the supersonic and super-Alfvénic flows in the coronal hole initiate possible Kelvin–Helmholtz instabilities along the boundaries of a coronal hole that separates faster and slower coronal flows. The already accelerated solar wind may be further accelerated by the dissipation of Kelvin–Helmholtz turbulence generated on the boundaries of the coronal hole.

The solar wind originating from coronal holes is likely to be highly aligned with the large-scale open radial magnetic field, making it observationally difficult to identify quasi-2D turbulence. Instead, the turbulence is likely to present itself as essentially slab turbulence i.e., turbulence composed of counterpropagating Alfvén waves. According to the basic W/T model[10] and extensions thereof,[43–57] the normalized cross helicity σ_c (the difference between the forward and backward Elsässer energies normalized to the total Elsässer energy) should be small to ensure that nonlinear interactions generate quasi-2D fluctuations[58] that then undergo a rapid 2D ($\mathbf{k}_\perp$, relative to the mean magnetic field) turbulent cascade that dissipates energy and heats the plasma. However, if the normalized cross helicity $|\sigma_c| \sim 1$, i.e., uni-directionally propagating Alfvén waves, then no turbulent interactions are possible within the W/T framework. However, the nearly incompressible (NI) MHD model in the small and $O(1)$ plasma beta regime admits uni-directional Alfvén wave propagation, and the Alfvén waves interact passively with the advected quasi-2D fluctuations to produce a $k_\parallel^{-5/3}$ wave number spectrum.[19] This is a key observational discriminator between the W/T and the quasi-2D turbulence models of solar coronal turbulence when the flow is highly aligned with the magnetic field.

A possible origin of the slow solar wind is illustrated in the right panel of Fig. 1. In this model, the quasi-2D turbulence generated by the magnetic carpet in the footpoints of a large magnetic loop heats the loop plasma in much the same way as the heating of coronal hole plasma occurs. However, the heating generates counterpropagating flows that cannot escape the loop, and the loop plasma is therefore heated to high temperatures. As illustrated, the loop plasma can escape into the high corona via interchange reconnection, at heights of perhaps $\sim$2–4 $R_\odot$. The hot escaping plasma forms the slow solar wind as it finds its way out of the upper corona through higher open field regions. This is basically the mechanism suggested by Fisk *et al.*[59,60] for the origin of the slow solar wind, although here incorporating the dissipation of quasi-2D turbulence as the loop heating mechanism. Such a model of the slow solar wind predicts a majority quasi-2D component and a minority slab component that should be relatively easily observed since the flows are unlikely to be highly aligned with the mean magnetic field.[61] By contrast, it is possible for the W/T model to heat the loop plasma since counterpropagating Alfvén waves will be generated at either end of a coronal loop. Indeed, Nigro *et al.*,[62,63] both theoretically and via reduced MHD simulations, found that fluctuations with a large perpendicular wave vector component can be generated in a loop by nonlinear interactions of counterpropagating Alfvénic fluctuations resulting in low cross-helicity values. Under these circumstances, with the opening of the loop via interchange reconnection, the hot loop plasma will expand as described already, but the dominant magnetic turbulence component will be slab, with a cross helicity $\sigma_c \simeq 0$, and not the quasi-2D component. As with the fast solar wind, two clearly distinct and testable predictions emerge from the NI MHD quasi-2D model and the W/T model: the former predicts a majority quasi-2D component and a minority slab component and the latter a majority slab component (with σ_c relatively close to although not necessarily 0) and a minority quasi-2D component. We note that if the slow wind happened to be highly field-aligned, the observed turbulence would appear to be slab or highly Alfvénic and could even have high values ($|\sigma_c| \sim 1$) of the normalized cross helicity (uni-directional Alfvén wave propagation) and have a parallel wave number spectrum of the Kolmogorov form. In support of this perspective, we recall the very interesting results presented by D'Amicis *et al.*[61,64] reporting observations of Alfvénic slow wind streams that possess a high cross-helicity value and a Kolmogorov-like spectrum. In Fig. 5 (bottom panel),[61] they show a correlation between θ_{BR} and V_{sw} that is almost identical to that in the fast wind (Fig. 5, top panel). Essentially, D'Amicis *et al.*[61] found that the observed slow wind is field-aligned, possesses high cross helicity, and yet has a Kolmogorov-like spectrum. Their result corresponds to the results presented by Telloni *et al.*[42] and Zhao *et al.*[9] for fast field-aligned flows. Matteini *et al.*[65,66] reported related results for fast wind. The important point is that both the slow wind and fast wind were field-aligned during the time these three sets of observations were made, and for this reason, only Alfvénic observations can be observed (the 2D component not being easily visible to a single spacecraft in this geometry). The observation of Kolmogorov-like spectra in such flows with a high cross helicity can be explained by NI MHD in the $\beta \ll 1$ or $O(1)$ limits thanks to a passive scalar-like interaction of uni-directionally propagating Alfvén waves with advected quasi-2D turbulence that results in a $k_\parallel^{-5/3}$ spectrum,[19] i.e., NI MHD generates a $k_\parallel^{-5/3}$ spectrum dynamically from uni-directionally propagating Alfvén waves. This stands in contrast to the W/T model which cannot do so. Such observations would therefore favor the NI MHD quasi-2D model rather than the W/T model.

Adhikari *et al.*[67] published an interesting paper entitled "Does turbulence turn off at the Alfvén critical surface?" that is germane to the discussion here. They examined two turbulence models in the vicinity of the Alfvén surface, the one underlying the W/T model and the other the NI MHD model in the plasma beta $\beta \ll 1$ or $O(1)$ limits. In essence, the W/T model predicts that at the Alfvén surface[67]

1. only outwardly propagating modes exist;
2. the velocity and magnetic field fluctuations are perfectly correlated, with equal velocity and magnetic field fluctuation correlation lengths; and
3. the nonlinear and dissipation terms are zero. Since these terms describe the transfer of large-scale energy to small scales, no transfer of energy occurs, suggesting that turbulence "turns off" at the Alfvén surface for the W/T model.

Within the W/T model, the Alfvén surface therefore acts to produce a "fossil"-like turbulence state shortly after the solar wind flow crosses the surface, "filtering" out all the backward propagating Alfvén modes, leaving only outwardly propagating modes. An important question is what the spectrum of the transmitted/filtered outwardly propagating Alfvén modes might be. If fossil turbulence, then if one follows the argument of Dobrowolny *et al.*[68,69] (see also Zank *et al.*[19,70]) it is possible that the spectrum transmitted across the Alfvén surface would be Kolmogorov-like for the outwardly propagating modes just below the Alfvén surface, provided the wave–wave couplings are governed by the nonlinear timescale and not the Alfvén timescale (see Appendix B of Zank *et al.*[70]). It is unclear how long such a superposition of linear Alfvén modes will retain a Kolmogorov-like spectrum as they propagate further into the super-Alfvénic solar wind in the absence of dynamical nonlinear couplings. Quasi-linear theory would suggest that resonant scattering of ions by Alfvén waves would result in a k^{-2} spectrum.[71] The continued expansion of the solar wind will lead eventually to the generation of (now advected) backward propagating Alfvénic modes that can "restart" nonlinear interactions and hence turbulence.

By contrast, the NI MHD $\beta \ll 1$ or $O(1)$ turbulence model predicts that at the Alfvén surface

1. the majority quasi-2D component is not subject to a critical point, although the Alfvén surface does represent a critical point for the minority slab turbulence component;
2. higher-order slab turbulence, like the W/T model, reduces to only outwardly propagating modes, with the slab turbulence

velocity and magnetic field fluctuations perfectly aligned and having equal velocity and magnetic fluctuations correlation lengths;

3. despite only outwardly propagating higher-order slab turbulence modes existing, the nonlinear dissipation term is nonzero because the dissipation of slab turbulence in the NI MHD description is due primarily to mixing with the dominant quasi-2D turbulence component;
4. both outward and inward nonpropagating modes of the dominant quasi-2D component are transmitted, and the corresponding velocity and magnetic field fluctuations are not perfectly correlated; and
5. the total nonlinear/dissipation terms are nonzero, ensuring that energy is transferred through the inertial range to eventually be dissipated, implying that turbulence in the plasma beta regime $\beta \ll 1$ or $O(1)$, as described by NI MHD, does not turn off at the Alfvén critical surface.

Consequently, NI MHD turbulence in the $\beta \ll 1$ or $O(1)$ regimes remains active and dominated by nonlinear interactions associated with the dominant quasi-2D component at and beyond the Alfvén surface. Furthermore, because of the interaction between quasi-2D structures and uni-directionally propagating Alfvénic modes, the minority slab turbulence also remains active at and beyond the Alfvén surface.

It is useful to list a set of the basic predictions from the NI quasi-2D models and those from the W/T models that can be tested by observations made by the Parker Solar Probe during its first set of encounters. Since PSP at the time of writing has not yet crossed below the Alfvén surface and is therefore making observations in the super-Alfvénic solar wind, the predictions below apply only to this region. Observationally, we stress that measuring spectral anisotropy and anisotropic structures is difficult when solar wind and coronal flows are highly aligned with the magnetic field, thereby preventing the observation of quasi-2D structures.[9,19] The NI quasi-2D models predict[18,19] for super-Alfvénic flows

1. that the energy-containing range in both the slow wind and fast wind is a superposition of a majority quasi-2D component and a minority slab component, likely in the ratio of 80:20;
2. that the inertial range is similarly anisotropic in both the slow wind and fast wind with a corresponding majority quasi-2D component and a minority slab component.
3. An arbitrary (normalized) cross-helicity for both the majority and minority component in both the slow wind and fast wind. For highly field-aligned flows, whether in the fast wind or even in slow wind, it is possible that uni-directional (i.e., with high normalized cross-helicity values $|\sigma_c| \simeq 1$) Alfvén wave/slab propagation exhibiting a $k_\parallel^{-5/3}$ spectrum can occur.
4. Arbitrary values of the (normalized) residual energy σ_r, including evolving toward -1, i.e., magnetic energy dominated, or $+1$, i.e., vortex-dominated, in the majority 2D component;
5. that the density fluctuations are primarily advected entropy fluctuations that behave as a passive scalar (a slow and fast mode wave contribution enters only at the higher order), have an amplitude that is ordered roughly by the turbulent Mach number $M \equiv \delta u / C_s$, where δu is a characteristic velocity of the turbulent fluctuations and C_s is the characteristic sound speed, and that the density variance spectrum is $k^{-5/3}$.

By contrast, the W/T models predict[10,48]

1. that the turbulence in the energy-containing range is primarily slab with a minority 2D component generated by the interaction of counterpropagating Alfvén waves for both the fast wind and slow wind;
2. that the inertial range is either isotropic or possibly possesses a Goldreich–Sridhar scaling;[72]
3. that the cross helicity for both fast wind and slow wind is small since counterpropagating Alfvén waves are essential to ensure the turbulent cascade of energy to small scales, and uni-directional Alfvén/slab propagation with a $k_\parallel^{-5/3}$ spectrum is not in general possible unless observations are made close to and just above the Alfvén surface. If the cross helicity is large, then turbulence is no longer operative within the context of the W/T model and can be regarded as fossil turbulence with the spectrum corresponding to a superposition of linear modes, possibly described by quasi-linear theory;
4. that the residual energy for both the fast wind and slow solar wind should be close to zero since the turbulence is primarily slab, and
5. nothing about density fluctuations, at least not in the standard W/T models, although Lithwick and Goldreich[73] suggest that slow mode waves may be responsible for density fluctuations.

Before concluding this section, we recall that the dissipation of a spectrum of ion cyclotron waves created at the base of the solar corona has been advanced as another possible mechanism for the heating of the solar corona. The spectrum of ion cyclotron waves is regarded as a static, linear, noninteracting superposition of waves. Ion cyclotron heating is also sometimes described as a "cyclotron sweep mechanism" and was addressed critically by Leamon *et al.*[74] The dissipation rate of the cyclotron sweep mechanism depends on the local proton (or minor ion) cyclotron frequency, which decreases with increasing heliocentric distance. Outward propagating fluctuations are transported into regions for which damping occurs at progressively lower frequencies. As a consequence, the linear dissipation of the fluctuations results in the absorption of energy at the local gyrofrequency. Linear dissipation of the wave spectrum therefore corresponds to a "sweep" through spectral space toward lower frequencies, thereby depleting the spectrum. Such a depletion of the wave spectrum will occur at even lower frequencies if minor or heavy ions are included in the dissipative process, with the consequence that the wave spectrum will already be partially depleted before the protons even experience heating.[75] A further and critical problem with the ion cyclotron heating mechanism[74] is that a large wave energy flux at high frequencies, up to perhaps the kilohertz range, is required to account for rapid cyclotron damping in the lower corona.[10] It is unclear whether there is a large enhancement of kHz power at the coronal base as this has not been observed. Furthermore, there is the obvious question of how such high-frequency waves in the lower solar corona could be generated.[76] Another significant problem facing the ion cyclotron dissipation mechanism is that the cascade in the parallel wavenumber direction is very slow. Hence, the spectrum dissipated by ion cyclotron resonance is unlikely to be replenished quickly enough to ensure rapid heating of the coronal plasma within 1–4 $R_\odot$. Finally, high-frequency modes experience only weak nonlinear couplings and weak WKB reflections.[10] High-frequency, parallel-propagating Alfvén waves are therefore transported rapidly through the corona, experiencing only direct kinetic damping.[13,77] For coronal conditions, the estimated perpendicular cascade rate[74] should lead to a much faster dissipation of energy at the small scales than linear proton cyclotron dissipation. In short, the ion cyclotron sweep mechanism does not appear to be a viable mechanism for heating the solar corona.

It is important to distinguish the possibility that a cyclotron-resonant dissipation mechanism likely participates in the spectral cascade together, with other possible kinetic noncyclotron-resonant mechanisms, from the ion cyclotron-sweep mechanism. For example, Bruno and Trenchi[78] showed that the ion spectral break moves to higher and higher frequencies as the Sun is approached. They showed quite clearly that, of the possible correspondences of the ion gyrofrequency and the frequencies corresponding to the ion-inertial length and Larmor radius, the ion-cyclotron resonance frequency is the one that better matches the location of the break point. This suggests that a cyclotron-resonant dissipation mechanism might be one of the processes involved in the spectral cascade. Related ion-cyclotron dissipation mechanisms that may lead to temperature anisotropy have been observed statistically at 1 au by Telloni *et al.*[79] Another set of kinetic fluctuations that may be important for dissipation is kinetic Alfvén waves (KAWs), which are ion scale dispersive waves with primarily perpendicular wave vectors[80] and are formed naturally by a turbulent cascade.[81] KAWs have been considered in the context of, e.g., solar wind heating[82] and solar electron heating in the corona.[83]

In the remainder of the paper, we first discuss Parker Solar Probe observations from a spectral perspective related to the turbulence models described above. Thereafter, we consider energy-containing theories of the transport of MHD turbulence and their incorporation into models of the solar wind, again focusing on Parker Solar Probe observations. We conclude by revisiting the predictions of the NI quasi-2D and W/T models listed above.

II. OBSERVATIONS OF TURBULENCE AND SMALL-SCALE STRUCTURES BY THE PARKER SOLAR PROBE

To interpret 1D time series data measured by spacecraft, Taylor's hypothesis is often used,[84] implying that the observed time variations correspond to spatial variations in the direction of solar wind flow.[85] Consequently, the turbulence properties measured by spacecraft depend on the direction of the solar wind flow with respect to the background magnetic field. In the framework of the 2D + slab turbulence model, 2D fluctuations can only be measured when the flow is perpendicular to the background magnetic field, while the slab fluctuations are measured when the flow is parallel to the background magnetic field. Small-scale magnetic flux ropes are a representation of the quasi-2D component of turbulent fluctuations. This is supported by the observation that the axial field of flux ropes tends to align with the nominal spiral interplanetary magnetic field.[86] The identification and characterization of small-scale magnetic flux ropes are helpful for understanding quasi-2D turbulent dynamics.[17–19] Taylor's hypothesis also implies a potential observational bias as the solar wind flow is more likely to be aligned with the background magnetic field closer to the Sun,[87,88] indicating that the quasi-2D small magnetic flux rope with wave vectors perpendicular to the mean field cannot be observed. However, field-aligned flows are very useful for studying fluctuations with parallel wave vectors. As discussed above, observations of turbulence in field-aligned flows may be a key discriminator between the two turbulence theories for coronal heating and solar wind driving. PSP provides a unique opportunity to study these parallel fluctuations.

A. Small-scale magnetic flux ropes

The identification of magnetic flux ropes is usually based on the observed rotation of the magnetic field.[89,90] We have developed an automatic detection method based on the normalized reduced magnetic helicity,[91] which usually has a high value in regions of magnetic flux ropes.[92–95] To remove possible contamination from Alfvénic structures, we also evaluate the normalized cross helicity and normalized residual energy for the structures with high magnetic helicity. In most cases, the cross helicity of a magnetic flux rope is low, and the residual energy is negative (indicating the dominance of magnetic fluctuation energy), while Alfvénic structures usually have high cross helicity and a small residual energy value.

We applied the detection method to the first four orbits of Parker Solar Probe. A wavelet technique is used to construct the spectrogram of the normalized reduced magnetic helicity, normalized cross helicity, and normalized residual energy. As an example, Fig. 2 shows an overview of the PSP's fourth orbit during the period from 2020 January 19 to 2020 February 4 (adapted with permission[96]). The first four panels show the magnetic field magnitude and its components B_R, B_T, and B_N, proton flow speed components (V_R, V_T, and V_N), proton number density N_p, proton temperature T_p, Alfvén speed V_A, the angle between the flow direction and the magnetic field direction θ_{VB}, and proton plasma beta β_p. The wavelet spectrograms of normalized magnetic helicity σ_m, normalized cross helicity σ_c, and normalized residual energy σ_r are shown in the following three panels. The bottom panel shows the radial distance of the PSP from the Sun. The fourth perihelion occurred on 2020 January 29 at around 0.13 au. The two vertical dashed lines in each panel identify two heliospheric current sheet (HCS) crossings, accompanied by an increase in proton plasma beta and a reversal of the sign of the normalized cross helicity σ_c. Between the two HCS crossings, the cross helicity σ_c is predominantly positive, and the residual energy is nearly zero in general, indicating the dominance of outwardly propagating Alfvén waves during this period. However, from January 28 to February 1, near perihelion, PSP appears to measure slow solar wind with the lowest speed around 200 km/s. The decrease in proton velocity is accompanied by an increase in the proton number density and a decrease in the proton temperature during this period. Thereafter, the cross helicity begins to decline, and the residual energy also becomes negative, indicating that the imbalance between the outward and inward propagating waves is lessened, and the magnetic fluctuation energy begins to increase and exceeds the kinetic fluctuation energy. The second HCS crossing is embedded in a region of elevated proton plasma beta, identified as the heliospheric plasma sheet (HPS) that is considered as the extension of the streamer belt at a large heliocentric distance.

The results of our analysis of small-scale magnetic flux ropes during the PSP's fourth orbit are summarized in Fig. 3 (adapted with permission).[96] Our automatic detection criteria for small magnetic flux ropes requires that the (i) normalized reduced magnetic helicity satisfy $|\sigma_m| \geq 0.7$, (ii) normalized cross helicity satisfy $|\sigma_c| \leq 0.3$, and (iii) normalized residual energy satisfy $\sigma_r \leq -0.5$. The high magnetic

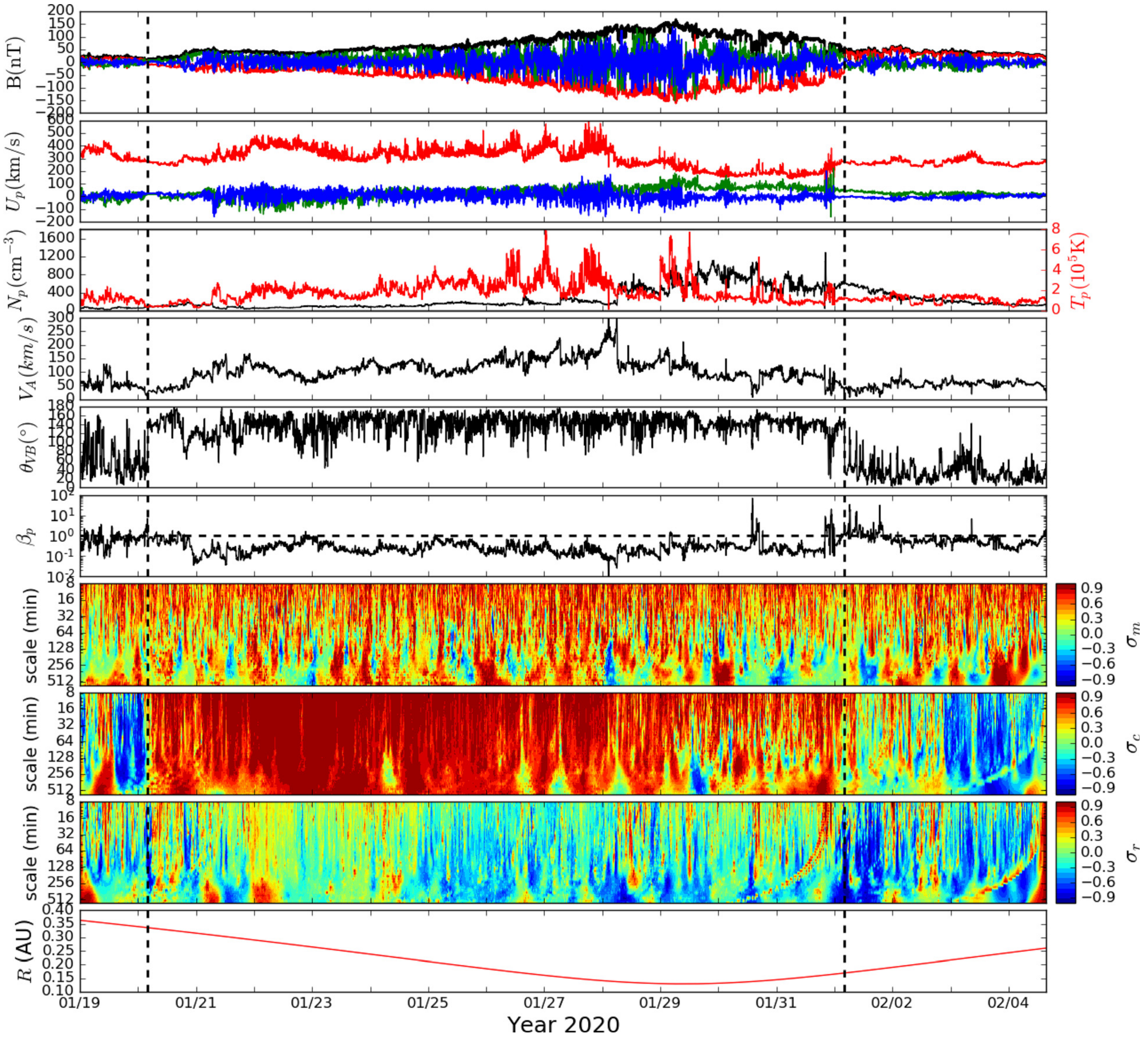

FIG. 2. The PSP *in situ* observations from its fourth orbit traversal from 2020 January 19 to 2020 February 4. The panels from top to bottom show, respectively, the magnetic field magnitude ($|B|$) and three components (B_R, B_T, and B_N), solar wind velocity components (V_R, V_T, and V_N), proton number density (N_p) and proton temperature (T_p), the Alfvén speed V_A, the angle θ_{VB} that shows the alignment between the flow velocity and magnetic field, proton plasma beta (β_p), the spectrograms of the normalized reduced magnetic helicity (σ_m), normalized cross helicity (σ_c), and normalized residual energy (σ_r). The bottom panel shows the radial distance of PSP from the Sun. The vertical dashed line in each panel identifies heliospheric current sheet (HCS) crossings. Reproduced with permission from Zhao *et al.*, Astron. Astrophys. **650**, A12 (2021).[96] Copyright 2021 EDP Sciences.

helicity identifies a rotating magnetic field in the flux rope region, while a low cross helicity and a nonzero residual energy excludes Alfvénic structures. It should be noted that some small magnetic flux ropes may also have Alfvénic fluctuations, whether its origin is the Sun or local magnetic reconnection in the solar wind or local nonlinear dynamics. However, we do not currently have a clear criterion to determine if Alfvén waves are generated within the magnetic flux ropes.[97] Therefore, we exclude all possible Alfvén waves in our search routine. Figure 3 shows the normalized cross helicity σ_c vs the normalized residual energy σ_r for the identified structures with high magnetic helicity σ_m. At a distance close to the Sun (within 0.35 au), the structures with high magnetic helicity appear to be highly Alfvénic, which is reflected by a large number of scatter points with high cross helicity $|\sigma_c| \geq 0.5$. Many scatter points are close to the dashed circle $\sigma_c^2 + \sigma_r^2 = 1$, which is characteristic of pure Alfvén waves. The scatter points inside the magenta rectangular box represent the most likely magnetic flux rope structures, which satisfies our search criteria, i.e., $|\sigma_m| \geq 0.7$ and $|\sigma_c| \leq 0.3$ and $\sigma_r \leq -0.5$.

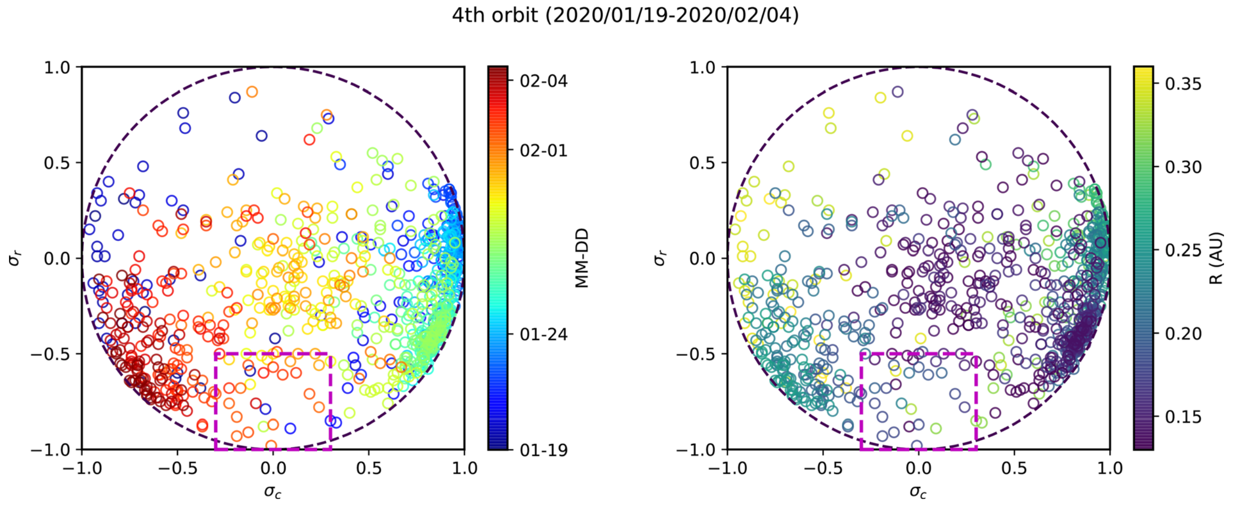

FIG. 3. Normalized cross helicity σ_c vs normalized residual energy σ_r for structures with a high magnetic helicity ($|\sigma_m| \geq 0.7$) identified in the fourth orbit. Left panel: scatter circles are colored according to the date. Right panel: points are colored according to the radial distance to the Sun. The dashed-dotted circle represents $\sigma_c^2 + \sigma_r^2 = 1$. The magenta rectangular box represents the region that likely contains flux rope structures with $|\sigma_c| \leq 0.3$ and $\sigma_r \leq -0.5$. Reproduced with permission from Zhao *et al.*, Astron. Astrophys. **650**, A12 (2021).[96] Copyright 2021 EDP Sciences.

Figure 4 presents a statistical study of the small magnetic flux rope occurrence rate during the PSP's fourth orbit using the magnetic helicity-based detection technique. The bar plots in the top panel show the number of small magnetic flux ropes per calendar day. The counts are color-coded for flux ropes with different durations. The following panels show 10 min moving-averaged radial magnetic field, proton density, and proton plasma beta plots. The location of the two HCS crossings, the fourth perihelion, and the HPS are also shown in the figure. Within the HPS region, the plasma beta shows a clear enhancement compared to the surrounding solar wind.

As shown in the figure, most of the small magnetic flux ropes are of short duration (less than ~40 min) and are observed frequently in the vicinity of the HCS crossing. Between January 21 and January 27, where the solar wind fluctuations are strongly imbalanced ($\sigma_c \simeq 1$ and $\sigma_r \simeq 0$), no magnetic flux ropes are detected. As illustrated in Fig. 2, θ_{VB} is ~180° between January 21 and January 27, and therefore the

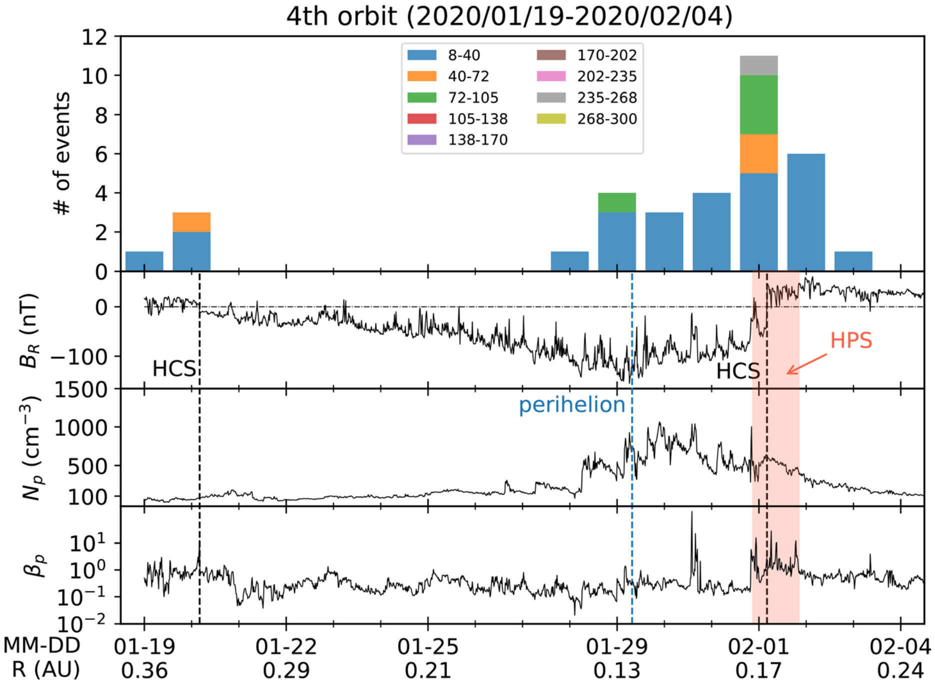

FIG. 4. Counts of magnetic flux ropes per calendar day during the PSP's fourth orbit. The counting bars are color-coded by the duration of flux ropes. The blue bar indicates a duration of 8 to 40 min, the orange bar 40 to 72 min, the green bar 72 to 105 min, and the gray bar 235 to 268 min. The radial magnetic field B_R, proton density N_p, and proton plasma beta β_p are shown in the bottom three panels. The two HCS crossings are identified by black vertical dashed lines, the fourth perihelion (~0.13 au) is indicated by a blue vertical dashed line, and the HPS is indicated by the pink shaded area. Reproduced with permission from Zhao *et al.*, Astron. Astrophys. **650**, A12 (2021).[96] Copyright 2021 EDP Sciences.

flow is highly magnetic field aligned, making the detection of quasi-perpendicular fluctuations such as flux ropes impossible. The identified long-duration flux ropes ($\geq$1 h) are mainly located at the second HCS crossing when the PSP is embedded in the streamer belt region, and the flow speed is rather slow ($\simeq$200 km/s). Some of these long-duration flux ropes may originate from narrow coronal mass ejections (CMEs)/blobs that are observed in coronagraph white-light images, but to be certain of the connection, more detailed analysis is needed.

B. Spectral features in field-aligned solar wind turbulence

As discussed above, a critical discriminant between the turbulence models proposed to explain coronal heating is the anisotropic nature of solar wind turbulence. In the context of solar wind turbulence, for example, Horbury *et al.*[98] and Podesta[99] used a wavelet technique to analyze the spectral anisotropy of magnetic fluctuations. They find that the inertial range of the magnetic power spectrum follows a Kolmogorov-like $\sim k_\perp^{-5/3}$ power law when the wave vector k is perpendicular to the background local magnetic field, and a $k_\parallel^{-2}$ power law spectrum when the wave vector is parallel to the background local magnetic field. The different power law indices in the parallel and perpendicular wave vector were interpreted as being consistent with the critical balance theory proposed by Goldreich and Shridhar[72] for strong Alfvénic turbulence. Note that in these studies, the local scale-dependent background magnetic field derived from the wavelet technique is used to calculate the parallel and perpendicular spectra. In contrast, Tessein *et al.*[100] found no difference in the spectral indices of parallel and perpendicular fluctuations when using a global mean magnetic field. Therefore, despite the theoretical inconsistency with the definition of the mean magnetic field, it has been thought that the critical balance theory can be validated only when the local background magnetic field is used instead of the global mean magnetic field. However, later studies[101] find that these observations, which were thought to be consistent with critical balance theory when using a local scale-dependent background magnetic field, might be influenced by the presence of intermittency. Turbulence intermittency can effectively change the parallel spectrum exponent from an inherent $-5/3$ value to -2. Furthermore, by applying the standard Fourier transform method to each 6 min interval, Wang *et al.*[7] confirmed that the critical balance prediction is valid for moderate-amplitude fluctuations, but invalid for the low-amplitude magnetic fluctuations, which have $k_\parallel^{-5/3}$ power law spectra. Recent work by Telloni *et al.*[8] extended the interval length used by Wang *et al.* to more than 1 h and conducted a rigorous search of parallel fluctuation intervals to avoid the effects of intermittency. In their work, the spectral indices of the uni-directionally propagating Alfvén waves with moderate-amplitude parallel fluctuations were found to be close to $-5/3$ instead of -2. A Kolmogorov-like $k_\parallel^{-5/3}$ spectrum for the strongly imbalanced turbulence can be explained by the NI MHD turbulence theory of Zank *et al.*[18,19]

Following those previous studies at 1 au, we searched for intervals observed by PSP with a highly field-aligned flow. Assuming Taylor's hypothesis and the Parker spiral magnetic field, PSP is more likely to measure parallel spectra close to the Sun. We apply strict search criteria to ensure that the selected intervals are mostly populated by the undisturbed Alfvénic parallel fluctuations. We then apply two spectral analysis methods, a standard Fourier analysis and a novel Hilbert spectral analysis (HSA),[102] to compute the power spectra of the magnetic fluctuations in these intervals.[9] The HSA is based on the Hilbert–Huang transformation (HHT) and has the advantage of allowing for the analysis of nonlinear and nonstationary data without *a priori* bases.

As an example, in Fig. 5, we show the spectral features of two identified field-aligned intervals observed by PSP in its first two orbits. Both intervals correspond to slow wind, unlike the Telloni *et al.*[42] fast wind examples. The first interval starts at 04:15:35 UT on 2018 November 3 and lasts for 23 min. During this period, the radial distance of the PSP is about 0.2 au, the observed average solar wind speed $\langle V_{sw}\rangle$ is 251 km/s, the magnetic field magnitude $\langle B_m\rangle$ is 73 nT, the angle between the local magnetic field and the flow direction $\langle\theta_{VB}\rangle$ is 172°, and the magnetic compressibility is 0.04. Specifically, although the averaged $\theta_{VB} = 172°$, as shown in Fig. 1 by Zhao *et al.*,[9] θ_{VB} during this interval varies from 160° to 180° when using $\sim$0.22 second

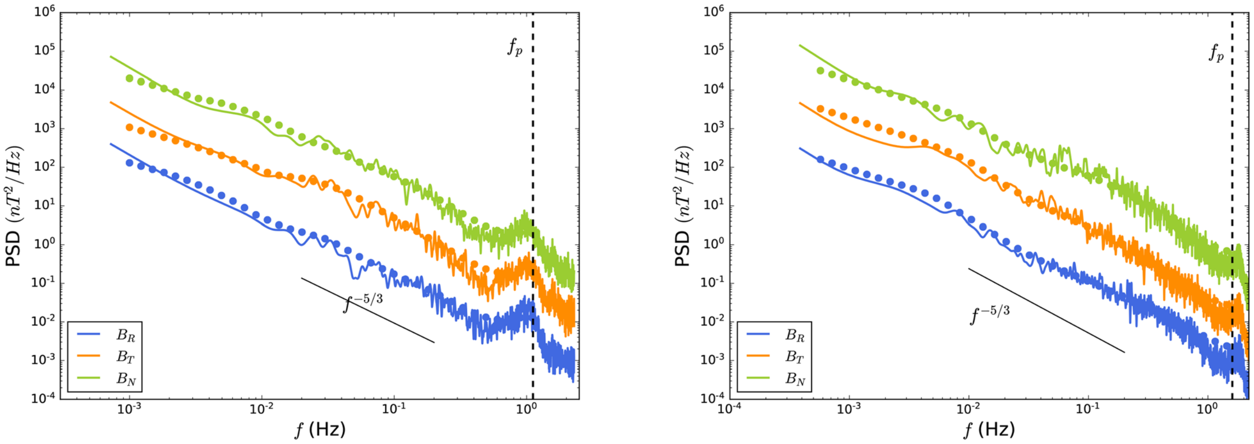

FIG. 5. Left panel: Fourier spectra (solid lines) and Hilbert spectra (dots) of the magnetic field components for the field-aligned interval on 2018 November 3. The spectra have been shifted for presentation purposes. Right panel: as in the left panel except for the field-aligned interval on 2019 April 4. Reproduced with permission from Zhao *et al.*, Astrophys. J. **898**, 113 (2020).[9] Copyright 2020 IOP Publishing.

resolution magnetic field and plasma data. Hence, in this interval the field and velocity are aligned with each other on both global and local scales (from 0.22 s to 23 min scales). Another identified field-aligned interval is from 05:18:35 to 06:01:22 UT on 2019 April 4, at about 0.17 au. During this interval, $\langle V_{sw} \rangle$ is 310 km/s, $\langle B_m \rangle$ is 100 nT, and $\langle \theta_{VB} \rangle$ is 171° ($160^\circ \leq \theta_{VB} \leq 180^\circ$).

The left and right panels of Fig. 5 show the standard Fourier power spectra (curves) and Hilbert marginal spectra (dots) for the three magnetic field components B_R, B_T, and B_N in the two parallel fluctuations dominated intervals. The Fourier and Hilbert spectra of each component are consistent with each other. A Kolmogorov power-law spectrum with an index of $-5/3$ is displayed for reference. The dashed vertical line identifies the proton gyrofrequency f_p. The power-law fitting is applied to the spectrum of each component within the inertial range of 0.01 Hz–0.5 Hz. For the interval on 2018 November 3, the spectral exponent of the B_R component is given by -1.55 ± 0.02, the B_T component -1.60 ± 0.05, and the B_N component -1.64 ± 0.02. For the interval on 2019 April 4, the spectral exponent of the B_R component is given by -1.5 ± 0.03, the B_T component -1.65 ± 0.02, and the B_N component -1.4 ± 0.03. The spectral indices of all three components are close to $-5/3$ rather than the -2 predicted by the "critical balance" theory for parallel fluctuations.

For completeness, we also evaluate the spectra of the normalized cross helicity σ_c and normalized residual energy σ_r. The left panel of Fig. 6 shows the Fourier power spectra of σ_c and σ_r for the interval on 2018 November 3. The right panel shows the velocity fluctuation trace power spectrum (black curve) and the velocity magnitude fluctuation spectrum (red curve). The blue vertical dashed line denotes the solar probe cup (SPC) noise floor, at which the velocity spectrum flattens and the effects of noise become important. Within the inertial range down to the SPC noise floor, the velocity fluctuation spectrum follows a $f^{-3/2}$ power law. The normalized cross helicity and residual energy remain approximately constant with $\sigma_c \simeq 0.8$ and $\sigma_r \simeq 0$ in the inertial range, which suggests that the identified field-aligned flow is highly imbalanced and dominated by uni-directional Alfvénic fluctuations. Therefore, we conclude that the parallel magnetic fluctuation spectrum has the form of a $-5/3$ power law spectrum in highly imbalanced turbulence.

The observed $k_\parallel^{-5/3}$ magnetic power spectrum in highly imbalanced turbulence can be explained by the nearly incompressible (NI) MHD theory developed by Zank *et al.*[19] Based on the NI theory, the turbulent fluctuations can be decomposed as majority 2D and minority slab components, corresponding to perpendicular and parallel wave vectors, respectively. In that theory, the 2D component possesses the classical $k_\perp^{-5/3}$ spectrum in the perpendicular wavenumber

$$G^\infty(k_\perp) \equiv E^\infty(k_\perp)k_\perp = C_k \varepsilon_\infty^{2/3} k_\perp^{-5/3}, \tag{1}$$

where C_k is the Kolmogorov constant and ε_∞ is the dissipation rate of 2D incompressible MHD turbulence. We introduce an Alfvén timescale[19] $\tau_A^{-1} = \frac{V_{A0}}{\lambda_A}(1 - \sigma_c^{*2})^{1/2}(M_{A0}^t)^2$, where V_{A0} is the mean Alfvén speed, λ_A is the Alfvén correlation length, and M_{A0}^t denotes the turbulent Alfvén Mach number. See Zank *et al.*[19] for further discussion. The spectrum of the minority NI component is governed by the ratio of the nonlinear and Alfvén timescales,

$$G^*(k_\parallel) \equiv E^*(k_\parallel, k_\perp)k_\perp^2$$
$$= C_k^{1/4} \varepsilon_*^{1/2} \varepsilon_\infty^{1/6} k_\perp^{-2/3} k_\parallel^{-1} \left(1 + \left(\frac{s^3 V_{A0}^3 (M_{A0}^t)^6}{C_k^{3/2} \varepsilon_\infty}\right)^{1/3} k_\parallel k_\perp^{-2/3}\right)^{1/2}, \tag{2}$$

where $s = (1 - \sigma_c^{*2})^{1/2}$ and ε_* is the NI/slab dissipation rate. We consider a possible relationship between parallel and perpendicular wavenumbers $k_\perp k_t^{a-1} = k_\parallel^a$, with k_t a transitional wavenumber defined by $k_t^{-1} = (s^3 V_{A0}^3 (M_{A0}^t)^6)/(C_k^{3/2} \varepsilon_\infty)$. Uni-directional wave propagation implies $s = 0$ and $k_t^{-1} = 0$. For strongly imbalanced turbulence ($a = 1$), we find[19]

$$G^*(k_\parallel) = \varepsilon_*^{1/2} \varepsilon_\infty^{1/6} k_\parallel^{-5/3}, \tag{3}$$

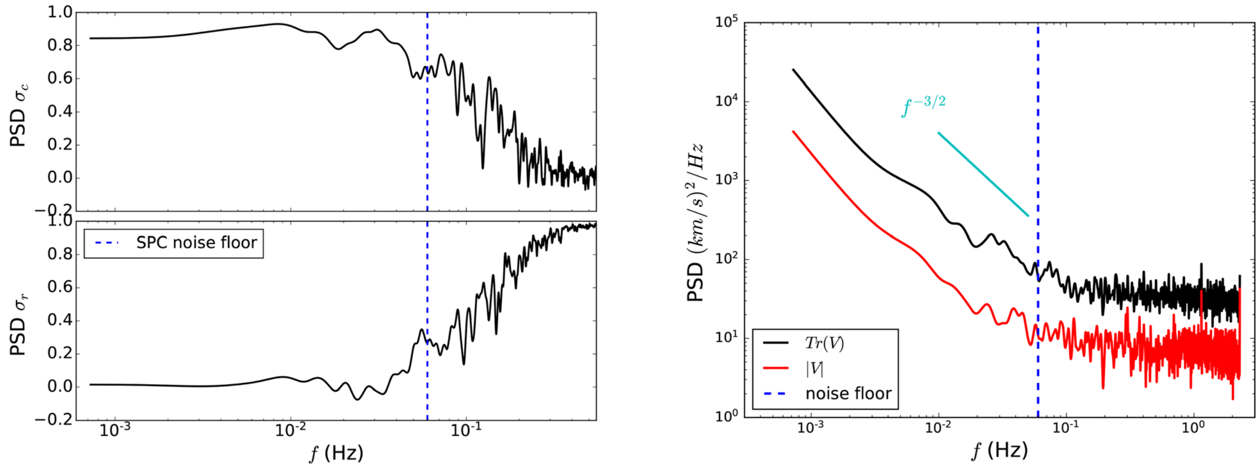

FIG. 6. Left panel: Fourier power spectra of the normalized cross helicity σ_c and normalized residual energy σ_r for the identified field-aligned interval. Right panel: the trace power spectrum (black curve) of velocity fluctuations and the spectrum of the velocity magnitude fluctuations (red curve). The spectra are analyzed for the ~5 Hz cadence plasma velocity data in a ~23 min interval. The blue vertical dashed line identifies the frequency at which the velocity spectrum begins to flatten and where noise may become important. Reproduced with permission from Zhao *et al.*, Astrophys. J. **898**, 113 (2020).[9] Copyright 2020 IOP Publishing.

which corresponds to a power spectral index of $-5/3$ for parallel magnetic fluctuations, as observed in the PSP data for field aligned flows.

III. PSP OBSERVATIONS AND TURBULENCE TRANSPORT MODELING

Properly understanding the heating of the solar corona and the subsequent development of the supersonic solar wind requires understanding the transport, evolution, and distributed dissipation of turbulence from the base of the corona to the distant heliosphere. Two approaches to the transport of turbulence have been developed. The first is based on an incompressible MHD phenomenology[70,103–108] and the second on a NI MHD phenomenology.[18,109–111] The two turbulence transport models are distinguished by (i) the first group of turbulence transport models describing isotropic turbulence and being appropriate to a high plasma beta β_p regime, whereas the second set of models describes highly anisotropic turbulence that comprises a superposition of a majority quasi-2D component and a minority NI/slab component and is appropriate to $\beta_p \sim 1$ or $\ll 1$, (ii) the NI MHD turbulence models admitting uni-directionally propagating Alfvén waves that interact with the majority quasi-2D turbulence component in a passive scalar sense, and (iii) the first admitting a singularity at the Alfvén surface that can lead to a "turning off" of turbulence there, unlike the NI MHD models.[67] In this section, we compare theoretical NI MHD turbulence transport model results with PSP (and Helios 2) observations.

The inhomogeneous NI MHD formulation[111] describes the transport of the majority quasi-2D and a minority NI/slab turbulence throughout the solar wind. Zank *et al.*[18] expressed the NI MHD system in terms of majority quasi-2D and minority NI/slab Elsässer variables. They derived 12 coupled transport equations describing moments of the majority quasi-2D and minority NI/slab primitive equations. Through a suitable combination, this yields equations describing the transport of energy in forward and backward propagating modes, the residual energy, and the corresponding correlation functions. The Zank *et al.* model was applied to supersonic solar wind turbulence, and a preliminary comparison between the theory and Voyager 2 and Ulysses measurements[18] showed that the NI MHD turbulence model can describe the evolution of turbulence throughout the heliosphere. More detailed analyses by Adhikari *et al.*[112] and Zank *et al.*[113] investigated solar wind heating and pickup ion transport throughout the heliosphere, finding that the NI MHD two-component turbulence model captures the behavior of the energy in forward and backward propagating modes, total turbulent energy, the variance in the magnetic field fluctuations and the fluctuations in the solar wind speed, the variance in the density fluctuations, the normalized cross-helicity and residual energy, the solar wind proton temperature, and the various correlation lengths observed by Voyager 2 throughout the heliosphere. Related studies have used NI MHD turbulence models to investigate the transport of cosmic rays in the solar wind.[114,115] The comparison of the NI MHD transport models to a variety of observations provides some confidence in the effectiveness of the NI MHD model as a description of turbulence throughout the heliosphere.

The basic approach to the NI MHD turbulence model for heating the solar corona was presented by Zank *et al.*[17] In developing a quantitative model to study the transport and evolution of turbulence in the quiet solar corona from the coronal base to 15 $R_\odot$, Zank *et al.*[17] applied the coupled quasi-2D and NI/slab turbulence transport equations to prescribed background profiles for the coronal flow speed and density. It was assumed that the photospheric magnetic carpet pumps quasi-2D structures continuously into the solar corona above the photosphere. Estimates[17] based on observations indicate that sufficient magnetic energy is introduced via the magnetic carpet to account for the required dissipation to explain the heating of the coronal plasma. The mechanism advanced by Zank *et al.* is related to the idea advanced by Parker[16,116,117] that the random twisting and braiding of magnetic field lines allow for the dissipation of magnetic energy via nanoflares above the photosphere. The simplified approach presented by Zank *et al.*[17] demonstrated that the turbulent dissipation of quasi-2D turbulence is sufficient to heat the solar corona to temperatures $\sim 2 \times 10^6$ K within 2 $R_\odot$ (see also the comments in Sec. I about an alternative method for generating 2D turbulence in the chromosphere below the transition region from a large flux of upwardly propagating Alfvénic fluctuations). An important advance by Adhikari *et al.*[40] extended the Zank *et al.* model by coupling the evolution, transport, and dissipation of turbulence to the basic solar wind equations to model a fast solar wind flow originating from an open coronal hole in which the flow is highly aligned with the magnetic field. Adhikari *et al.* found that the heating near the coronal base is due primarily to the dissipation of quasi-2D turbulence rather than NI/slab turbulence, resulting in the heating of the coronal plasma to temperatures of $\sim 10^6$ K within a few solar radii. Hence, the dominant quasi-2D component appears to be mainly responsible for the acceleration of the solar wind. Adhikari *et al.*[118] applied a related model to investigate the transport, evolution, and dissipation of turbulence in the slow solar wind along the trajectory of the Parker Solar Probe, finding good correspondence between the theory and observations. Adhikari *et al.*[119] further extended their model to include electrons as a separate fluid component. The additional physics introduced by electrons, i.e., the incorporation of an *ad hoc* separate turbulent heating of protons and electrons, Coulomb collisions between protons and electrons, and a phenomenological electron heat conduction, augmented by additional turbulence physics such as the Alfvén effect and the turbulent dynamo effect,[70,120,121] yields good agreement between theoretical solutions and the fast solar wind flow measured by PSP and Helios 2.

Before comparing the theoretical turbulence-mediated solar wind solutions to the fast and slow solar wind flows measured by PSP and Helios 2, we discuss briefly PSP solar wind electrons alphas and protons (SWEAP) observations during its first encounter in the outbound direction. The plasma data correspond to the moment data derived from PSP SWEAP measurements.[3] Figure 7 shows the solar wind speed (top panel), solar wind proton density (second panel), solar wind proton temperature (third panel), proton mass flux (fourth panel), and thermal plasma beta (bottom panel) as a function of heliocentric distance. In the figure, the light blue symbols correspond to solar wind with a speed of less than 420 km/s, and dark blue symbols to flows with speed greater than 420 km/s. Evidently, PSP observed a fast (∼600 km/s) and a slow (∼400 km/s) solar wind stream during its first encounter in the outbound direction. The other solar wind parameters also reflect this classification.

A. Toward an NI MHD turbulence-driven model of the solar wind

The NI MHD phenomenology[18,70,109–112,122,123] distinguishes between a strong and weak guide magnetic field through the value of

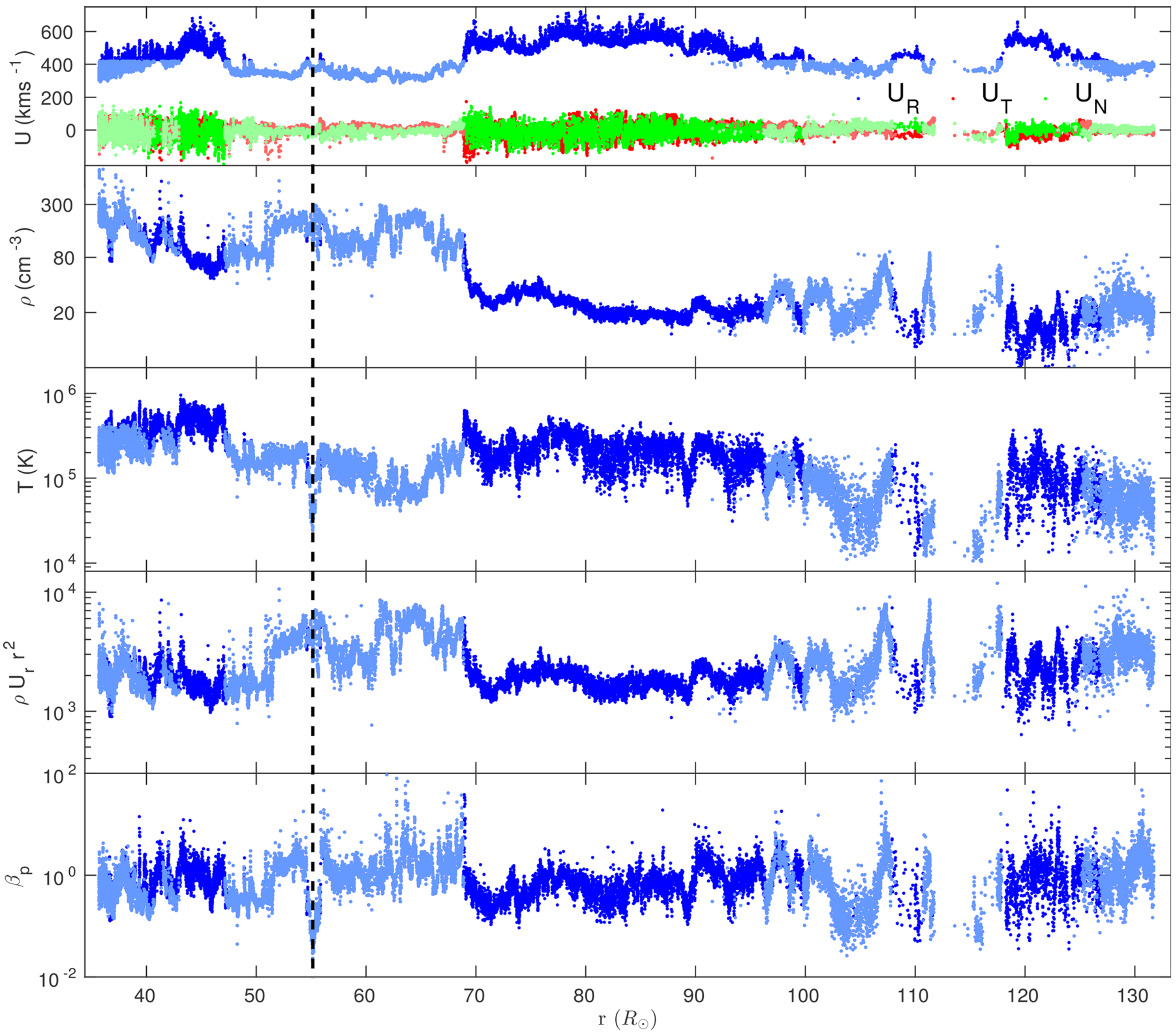

FIG. 7. PSP SWEAP measurements: solar wind speed (top panel), solar wind density (second panel), solar wind proton temperature (third panel), mass flux (fourth panel), and the plasma beta (bottom panel) as a function of heliocentric distance. Light blue "." symbols correspond to solar wind speeds less than 420 km/s, and dark blue "." symbols correspond to flow speeds greater than 420 km/s. The vertical line identifies the location of a coronal mass ejection observed by PSP at ~55.2 R$_\odot$. Reproduced with permission from Adhikari *et al.*, Astrophys. J. Suppl. Ser. **246**, 38 (2020).[118] Copyright 2020 IOP Publishing.

the plasma beta β_p. Specifically, the $\beta_p \gg 1$ regime corresponds to an isotropic leading-order incompressible MHD model, whereas the $\beta_p \sim 1$ and $\ll 1$ regimes yield an MHD description that comprises a majority quasi-2D and a minority NI/slab component. The solar wind and certainly the solar corona are typically found in the $\beta_p \sim 1$ or $\ll 1$ regimes. In this case, the total Elsässer variables can be written as the sum of the quasi-2D and NI/slab Elsässer variables, i.e., $\mathbf{z}^{\pm} = \mathbf{z}^{\infty\pm} + \mathbf{z}^{*\pm}$ (where, $\mathbf{z}^{\infty\pm} \gg \mathbf{z}^{*\pm}$), provided certain symmetries of the underlying turbulence hold.[18] Zank *et al.*[18] provide a detailed derivation of the NI MHD turbulence transport model equations. The majority quasi-2D and minority NI/slab Elsässer variables can be written as[18]

$$\mathbf{z}^{\infty\pm} = \mathbf{u}^{\infty} \pm \frac{\mathbf{B}^{\infty}}{\sqrt{\mu_0 \rho}} \quad \text{and} \quad \mathbf{z}^{*\pm} = \mathbf{u}^{*} \pm \frac{\mathbf{B}^{*}}{\sqrt{\mu_0 \rho}}, \tag{4}$$

where the superscripts "∞" and "$*$" indicate quasi-2D turbulence and NI/slab turbulence, respectively. The quasi-2D and NI/slab variances of the Elsässer variables and the residual energy E_D can be written as[18,70]

$$\langle z^{\infty,*\pm 2} \rangle = \langle \mathbf{z}^{\infty,*\pm} \cdot \mathbf{z}^{\infty,*\pm} \rangle; \quad E_D^{\infty,*} = \langle \mathbf{z}^{\infty,*+} \cdot \mathbf{z}^{\infty,*-} \rangle, \tag{5}$$

where $\langle z^{+2} \rangle$ and $\langle z^{-2} \rangle$ are the energy in forward and backward propagating modes, respectively. The correlation functions corresponding to the forward/backward propagating modes and the residual energy can be written as

$$L^{\pm}_{\infty,*} = \int \langle \boldsymbol{z}^{\infty,*\pm}\cdot \boldsymbol{z}^{\infty,*\pm\prime}\rangle dy \equiv z^{\infty,*\pm 2}\lambda^{\pm}_{\infty,*}, \tag{6}$$

$$L_D^{\infty,*} = \int \langle \mathbf{z}^{\infty,*+}\cdot\mathbf{z}^{\infty,*-\prime} + \mathbf{z}^{\infty,*+\prime}\cdot\mathbf{z}^{\infty,*-}\rangle dy \equiv E_D^{\infty,*}\lambda_D^{\infty,*}, \tag{7}$$

where $y = |\mathbf{y}|$ is the spatial lag between fluctuations, $\mathbf{z}^{\infty,*-\prime}$ are lagged Elsässer variables, and $\lambda^{\pm}$ and λ_D are the correlation lengths corresponding to the forward/backward propagating modes and the residual energy.

1. Observational support for a majority 2D: Minority slab decomposition

Here, we discuss briefly the existing observational support for a decomposition of solar wind turbulence into dominant quasi-2D and minority slab components in an NI MHD framework.

Slow wind density fluctuations ($\delta\rho$) are shown as a function of turbulent sonic Mach number $M_s = \delta u/C_s$ in the left panel of Fig. 8. Here, $C_s = \sqrt{\gamma P/\rho}$ is the sound speed, $\gamma(=5/3)$ is the polytropic index, P is the thermal pressure, and ρ is the solar wind mass density. A least squares fit of the density fluctuations and the turbulent Mach number yields the relationship $\delta\rho \sim M_s^{0.97}$, which is close to the $\delta\rho \sim O(M_s)$ scaling predicted by Hunana *et al.*[111,124] and Bhattacharjee *et al.*[125] for nearly incompressible inhomogeneous flows. Figure 8 shows histograms of $\delta\rho/\rho$ (middle panel) and M_s (right), illustrating that $\delta\rho/\rho$ clusters around $\sim$0.15, and M_s around $\sim$0.3 and $\sim$0.6. The small values of the density fluctuations, the $\sim O(M_s)$ scaling of $\delta\rho$, and the small sonic turbulent Mach number support an interpretation of the PSP-observed solar wind flow as nearly incompressible.

Early and important work by Bieber and colleagues[126,127] suggested that 2D turbulence dominated slab turbulence in the vicinity of the Earth, typically in a ratio of approximately 80:20, consistent with theoretical expectations.[18,19,109,110] Motivated by this work, subsequent studies have attempted to further identify the underlying anisotropy of low-frequency MHD turbulence.[7–9,98,99,128–130] A recent analysis by Pine *et al.*[131] computed the power in the perpendicular and parallel components of the fluctuating magnetic energy using Advanced Composition Explorer (ACE) and Voyager magnetometer data, finding that the power in the perpendicular component exceeded that in the parallel component. Adhikari *et al.*[132] analyzed Solar Orbiter magnetometer[133] and Solar Wind Analyzer–Proton and Alpha Sensor (SWA–PAS) plasma data[134] obtained between July 7, 2020 and August 31, 2020. During this time, Solar Orbiter was at a heliocentric distance of 140–193 $R_\odot$ and within a latitude of 5°. The slow solar wind speed ranged from 300–420 km/s, and the fast solar wind speed exceeded 420 km/s.

Adhikari *et al.*[132] derived the energy in forward and backward propagating modes, the normalized residual energy, the normalized cross-helicity, the fluctuating kinetic and magnetic energy, the relevant correlation lengths, and the variance of the density fluctuations by using the R, T, and N components of the solar wind speed and the magnetic field, and the solar wind density. They evaluate the perpendicular (or 2D) and slab variances of the Elsässer variables, the fluctuating magnetic energy, and the fluctuating kinetic energy with respect to the direction of the mean magnetic field following Belcher and Davis,[135] i.e.,

$$\sigma^2_{slab} = \frac{\sum \langle B_i\rangle S_{ij}\langle B_j\rangle}{|\langle \mathbf{B}\rangle|}; \quad \sigma^2_{\perp} = \sigma^2_s - \sigma^2_{slab}, \quad i,j = R,T,N, \tag{8}$$

where $\sigma^2_\perp$ and σ^2_{slab}, denote the variances of various turbulence quantities perpendicular and parallel to the mean magnetic field $\langle\mathbf{B}\rangle$, approximately corresponding to 2D and slab turbulence, respectively. The ensemble average $\langle\ldots\rangle$ refers to averaging over a specified time interval. Finally, σ^2_s corresponds to the trace of $\mathbf{S}$, where

$$S_{ij} = \langle A_iA_j\rangle - \langle A_i\rangle\langle A_j\rangle \tag{9}$$

is a 3×3 matrix, formed by the R, T, and N components of a vector $\mathbf{A}$.

Use of Eqs. (8) and (9) allowed Adhikari *et al.*[132] to obtain the observed total energy, 2D energy, and slab energy corresponding to forward [Figs. 9(A1) and 9(B1)] and backward propagating modes [Figs. 9(A2) and 9(B2)], magnetic field fluctuations [Figs. 9(A3) and 9(B3)], and kinetic energy fluctuations [Figs. 9(A4) and 9(B4)] as a function of angle between the mean solar wind speed and the mean magnetic field (θ_{UB}). The top two rows of panels correspond to the slow solar wind and the bottom two panels to the fast solar wind. In the panels of the first and third rows, the green scatter plots with error bars denote the total energy, the red scatter plots with error bars denote the perpendicular energy, the blue scatter plots with error bars denote the energy in slab fluctuations, and the black scatter plots with error bars show the perpendicular + slab energy corresponding to the energy in forward propagating modes, the energy in backward

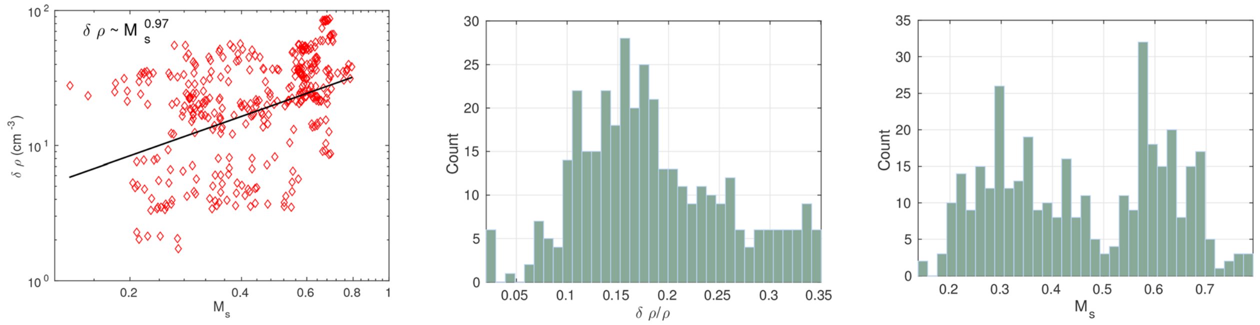

FIG. 8. Left panel: density fluctuations $\delta\rho$ as a function of turbulent Mach number M_s for solar wind with a speed less than 420 km/s. The black line is a least squares fit, showing that $\delta\rho \sim M_s^{0.97}$. Middle panel: histogram of the density fluctuations normalized to the mean density. Right panel: histogram of the turbulent sonic Mach number. Reproduced with permission from Adhikari *et al.*, Astrophys. J. Suppl. Ser. **246**, 38 (2020).[118] Copyright 2020 IOP Publishing.

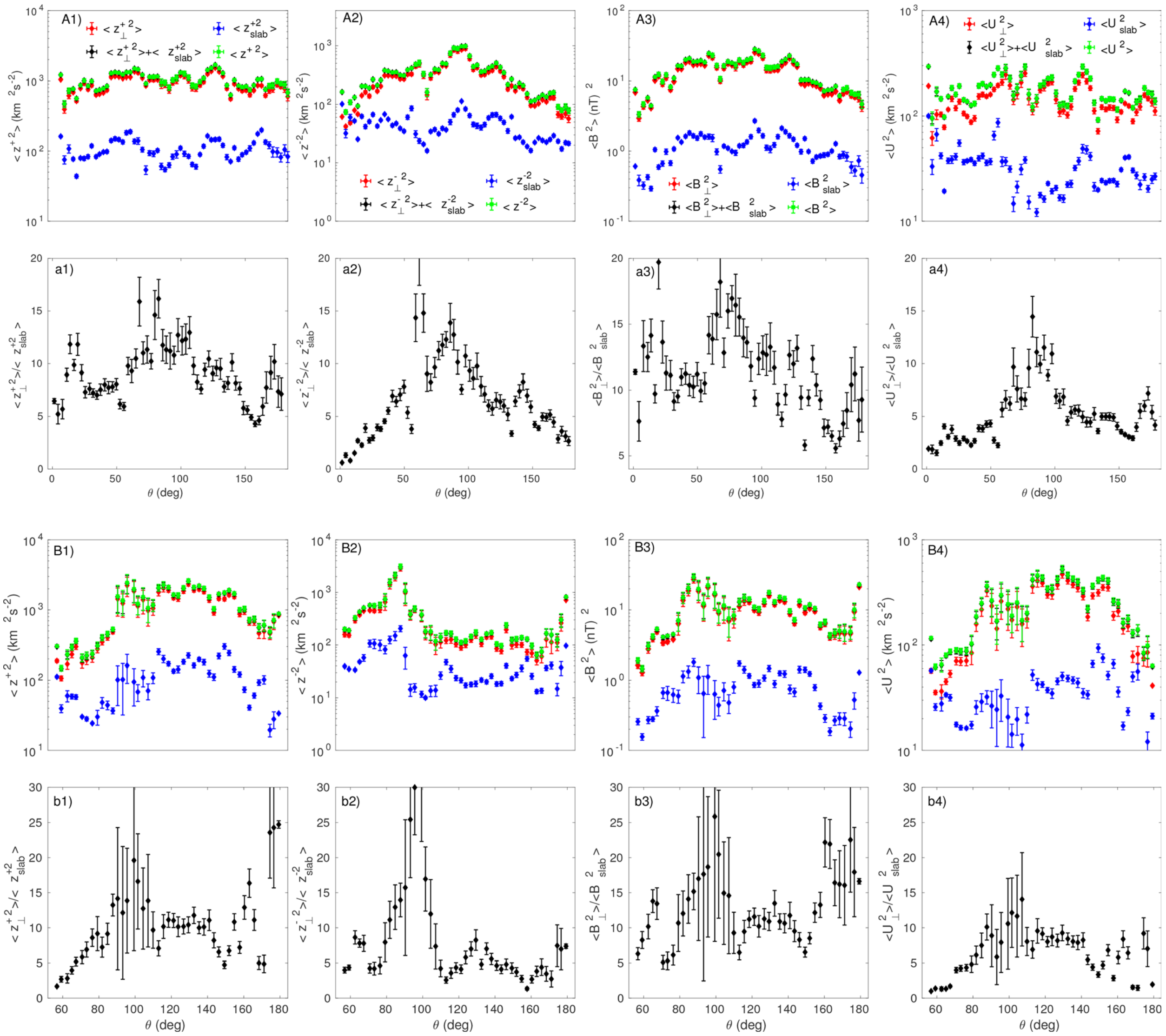

FIG. 9. The first two rows show results for the slow solar wind, and the bottom two rows results for the fast wind. The top and third panel show the total (green), perpendicular (red), slab (blue), and sum of the perpendicular and slab, i.e., perpendicular + slab (black) turbulence energy for forward propagating modes (A1) and (B1), backward propagating modes (A2) and (B2), the fluctuating magnetic energy (A3) and (B3), and the fluctuating kinetic energy (A4) and (B4) for the slow and fast solar wind as a function of angle between the mean solar wind speed and the mean magnetic field (θ_{UB}). The second and fourth panels show the ratio between the 2D and slab variances of energy in forward propagating modes (a1) and (b1), backward propagating modes (a2) and (b2), the fluctuating magnetic energy (a3) and (b3), and the fluctuating kinetic energy (a4) and (b4) as a function of θ_{UB}. Reproduced with permission from Adhikari *et al.*, Astron. Astrophys. (published online, 2021).[132] Copyright 2021 EDP Sciences.

propagating modes, the fluctuating magnetic energy, and the fluctuating kinetic energy. In the plots, the black and green scatter plots overlap and are indistinguishable.

From Fig. 9, the perpendicular + slab (black scatter plots) energy in forward/backward propagating modes is the same as the total energy in forward/backward propagating modes (green scatter plots) (the green and black scatter plots overlap), as does the fluctuating magnetic energy and the fluctuating kinetic energy. The red points in the first and third row of panels correspond to the (quasi-) 2D component of the forward/backward Elsässer, magnetic, and kinetic energies as a function of θ_{UB}. In both the slow and fast solar wind, the red points track the total energy (black or green points) very closely. By contrast, the blue points that describes the corresponding slab contributions are of smaller intensity and lie well below the green and black points. This important result indicates that solar wind turbulence is a superposition of 2D and slab turbulence and that the perpendicular energy in forward and backward propagating modes, the fluctuating magnetic energy, and the fluctuating kinetic energy exceeds the corresponding slab energies, i.e., (quasi-) 2D turbulence dominates. More details can be found in Adhikari *et al.*[132]

The second and fourth rows of panels in Fig. 9 show the ratio between the perpendicular variances and the slab variances of the energy in forward propagating modes [Figs. 9(a1) and 9(b1)], the energy in backward propagating modes [Figs. 9(a2) and 9(b2)], the fluctuating magnetic energy [Figs. 9(a3) and 9(b3)], and the fluctuating kinetic energy [Figs. 9(a4) and 9(b4)] as a function of θ_{UB} for the slow solar wind and the fast solar wind. In the slow solar wind, the ratio between the 2D energy and slab energy clearly depends on θ_{UB} with the ratio being typically larger when the solar wind flow and mean magnetic field are highly oblique and smaller with more aligned magnetic field and solar wind flow. This is consistent with a spacecraft's ability to observe 2D and slab fluctuations primarily in these respective flow-magnetic field geometries.

In the fast solar wind, the results for the ratio of 2D:slab components are similar to those in the slow solar wind, but are not symmetrical about $\theta_{UB} = 90^\circ$ as in the slow solar wind.

The observational results presented by Adhikari *et al.*[132] are consistent with the NI MHD theory[18,109,110] prediction that solar wind turbulence is a superposition of a majority 2D and a minority slab component. Furthermore, Sec. II discussing the observation of quasi-2D structures, i.e., magnetic flux ropes, by PSP further supports the NI MHD approach.[95,96,136] Pressure-balanced structures (PBSs) or flux tubes,[137–139] indicated by sharp changes in solar wind variables in Fig. 7, are common in the solar wind. PBSs/flux tubes are equilibrium solutions of NI MHD[109] but, unlike the static model of flux tubes discussed in Borovsky,[139] PBSs/flux tubes are highly dynamical in the presence of quasi-2D turbulence.[140] The turbulence transport theory presented below includes the dynamics of these structures through the energy density moments of the NI MHD description, interacting dynamically on a nonlinear timescale.

2. Turbulence transport modeling in a spherically expanding solar wind

In the solar corona and inner heliosphere, we can assume that the magnetic field **B** is radial

$$\mathbf{B} = B_0\left(\frac{r_0}{r}\right)^2\hat{r},$$

where B_0 is the magnetic field at a reference location r_0 and $\hat{r}$ denotes the radial direction.

The 1D steady-state majority quasi-2D turbulence transport model equations that describe the transport of quasi-2D turbulence, under the assumption of spherical expansion, are given by[18]

$$U\frac{d\langle z^{\infty\pm 2}\rangle}{dr} + \frac{1}{2}\left(\langle z^{\infty\pm 2}\rangle + E_D^\infty\right)\left(\frac{dU}{dr} + \frac{2U}{r}\right) = -2\alpha\frac{\langle z^{\infty\pm 2}\rangle^2\langle z^{\infty\mp 2}\rangle^{\frac{1}{2}}}{L_\infty^\pm}, \tag{10}$$

$$\begin{aligned} U\frac{dE_D^\infty}{dr} + \frac{1}{2}(E_D^\infty + E_T^\infty)\left(\frac{dU}{dr} + \frac{2U}{r}\right) &= -\alpha E_D^\infty\left(\frac{\langle z^{\infty+2}\rangle^{1/2}}{\lambda_\infty^-} + \frac{\langle z^{\infty-2}\rangle^{1/2}}{\lambda_\infty^+}\right) \\ &\quad +\alpha\left(\frac{\langle z^{\infty+2}\rangle\langle z^{\infty-2}\rangle^{1/2}}{\lambda_\infty^+} + \frac{\langle z^{\infty-2}\rangle\langle z^{\infty+2}\rangle^{1/2}}{\lambda_\infty^-}\right), \end{aligned} \tag{11}$$

$$U\frac{dL_\infty^\pm}{dr} + \frac{1}{2}\left(L_\infty^\pm + \frac{L_D^\infty}{2}\right)\left(\frac{dU}{dr} + \frac{2U}{r}\right) = 0, \tag{12}$$

$$U\frac{dL_D^\infty}{dr} + \frac{1}{2}\left(\frac{dU}{dr} + \frac{2U}{2}\right)\left(L_D^\infty + L_\infty^+ + L_\infty^-\right) = 0, \tag{13}$$

where $E_T^\infty = (\langle z^{\infty+2}\rangle + \langle z^{\infty-2}\rangle)/2$ is the quasi-2D total turbulent energy, U is the solar wind speed, and α is the von-Kármán Taylor constant. In Eq. (10), the right-hand term is the nonlinear dissipation term for the energy in forward and backward propagating modes derived from a Kolmogorov phenomenology. The nonlinear term is responsible for the cascade of energy from large to small scales through the inertial range, which eventually heats the solar wind through dissipation. In Eq. (11), the dissipation term for the residual energy is derived in two ways: the first term follows from a Kolmogorov phenomenology,[18] and the second term results from including the turbulent dynamo effect.[70,120,121] We do not include the Alfvén effect in the quasi-2D turbulence equations because the Alfvén velocity is absent for quasi-2D turbulence. However, we do include it when modeling the dissipation term for the NI/slab residual energy. Simulations[120,121] suggest that the turbulent dynamo effect and the Alfvén effect may be important in controlling the evolution of the residual energy. It is evident that the turbulent dynamo quasi-2D increases the residual energy, whereas of course Kolmogorov dissipation decreases the residual energy.

The corresponding 1D spherically symmetric NI/slab turbulence transport equations are given by[18]

$$\begin{aligned} &(U\mp V_A)\frac{d\langle z^{*\pm 2}\rangle}{dr} + \frac{1}{2}\frac{dU}{dr}\left(\langle z^{*\pm 2}\rangle - E_D^*\right) - (2b-1)\frac{U}{r}\langle z^{*\pm 2}\rangle \\ &\quad + (6b-1)\frac{U}{r}E_D^* \pm 4b\frac{V_A}{r}E_D^* \mp \frac{1}{2}\frac{V_A}{\rho}\frac{d\rho}{dr}\left(z^{*\pm 2} - E_D^*\right) \\ &\quad = -2\alpha\frac{\langle z^{*\pm 2}\rangle\langle z^{\infty\pm 2}\rangle\langle z^{\infty\mp 2}\rangle^{\frac{1}{2}}}{L_\infty^\pm} - 2\alpha\frac{\langle z^{*\pm 2}\rangle^2\langle z^{*\mp 2}\rangle^{\frac{1}{2}}}{L_*^\pm}, \end{aligned} \tag{14}$$

$$\begin{aligned} &U\frac{dE_D^*}{dr} + \frac{1}{2}\frac{dU}{dr}\left(E_D^* - E_T^*\right) - (2b-1)\frac{U}{r}E_D^* + (6b-1)\frac{U}{r}E_T^* \\ &\quad - 4b\frac{V_A}{r}E_C^* - \frac{1}{2}\frac{V_A}{\rho}\frac{d\rho}{dr}E_C^* \\ &\quad = -\alpha E_D^*\left(\frac{\langle z^{\infty-2}\rangle^{1/2}}{\lambda_\infty^+} + \frac{\langle z^{\infty+2}\rangle^{1/2}}{\lambda_\infty^-}\right) \\ &\quad + \alpha\left(\frac{\langle z^{*+2}\rangle\langle z^{\infty-2}\rangle^{1/2}}{\lambda_\infty^+} + \frac{\langle z^{*-2}\rangle\langle z^{\infty+2}\rangle^{1/2}}{\lambda_\infty^-}\right) \\ &\quad - \alpha E_D^*\frac{V_A}{\lambda_*^+ + \lambda_*^-}\left(1 - \sigma_c^*\right)^{\frac{1}{2}}M_{A0}^t 2 \\ &\quad + \alpha\left(\frac{\langle z^{*+2}\rangle\langle z^{*-2}\rangle^{\frac{1}{2}}}{\lambda_*^+} + \frac{\langle z^{*-2}\rangle\langle z^{*+2}\rangle^{\frac{1}{2}}}{\lambda_*^-}\right), \end{aligned} \tag{15}$$

$$\begin{aligned} &(U\mp V_A)\frac{dL_*^\pm}{dr} + \frac{1}{2}\left(L_*^\pm - \frac{L_D^*}{2}\right)\frac{dU}{dr} - (2b-1)\frac{U}{r}L_*^\pm \\ &\quad + \left(3b - \frac{1}{2}\right)\frac{U}{r}L_D^* \pm 2b\frac{V_A}{r}L_D^* \mp \frac{1}{2}\frac{V_A}{\rho}\frac{d\rho}{dr}\left(L_*^\pm - \frac{L_D^*}{2}\right) = 0, \end{aligned} \tag{16}$$

$$\begin{aligned} &U\frac{dL_D^*}{dr}+\frac{1}{2}\left(L_D^*-L_*^+-L_*^-\right)\frac{dU}{dr}\\ &\quad-\frac{2U}{r}\left[\left(b-\frac{1}{2}\right)L_D^*-\left(3b-\frac{1}{2}\right)\left(L_*^-+L_*^+\right)\right]\\ &\quad-4b\frac{V_A}{r}\left(L_*^+-L_*^-\right)-\frac{1}{2}\frac{V_A}{\rho}\frac{d\rho}{dr}\left(L_*^+-L_*^-\right)=0, \end{aligned} \tag{17}$$

where V_A is the Alfvén velocity, and E_C^* is the NI/slab cross helicity. The parameter b, which is associated with a closure assumption for the off diagonal two-point correlations,[70] reflects the geometry of NI/slab turbulence. The von-Kármán Taylor constant α is associated with the nonlinear heating rate. The nonlinear dissipation terms for the energy in forward and backward propagating modes are based on a Kolmogorov phenomenology.[18,19,70] The modeling of the nonlinear dissipation term for the residual energy is not as straightforward as those for the Elsässer energies because the residual energy is not a conserved quantity. The residual energy is usually but not always negative in the inertial range. To derive the nonlinear dissipation term for the residual energy in slab turbulence, Adhikari *et al.*[119] following Zank *et al.*,[18,19,70] included the Alfvén effect and the turbulent small-scale dynamo effect,[120,121] and the NI/slab timescale in the NI MHD phenomenology. In Eq. (15), the first term on the RHS is derived from a Kolmogorov phenomenology, the second and fourth terms represent the turbulent small-scale dynamo effect, and the third term represents the Alfvén effect, which is slightly modified from Zank *et al.*,[70] multiplying by $(1-\sigma_c^*)^{1/2}{M_{A0}^t}^2$ (see Zank *et al.*[19] and Adhikari *et al.*[119]) where σ_c^* is the NI/slab normalized cross-helicity, and M_{A0}^t is the turbulent Alfvén Mach number. We use $M_{A0}^t=0.1$. Notice that for unidirectional Alfvén waves, i.e., $\sigma_c^*=\pm 1$, the term $(1-\sigma_c^*)^{1/2}{M_{A0}^t}^2$ vanishes, indicating that the dissipation term associated with the Alfvén effect vanishes (further discussion can be found in the study by Zank *et al.*[19]).

For the present, in part due a desire to begin with the simplest possible models, the solar coronal heating models do not include *in situ* turbulence driving terms (or at least they are formally set to zero for now) beyond the region above the photosphere (the "low corona"), and we assume instead a steady injection of turbulence at the base. This of course corresponds to a model in which the turbulence is effectively driven at the base. The turbulence is treated as steady-state with energy injection at the base being balanced by dissipation as the turbulence decays with increasing height without replenishment. In principle, these models should connect smoothly onto existing turbulence-transport solar wind models[18,107,108,112,113,123,141,142] all of which include turbulence source terms related or extending those developed in Zank *et al.*[18,107] (i.e., stream–stream shear source terms and even pickup ion driving in the distant heliosphere). However, it is entirely possible that additional sources of turbulence exist in the lower corona, possibly associated with shear-driven instabilities as illustrated in Fig. 1, left panel, in which we suggest that shear-driven turbulence generated by, e.g., Kelvin–Helmholtz instabilities, may provide an additional source of *in situ* coronal turbulence. Related ideas have been explored recently by Ruffolo *et al.*[143] who suggest the possibility of a shear-driven transition to isotropic turbulence outside the Alfvén critical radius. Other factors not addressed in these first models presented here include super- or sub-radial expansion of the large-scale solar magnetic fields associated with coronal holes or lateral regions adjacent to coronal holes, for example. The roles of coronal instabilities and nonspherical expansion are active areas of investigation.

The coupled quasi-2D and NI/slab turbulence transport equations (10)–(17) can be used to describe any inhomogeneous spherically symmetric flow in the inner heliosphere. Large-scale fields, such as the solar wind velocity, the magnetic field through the Alfvén velocity, and even scalars like the solar wind density, and their gradients affect the evolution of quasi-2D and NI/slab turbulence. Ideally, because the large-scale flow is heated dissipatively by the evolving turbulence, one needs to couple the large-scale background flow equations and the turbulence equations. The 1D spherically symmetric steady-state continuity and the momentum equations are

$$\frac{d}{dr}\left(r^2\rho U\right)=0, \tag{18}$$

$$\rho U\frac{dU}{dr}=-\frac{dP_p}{dr}-\frac{dP_e}{dr}, \tag{19}$$

where P_p and P_e are the thermal proton and electron pressure. The electron density is assumed to be approximately equal to the proton density, i.e., $n_e\approx n_p$. Similarly, the magnetic force $(\mathbf{J}\times\mathbf{B})_r=-1/(\mu_0 r)B_\phi d/dr(rB_\phi)$ is neglected in (19) because the magnetic force produced by the Parker spiral magnetic field is negligible compared to the thermal proton and electron forces. Near the Sun, a gravitational force $GM_\odot\rho/r^2$ (G the gravitational constant, $M_\odot$ the solar mass) is present on the RHS of Eq. (19), which is negligible far from the Sun. The thermal proton and electron pressure gradients drive the solar wind.

The 1D steady-state transport equations for the proton and electron pressure in a spherical coordinate system r can be written as

$$U\frac{dP_p}{dr}+\gamma P_p\frac{dU}{dr}+2\gamma\frac{U}{r}P_p=(\gamma-1)\big(\nu_{pe}(P_e-P_p)+f_pS_t\big), \tag{20}$$

$$\begin{aligned} U\frac{dP_e}{dr}+\gamma P_e\frac{dU}{dr}+2\gamma\frac{U}{r}P_e=(\gamma-1)[\nu_{ep}(P_p-P_e)\\ -\nabla\cdot\mathbf{q}_e+(1-f_p)S_t], \end{aligned} \tag{21}$$

where S_t is a turbulent heating term, f_p and $(1-f_p)$ denote the fraction of the turbulent energy that heats the solar wind protons and electrons, respectively, $\gamma(=5/3)$ is the polytropic index, and ν_{pe} and ν_{ep} are proton–electron and electron–proton Coulomb collisional rates.[144,145] The Coulomb collision frequencies are balanced, so $n_e\nu_{ep}\approx n_p\nu_{pe}$. In Eqs. (20) and (21), the P_e-P_p term represents the Coulomb collisional term, which vanishes when $P_e=P_p$. An empirical form of the collisional proton–electron frequency is given by[146]

$$\nu_{pe}\approx 8.4\times 10^{-9}\left(\frac{n_e}{2.5\,\mathrm{cm}^{-3}}\right)\left(\frac{T_e}{10^5\,\mathrm{K}}\right)^{-3/2}s^{-1}. \tag{22}$$

In Eq. (21), $\mathbf{q}_e$ is the electron heat flux. The collisional proton heat flux[145] is generally neglected because it is insignificant compared to the turbulent heating term. An isotropic electron and proton temperature is employed because the pressure/temperature contribution is dominated by the Maxwellian core, and the parallel and perpendicular contributions to the pressure/temperature are less important.[147] However, the electron heat flux cannot be neglected.[147] The parallel electron heat flux (to the magnetic field)[146] is dominated by the electron Strahl since the Maxwellian electron core distribution does not contribute. We follow Cranmer *et al.*[146] and use an empirical formula for the electron heat flux that is derived by fitting the electron heat flux measured by Helios 2 from 0.3 to 1 au,[148] specifically

$$\ln\left(\frac{q_{||,e}}{q_0}\right) = -0.7037 - 2.115x - 0.2545x^2, \tag{23}$$

where $x \equiv \ln(r/1au)$ and $q_0 = 0.01$ erg cm^{-2} s^{-1}. Since Eq. (23) is an empirical result, this cannot describe the collisionless or collision dominated solar wind. However, it is necessary to consider the collisional characteristics of plasma when modeling the parallel electron heat flux $q_{||}$. The Spitzer and Härm[149] collisional form of the parallel heat conduction $q_{||} = -\kappa_{||}\nabla_{||}T_e(r)$ does not compare well to electron heat flux observations and yields a large temperature at 1 au. The term $\nabla\cdot\mathbf{q}_e$ can be expressed as[146]

$$\nabla\cdot\mathbf{q}_e = \frac{1}{r^2}\frac{\partial}{\partial r}\left(r^2 q_{||}\cos^2\phi\right), \tag{24}$$

where ϕ is the Parker spiral angle,

$$\tan\phi = \frac{\Omega r\sin\theta}{U},$$

and $\Omega = 2.7\times10^{-6}$ rad s^{-1} is the solar rotation frequency. We choose a colatitude $\theta = 90^\circ$ to compare the model results with PSP and Helios 2 measurements.

We distribute the dissipated turbulence energy between electrons and protons, as illustrated in Eqs. (20) and (21), respectively. By designating $f_p = 0.6$,[150] 60% of the turbulence energy is dissipated as heating for the protons and 40% for the electrons. Breech *et al.*[151] used $f_p = 0.6$ from 0.3 to 100 au, whereas Howes[152,153] and Engelbrecht and Strauss[154] assume that f_p depends on heliocentric distance. There is however no generally accepted model that describes the variation of f_p with the heliocentric distance. Accordingly, we adopt the simplest possibility. The turbulent heating term S_t derives from a von-Kármán phenomenology and is given by[51,113,119]

$$\begin{aligned}
S_t = \alpha m_p n_s\Bigg[&\frac{\langle z^{\infty+2}\rangle^2\langle z^{\infty-2}\rangle^{1/2}}{L_\infty^+} + \frac{\langle z^{\infty-2}\rangle^2\langle z^{\infty+2}\rangle^{1/2}}{L_\infty^-}\\
&+ E_D^\infty\left(\frac{\langle z^{\infty+2}\rangle^{1/2}}{\lambda_\infty^-} + \frac{\langle z^{\infty-2}\rangle^{1/2}}{\lambda_\infty^+}\right) + 2\frac{\langle z^{*+2}\rangle\langle z^{\infty+2}\rangle\langle z^{\infty-2}\rangle^{1/2}}{L_\infty^+}\\
&+ 2\frac{\langle z^{*-2}\rangle\langle z^{\infty-2}\rangle\langle z^{\infty+2}\rangle^{1/2}}{L_\infty^-} + \frac{\langle z^{*+2}\rangle^2\langle z^{*-2}\rangle^{1/2}}{L_*^+}\\
&+ \frac{\langle z^{*-2}\rangle^2\langle z^{*+2}\rangle^{1/2}}{L_*^-} + E_D^*\left(\frac{\langle z^{\infty-2}\rangle}{\lambda_\infty^+} + \frac{\langle z^{\infty+2}\rangle}{\lambda^-}\right)\\
&- \frac{\langle z^{*+2}\rangle\langle z^{\infty-2}\rangle^{1/2}}{\lambda_\infty^+} - \frac{\langle z^{*-2}\rangle\langle z^{\infty+2}\rangle^{1/2}}{\lambda_\infty^-}\\
&+ E_D^*\frac{V_A}{\lambda_*^+ + \lambda_*^-}(1-\sigma_c^*)^{1/2}{M_{A0}^t}^2\Bigg],
\end{aligned} \tag{25}$$

where m_p is the proton mass, and n_s is the solar wind proton number density.

Finally, an important component described by NI MHD is the evolution of density fluctuations. These are neither slow mode nor other forms of propagating waves but rather entropic fluctuations that correspond to $O(M_s)$ fluctuations, as described above. An evolution or transport equation for the density variance associated with density fluctuations in the solar wind $\langle\rho^{\infty 2}\rangle$ can be expressed as[18,112,113,119]

$$U\frac{d\langle\rho^{\infty 2}\rangle}{dr} + 2\langle\rho^{\infty 2}\rangle\frac{dU}{dr} + 4\frac{U}{r}\langle\rho^{\infty 2}\rangle = -\alpha\frac{\langle u^{\infty 2}\rangle^{1/2}\langle\rho^{\infty 2}\rangle}{l_u^\infty}, \tag{26}$$

where $\langle u^{\infty 2}\rangle = (\langle z^{\infty+2}\rangle + \langle z^{\infty-2}\rangle + 2E_D^\infty)/4$ is the quasi-2D fluctuating kinetic energy, $l_u^\infty = [(E_T^\infty + E_C^\infty)\lambda_\infty^+ + (E_T^\infty - E_C^\infty)\lambda_\infty^- + E_D^\infty\lambda_D^\infty]/2(E_T^\infty + E_D^\infty)$ is the correlation length of the quasi-2D fluctuating kinetic energy, and E_C^∞ is the quasi-2D cross-helicity. Notice that the evolution of the density variance $\langle\rho^{\infty 2}\rangle$ depends only on the leading-order 2D velocity fluctuations and correlation length and behaves as a passive scalar.

B. Comparing PSP observations with solar wind turbulence models

PSP gives us an excellent opportunity to investigate the bulk and turbulence properties of the inner fast and slow solar wind and relate the observations directly to the basic turbulence-driven solar wind theoretical model described in Sec. III A. The fast and slow solar wind streams observed by PSP during its first encounter in the outbound direction are clearly visible in Fig. 7. As illustrated in Fig. 1, we may interpret the fast solar wind as originating from a coronal hole in the open field region, whereas the slow solar wind originates from the solar equatorial region in the vicinity of closed magnetic field regions.

The comparison below between the turbulence transport models and observations derived from PSP can be summarized as follows. (i) The slow wind comparison (Sec. III B 1) is based on a model that integrates the turbulence transport equations from ∼35.5 $R_\odot$ using PSP observations made at perihelion as the inner boundary. Hence, this is above the Alfvén surface and in the super-Alfvénic solar wind. (ii) The fast solar wind comparison (Sec. III B 2) begins from 1 $R_\odot$ but the turbulence transport model (and hence boundary conditions) that is coupled to the large-scale flow model includes only the dominant quasi-2D turbulence component and outwardly propagating minority Alfvén wave fluctuations [one can show that a purely outward (or inward) Alfvén wave energy equation can be derived from the slab transport equations[40] if $z^{*-} = 0$ and $E_D^* = 0$]. The purpose of this subsection is to illustrate that the coupled turbulence-driven solar wind model can generate a fast solar wind within ∼3–4 $R_\odot$ and provide the required high coronal temperatures. (iii) The full turbulence transport model of Sec. III A 2 that includes both the dominant quasi-2D and minority slab components as well as electrons in the coupled large-scale flow model is solved in Sec. III B 3 from ∼45 $R_\odot$ to 1 au with the inner boundary conditions drawn from the first PSP encounter. The subsequent model is therefore in super-Alfvénic flow exclusively and is compared to PSP and Helios data drawn from the super-Alfvenic solar wind.

1. Transport of turbulence in the slow solar wind

Adhikari *et al.*[118] described the transport of low frequency turbulence observed in the slow solar wind by Parker Solar Probe during the first orbit, interpreting the observations using the NI MHD turbulence transport model equations presented in Sec. III A.

TABLE I. Boundary values at 0.165 au (35.55 $R_\odot$) as measured by PSP at its closest approach to the Sun during the first encounter.[118]

2D core model equations		Slab model equations	
$\langle z^{\infty+2}\rangle$	$9338.4\,\mathrm{km^2\,s^{-2}}$	$\langle z^{*+2}\rangle$	$2334.6\,\mathrm{km^2\,s^{-2}}$
$\langle z^{\infty-2}\rangle$	$952.4\,\mathrm{km^2\,s^{-2}}$	$\langle z^{*-2}\rangle$	$238.1\,\mathrm{km^2\,s^{-2}}$
E_D^∞	$-112.48\,\mathrm{km^2\,s^{-2}}$	E_D^*	$-28.12\,\mathrm{km^2\,s^{-2}}$
L_∞^+	$5.19\times10^8\,\mathrm{km^3\,s^{-2}}$	L_*^+	$2.59\times10^8\,\mathrm{km^3\,s^{-2}}$
L_∞^-	$5.44\times10^7\,\mathrm{km^3\,s^{-2}}$	L_*^+	$2.72\times10^7\,\mathrm{km^3\,s^{-2}}$
L_D^∞	$-1.34\times10^8\,\mathrm{km^3\,s^{-2}}$	L_D^*	$-6.7\times10^7\,\mathrm{km^3\,s^{-2}}$
$\langle \rho^{\infty 2}\rangle$	$2.83\times10^3\,\mathrm{cm^{-6}}$		
T	$1.75\times10^5\,\mathrm{K}$		

The turbulence transport model assumed a constant radial solar wind speed U and included a stream-shear source of turbulence. The turbulence transport model equations and the temperature equation were solved between 35.5 and 131.64 $R_\odot$ to be consistent with PSP measurements. A fourth-order Runge–Kutta method was used to solve the coupled system of turbulence transport equations with an assumed solar wind velocity profile. The relevant boundary conditions are shown in Table I, and these values are derived from PSP measurements. We assume an 80:20 ratio between the quasi-2D and slab turbulence[19,110] to obtain suitable boundary conditions for the majority quasi-2D and minority slab Elsässer energies and residual energy. Similarly, we obtain the boundary conditions for the correlation function by assuming that the ratio between the quasi-2D and slab correlation function is 2:1.[155] The parameter values used in the coupled turbulence transport model equations are shown in Table II.

Reasonable agreement between PSP measurements and theory can be seen from Fig. 10. The various turbulent quantities were derived from PSP measurements using a now well-established approach.[107,112,113,122,123,156]

Figure 10 compares the PSP SWEAP measurements and theoretical solutions for the solar wind proton temperature, the fluctuating density variance, the velocity correlation length, and the turbulent kinetic energy. Two curves show the theoretical proton temperature, with the black curve assuming that 40% of the turbulence energy is dissipated in heating the protons and the blue curve corresponds to assuming 30% of the turbulence energy is dissipated in proton heating. The temperature change with the heliocentric distance scales approximately as $r^{-0.9}$ and $r^{-0.95}$ for the two curves, which of course is slower than adiabatic cooling. This dissipation/heating fraction is rather less than used by Breech *et al.*[151] as discussed above. Adhikari *et al.*[118] suggested that the remaining energy in turbulent fluctuations is used to both heat thermal electrons and possibly energize a nonthermal or energetic particle component via turbulent energization (e.g., Refs. 157–159). The top right panel of Fig. 10 is a comparison of the theoretical (solid curve) and observed (red diamonds with error bar) fluctuating density variance as a function of heliocentric distance. The observed and theoretical dependence with r is in reasonable accord, with the theoretical dependence being $\sim r^{-2.98}$. The bottom left panel of Fig. 10 shows the fluctuating kinetic energy as a function of heliocentric distance in the same format except that the solid line identifies the theoretical fluctuating quasi-2D kinetic energy, the dashed line the theoretical fluctuating NI/slab kinetic energy, and the dashed-dotted-dashed curve the total (quasi-2D plus NI/slab) fluctuating kinetic energy. The theoretical fluctuating quasi-2D, NI/slab, and total kinetic energy decrease according to $r^{-1.62}$, $r^{-1.18}$, and $r^{-1.47}$ with increasing distance, respectively. The observed and theoretical models for the fluctuating kinetic energy are in reasonable agreement. However, we find that in the slow solar wind flow, the observed turbulent kinetic energy (i.e., the total kinetic energy in fluctuations as observed by PSP) matches quite well the predicted behavior of the theoretical quasi-2D turbulence energy. By contrast, in the fast solar wind flow, the observed fluctuating kinetic energy better matches the predicted behavior of the theoretical NI/slab turbulence energy [see Fig. 16 and Fig. 3(c) of Adhkari *et al.*[40]] for the reasons discussed above regarding the alignment of the radial flow with the magnetic field. Finally, the kinetic energy correlation length is shown as a function of heliocentric distance in the bottom right panel of Fig. 10. Two curves are plotted, corresponding to the quasi-2D fluctuating kinetic energy (solid curve) and the slab fluctuating kinetic energy (dashed curve). The former increases until $\sim$65 $R_\odot$ and then decreases slightly with increasing distance unlike the slab correlation length that increases gradually with the heliocentric distance.

TABLE II. Model parameters for the turbulence transport equations.[118]

Parameters	Values	Parameters	Values
C_{sh}^+	0.25	C_{sh}^{+*}	0.2
C_{sh}^-	0.1	C_{sh}^{-*}	0.05
$C_{sh}^{E_D}$	-0.006	$C_{sh}^{E_D*}$	-0.003
U	$380.0\,\mathrm{km\,s^{-1}}$	η_1	0.8
ΔU	$200.0\,\mathrm{km\,s^{-1}}$	b	0.26
V_{A0}	$101.37\,\mathrm{km\,s^{-1}}$	α	0.1
r_0	0.165 au	n_{sw}	232.34

We extend the analysis of Adhkari *et al.*[40] by including a comparison of the model results with the magnetic field fluctuations. Illustrated in Fig. 11 are plots of the Elsässer energies $\langle z^{\infty,*\pm 2}\rangle$ for the quasi-2D and slab components, together with the total Elsässer energy density $\langle z^{\pm 2}\rangle_{tot}$. As discussed above, the magnetic field was not aligned with the flow vector, implying that the quasi-2D component was able to be measured by PSP. The solid line depicts the predicted evolution with heliocentric distance of the quasi-2D component and the dashed line the slab component. The dash-dotted line shows the

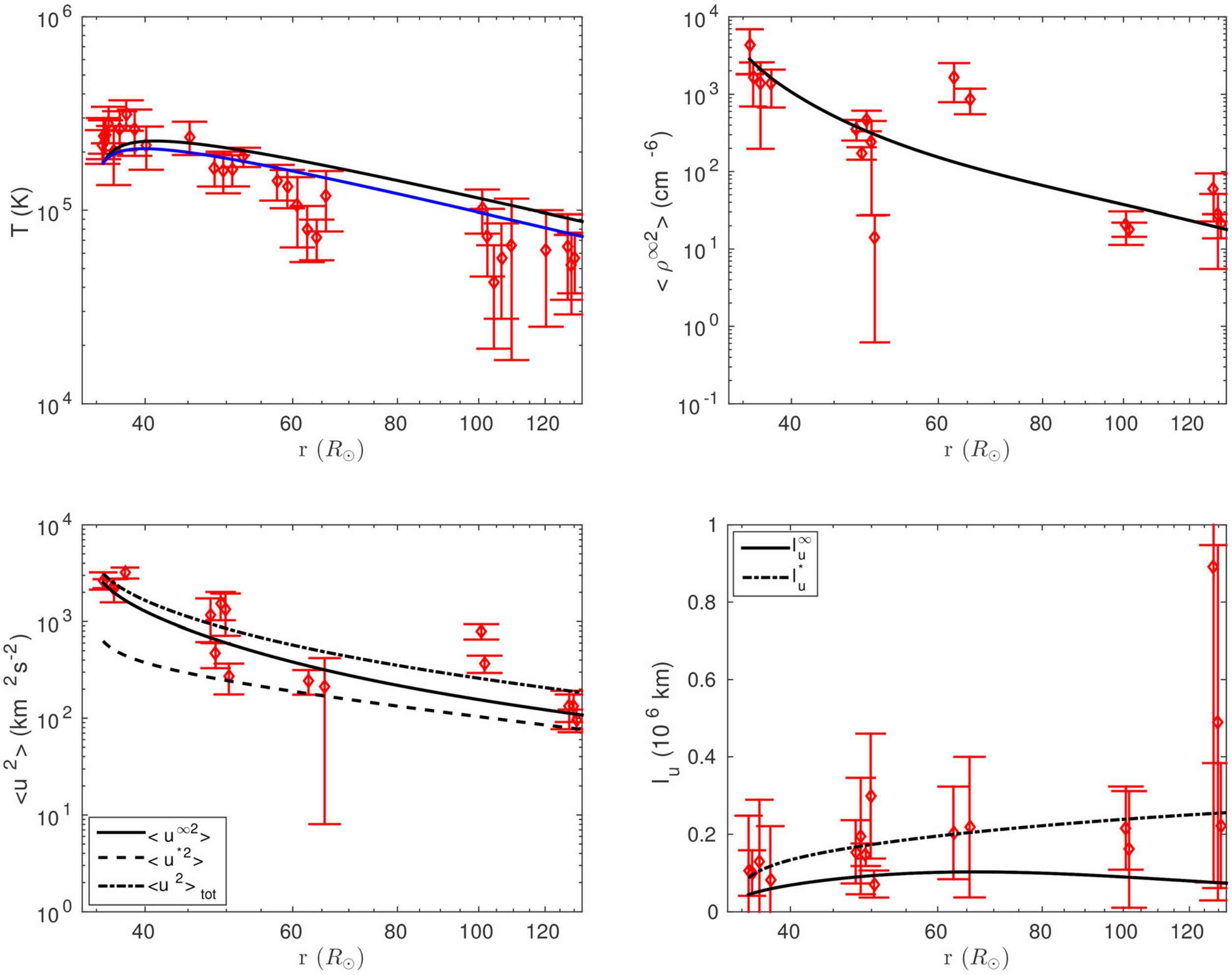

FIG. 10. Comparison between the theoretical results and PSP measurements in the slow solar wind flow as a function of heliocentric distance. Top left: solar wind proton temperature; top right: fluctuating density variance; bottom left: fluctuating kinetic energy. Bottom right: correlation length of velocity fluctuations. Reproduced with permission from Adhikari *et al.*, Astrophys. J. Suppl. Ser. **246**, 38 (2020).[118] Copyright 2020 IOP Publishing.

total Elsässer energy density, clearly dominated theoretically by the quasi-2D component. The observational Elsässer energy density derived from PSP plasma and magnetic field data are plotted as the red points with error bars. The total energies $E_T^{\infty,*} \equiv (\langle z^{\infty,*+2}\rangle + \langle z^{\infty,*-2}\rangle)/2$ and $E_T^{tot} \equiv E_T^{\infty} + E_T^{*}$ are plotted in the middle left panel, and good agreement with the observed and theoretical quasi-2D and total energy is shown. The observed Elsässer and total energies are consistent with the quasi-2D and total energy predictions, indicating that the turbulence is dominated by quasi-2D fluctuations and not by slab turbulence. This is further illustrated by the normalized residual energy plot in Fig. 11 that shows departures from 0 (which would be expected for slab turbulence dominated by Alfvénic fluctuations). The normalized cross helicity decreases from 1, indicating that the energy flux is not uni-directional.

The left panel of Fig. 12 shows the magnetic field variance for the quasi-2D, slab, and total fluctuations. The observed magnetic field variance tracks the predicted quasi-2D (and total) values closely. The slab variance is roughly a factor 3.5 smaller than the quasi-2D contribution. The observed and predicted quasi-2D magnetic correlation length ℓ_B are consistent too.

The modeled and observed correlation lengths for the forward, backward, and residual energy as a function of increasing heliocentric distance are illustrated in Fig. 13. The observed forward and backward correlation lengths appear to be consistent with the corresponding quasi-2D models. The observed residual energy correlation length tracks the modeled quasi-2D and slab curves less well although the overall dependence with the heliocentric distance is similar.

2. Transport of turbulence and dissipative heating in the fast solar wind

The analysis presented in Sec. III B 1 assumed a constant prescribed background solar wind speed. Here, we discuss a coupled turbulence-driven solar wind model[40] for the fast solar wind flow in

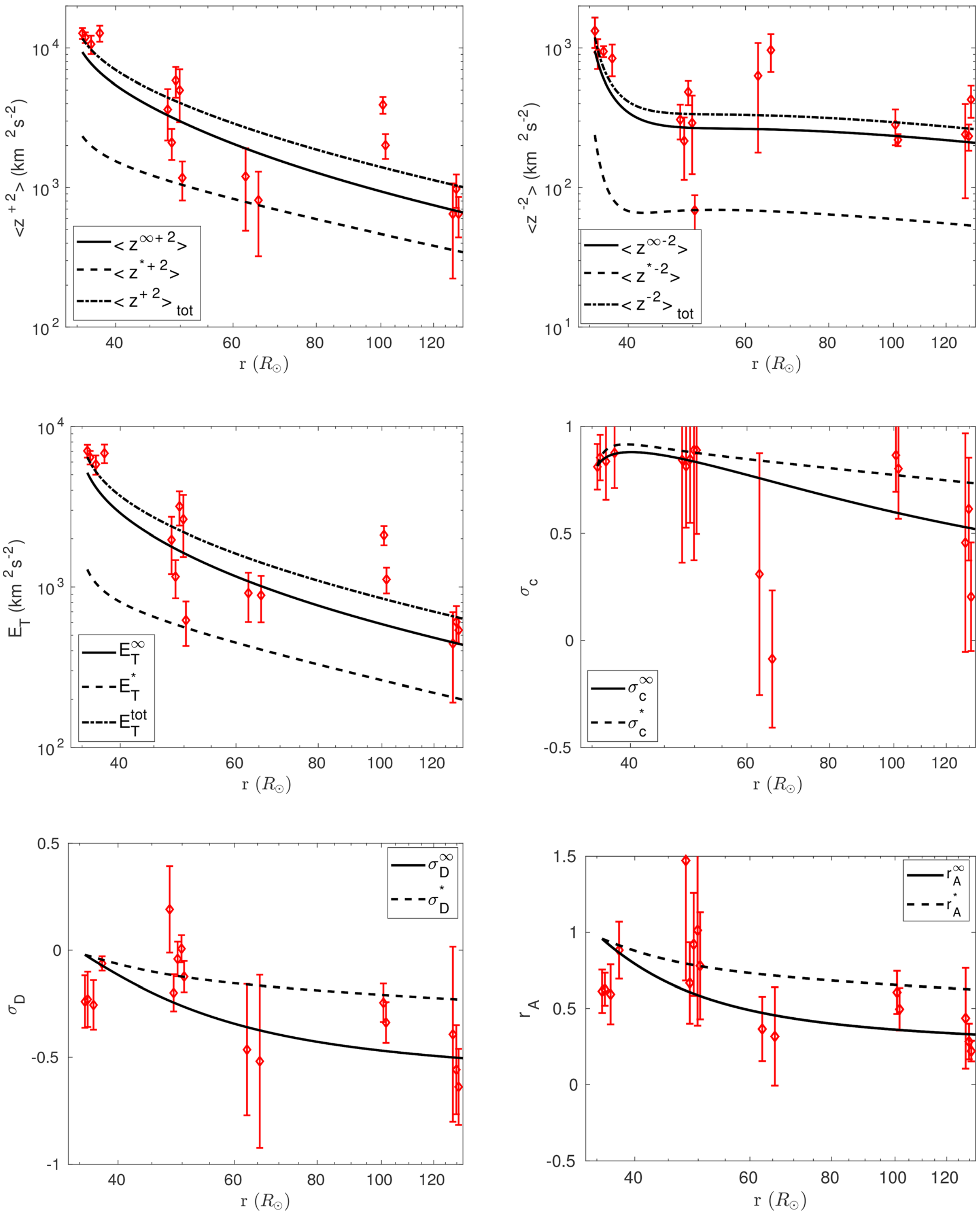

FIG. 11. The top two panels show the Elsässer energy density in forward and backward modes, broken into the dominant quasi-2D components $\langle z^{\infty\pm2}\rangle$ (solid line), the slab components $\langle z^{*\pm2}\rangle$ (dashed line), and the total $\langle z^{\pm2}\rangle_{tot}$ (dash-dotted line) as a function of increasing heliocentric distance. The middle left panel shows the total energies $E_T^{\infty,*,tot}$ in the same format. The normalized cross helicity $\sigma_c^{\infty,*}$, normalized residual energy $\sigma_D^{\infty,*}$, and Alfvén ratio $r_A^{\infty,*}$ for the majority 2D component and the minority slab component is plotted as a function of heliocentric distance in the right middle panel, bottom left panel, and right bottom panel in the same format. The red diamonds denote the derived solar wind observations with error bars. Reproduced with permission from Adhikari *et al.*, Astrophys. J. Suppl. Ser. **246**, 38 (2020).[118] Copyright 2020 IOP Publishing.

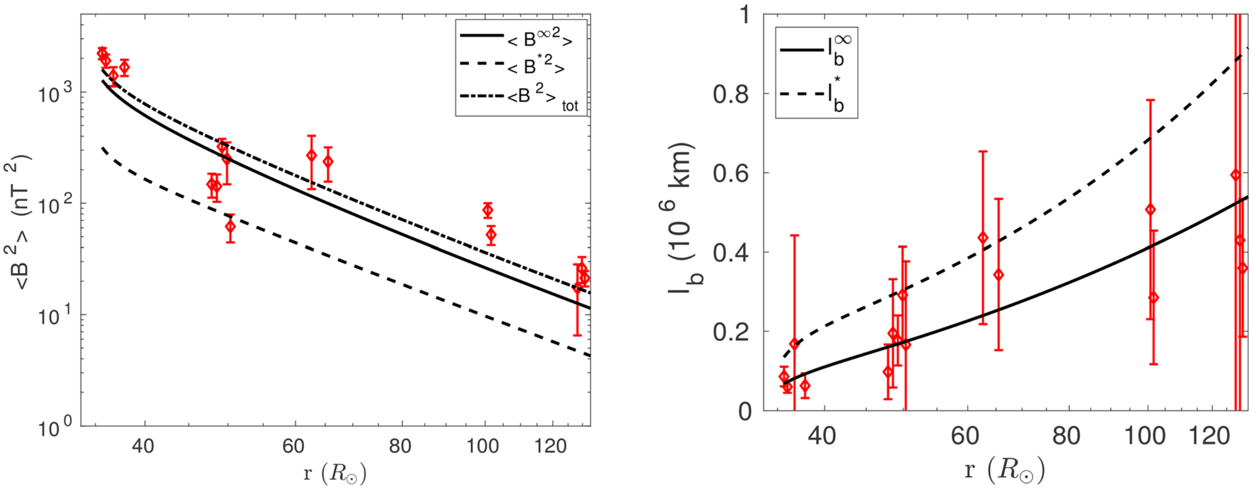

FIG. 12. The left panel shows the predicted quasi-2D, slab, and total magnetic field variance $\langle B^{\infty,*2}\rangle$ and $\langle B^2\rangle_{tot}$ as a function of increasing heliocentric distance using the same plotting convention as in Fig. 11. The right panel shows the magnetic correlation length ℓ_B as a function of heliocentric distance. The red diamonds denote the derived solar wind observations with error bars. Reproduced with permission from Adhikari *et al.*, Astrophys. J. Suppl. Ser. **246**, 38 (2020).[118] Copyright 2020 IOP Publishing.

open field regions that can be compared to observations made by PSP during periods when the solar wind flow is highly aligned with the magnetic field. The turbulence transport model is based on NI MHD as described in Sec. III A and is coupled to the large-scale flow model. However, both the turbulence transport model and the large-scale flow equations are simplified slightly in that only the dominant quasi-2D turbulence component and outwardly propagating minority Alfvén wave fluctuations [one can show that a purely outward (or inward) Alfvén wave energy equation can be derived from the slab transport equations[40] if $z^{*-} = 0$ and $E_D^* = 0$] are included and we neglect the contribution of electrons. Consequently, because the quasi-2D component is an advected quantity and only outward propagating Alfvén waves are present, nothing special has to be done physically or numerically at the Alfvén point in the solutions. Here, the focus on the heating of protons to illustrate that the coupled turbulence-driven solar wind model can generate a fast solar wind within ~3–4 $R_\odot$ and provide the required high coronal temperatures.

We consider the evolution of the solar wind and low-frequency turbulence in the fast wind from 1 to 100 $R_\odot$. The coupled solar wind (fluid equation description only) and turbulence transport equations are solved using a fourth-order Runge–Kutta method, and we use PSP fast solar wind measurements to compare observations and model results. The boundary conditions are listed in Table III. The boundary conditions at the coronal base are chosen in such a way that the numerical solutions of the model are reasonable and yield results consistent with PSP measurements. Since the momentum equation introduces a sonic point, we use L'H ô pital's rule to integrate the system of equations near and through the sonic point.

Consider fast solar wind flow measurements made by PSP during four 2018 intervals with start and end times (DOY:HR:MN): (312:13:0.378–313:8:46.54), (318:1:56.62–319:5:54.51), (319:21:25.64 –321:7:59.89), and (323:7:7.16–324.0.46:27.35).

Figure 14(a) compares the observed and theoretical radial solar wind speed U (solid curve), Alfvén velocity V_A (dashed curve) and sound speed from 1 to 100 $R_\odot$. Diamonds with error bars denote observed quantities, and the error bar indicates the inter-quartile range. The solar wind speed is predicted to increase rapidly from the base of the solar corona to 4 $R_\odot$ and then more slowly ($r^{0.14}$) until 100 $R_\odot$. Good agreement is shown with the observed solar wind speed. The Alfvén velocity increases from ~900 km/s at the coronal base to

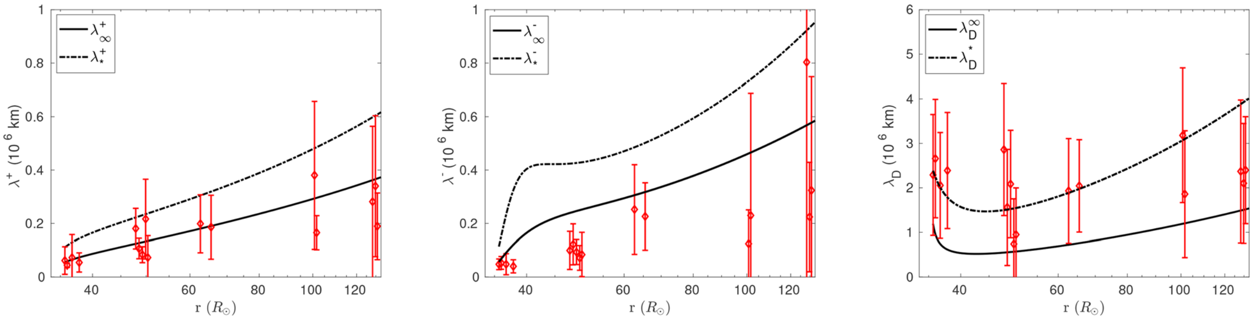

FIG. 13. From left to right, the panels show the correlation lengths $\lambda^{\pm}_{\infty,*}$ and $\lambda_D^{\infty,*}$ as a function of heliocentric distance using the same convention as in Fig. 11. The red diamonds denote the derived solar wind observations with error bars. Reproduced with permission from Adhikari *et al.*, Astrophys. J. Suppl. Ser. **246**, 38 (2020).[118] Copyright 2020 IOP Publishing.

TABLE III. Boundary values at 1 R$_\odot$ for the turbulent quantities and the solar wind parameters.[40]

Parameters	Values	Parameters	Values
$\langle z^{\infty+2}\rangle$ (km^2 s^{-2})	5.8×10^5	$\langle z^{*-2}\rangle$ (km^2 s^{-2})	1100
$\langle z^{\infty-2}\rangle$ (km^2 s^{-2})	5.8×10^5	L_*^+ (km^3 s^{-2})	1.76×10^8
E_D^∞ (km^2 s^{-2})	2000	U (km s^{-1})	13.56
L_∞^+ (km^3 s^{-2})	4.64×10^{10}	n (cm^{-3})	1.0×10^7
L_∞^- (km^3 s^{-2})	4.64×10^{10}	T (K)	5×10^5
L_D^∞ (km^3 s^{-2})	1.6×10^8	$\langle\rho^{\infty2}\rangle$ (cm^{-6})	2×10^{11}

about $\sim2.79\times10^3$ km/s at 1.2 R$_\odot$, after which it decreases gradually. The Alfvén surface, at which $U=V_A$, is located at $\sim$11.7 R$_\odot$. The observed Alfvén velocity (blue diamonds) beyond the Alfvén surface matches the theoretical expectation. The dashed-dotted-dashed curve shows the sound speed, and the sonic point is located at $\sim$1.78 R$_\odot$.

The observed (red diamonds) and theoretical (solid curve) solar wind proton temperature is plotted in Fig. 14(b). The proton temperature increases from 5×10^5 K at the coronal base to $\sim3.5\times10^6$ K within 2 R$_\odot$ and then decreases gradually with increasing distance (see the inset). The reason for the rapid increase in temperature is the dissipation of primarily advected quasi-2D turbulence[17] and not slab/Alfvénic turbulence. The theoretical solar wind proton temperature is in reasonable agreement with the observed solar wind proton temperature between $\sim$35 and $\sim$50 R$_\odot$ but is higher than that observed between 70 and 100 R$_\odot$. Here, we have assumed that 80% of the turbulent energy heats the solar wind coronal plasma in the fast solar wind.

Not too surprisingly, the observed and theoretical densities are in good agreement [Fig. 14(c)] since the solar wind flow speed is roughly constant beyond $\sim$10 R$_\odot$, and the theoretical expansion corresponds to $\sim r^{-2.14}$ between 35.5 and 100 R$_\odot$. Finally, Fig. 14(d) shows the radial profiles of the heating rates[40] associated with quasi-2D and slab turbulence, the former dominating in the subsonic part of the solar wind and being responsible for heating the corona to temperatures in excess of 10^6 K.

Rather than discussing the transport of turbulence on the basis of this coupled solar wind-turbulence model, we present our currently most detailed coupled model in the Sec. III B 3 and include a discussion of the turbulence characteristics there.

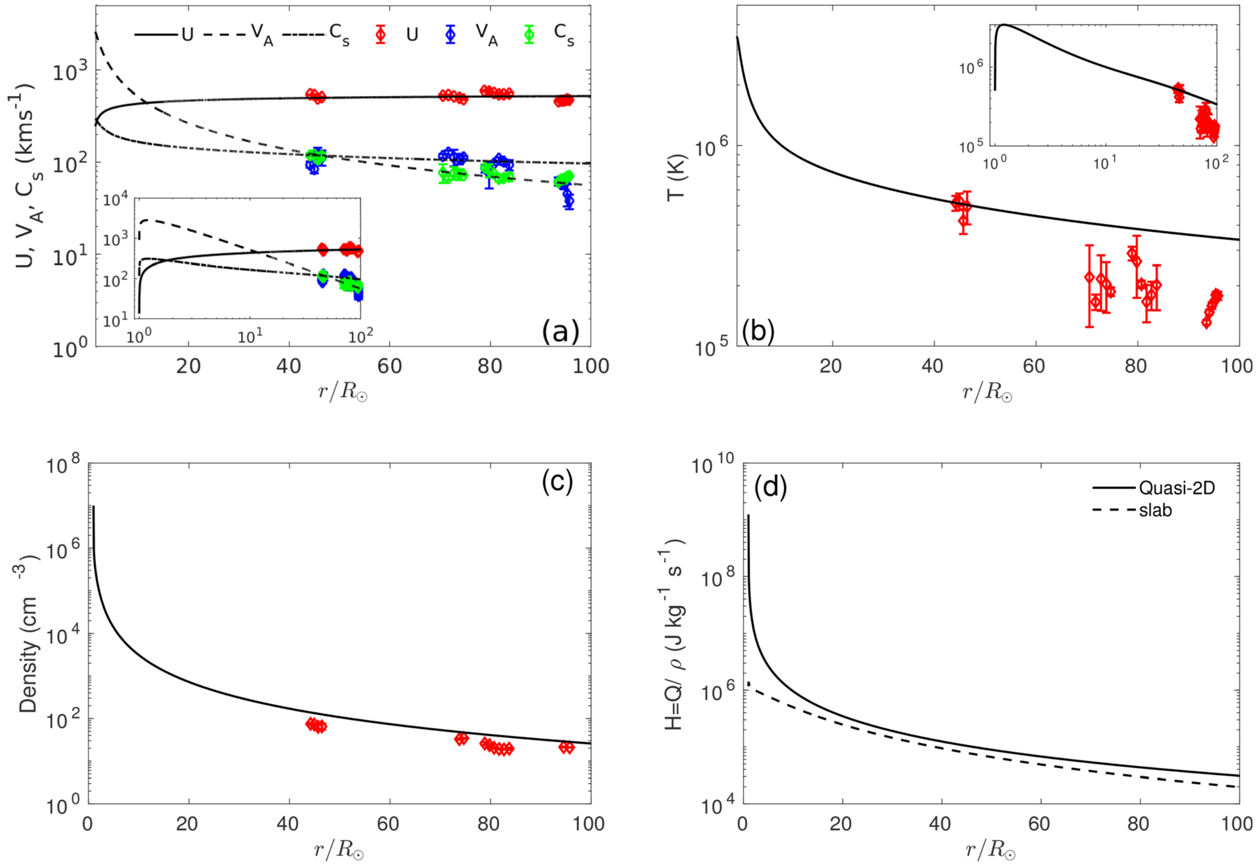

FIG. 14. The panels show (a) (solid curve), the Alfvén speed (dashed curve), and the sound speed (dashed-dotted-dashed curve); (b) the solar wind proton temperature (solid curve); (c) the solar wind density (solid curve), and (d) the heating rate of quasi-2D (solid curve) and NI/slab (dashed curve) turbulence as a function of heliocentric distance. The red diamonds denote the corresponding observed solar wind parameters with error bars. Reproduced with permission from Adhikari *et al.*, Astrophys. J. **901**, 102 (2020).[40] Copyright 2020 IOP Publishing.

3. Inclusion of electron physics

As discussed in Sec. III A, electrons can be incorporated phenomenologically in a Parker-like solar wind model that is coupled to a set of turbulence transport equations. A phenomenological choice for the ratio of the distribution of the dissipated turbulence energy to heat protons and electrons must be made. Following precedent, we adopt a ratio of 60:40.[119,155] The coupled solar wind driven-turbulence model is solved from 45.15 to 215 $R_\odot$, and the theoretical results are compared with PSP SWEAP[3] and FIELDS[2] observations, as well as Helios 2 measurements. The PSP measurements comprise the four intervals listed in Sec. III B 2 above. In 1976, Helios 2 sampled three high-speed streams at 0.29, 0.65, and 0.87 au that originated from the same source on the Sun.[160] We use the Helios 2 observations to extend the fast solar wind comparison with the theoretical model. For the PSP and Helios 2 observations, we restrict our attention to data that satisfy the following two criteria: (i) the angle between the large-scale mean flow and the magnetic field should be less than 20° ($\theta_{UB} < 20^\circ$) or greater than 160° ($\theta_{UB} > 160^\circ$) and (ii) the mean square fluctuations of the velocity, magnetic field, solar wind density, and solar wind temperature should be less than the square of their mean fields to avoid data associated with shocks and other embedded structures.

In solving the coupled solar wind-turbulence transport model with electrons, we use the same procedure described above, i.e., a fourth-order Runge–Kutta method with the boundary conditions shown in Table IV.

In the top left panel of Fig. 15, we compare the observed solar wind proton (red and blue squares) and electron temperatures (pink and green triangles) to their predicted values (solid and dashed curves, respectively). The theoretical solar wind proton temperature is a power law in heliocentric distance r, $r^{-0.66}$, whereas the theoretical solar wind electron temperature flattens after $\sim$120 $R_\odot$, being $r^{-0.54}$ between $\sim$44.5 and $\sim$150 $R_\odot$, and $r^{-0.24}$ between $\sim$150 and 215 $R_\odot$.[161] Proton and electron entropy plots are shown in the top right panel of Fig. 15. Observationally and theoretically, both increase with increasing heliocentric distance as expected from the dissipation of turbulence, and the theory and the two sets of observations are consistent.[119] The bottom left panel shows the observed and predicted radial solar wind speed. A modest increase in speed is predicted but it is basically constant with $U \sim 520$ km/s. There is some scatter in the PSP and Helios 2 radial speeds. Finally, as expected, the observed and predicted density profiles are in good agreement, as illustrated in the bottom right panel of Fig. 15.

Consider now the transport of low frequency MHD turbulence in the inner heliosphere for the fast wind as illustrated in Fig. 16. The top two panels show the energy in forward and backward propagating fluctuations as measured by the Elsässer variables $\langle z^{\pm 2} \rangle$ as a function of heliocentric distance. Unlike the slow wind example discussed in Sec. III B 1, the large-scale background solar wind flow is not prescribed but instead is coupled to the turbulence model. In Fig. 16, we plot turbulence quantities derived from both PSP and Helios 2 observations (red and blue squares with error bars, respectively). Two theoretical curves are shown, with the solid curve corresponding to the majority 2D turbulence component and the dashed curve to the minority slab component. It is important to emphasize again that the PSP observations particularly are made frequently in fast magnetic field-aligned flows and consequently only slab or Alfvénic fluctuations can be measured, since quasi-2D fluctuations are effectively invisible to the spacecraft. Consequently, comparison of theory and observations means that it is likely possible on many occasions that only the slab predictions of NI MHD turbulence should be compared to the observations made by PSP (and Helios 2). The energy in forward and backward Elsässer modes does appear to be consistent with the slab/NI component rather than the 2D component, despite the 2D component dominating energetically and being primarily responsible for the heating of the corona. The bottom left plot shows the normalized residual energy. The relative smallness of the observed normalized residual energy indicates that slab or Alfvénic turbulence is being measured, and this is evidently consistent with the dashed curve prediction of the NI MHD theory. By contrast, the dominant quasi-2D component that is unable to be measured by PSP in this particular geometry evolves from a state of $\sigma_D \sim 0$ (fluctuating kinetic and magnetic energy being almost equal) to one dominated by magnetic field fluctuations. The remaining panel shows the normalized cross helicity observed by PSP and Helios 2, together with the predicted quasi-2D and slab values. The observed values, which agree well with the slab predictions, give high values of σ_c from $\sim$0.9 to 0.8, indicating an almost entirely uni-directional energy flux. This is consistent with the prior discussion (Sec. II B) of PSP-observed uni-directional Alfvén wave propagation and Kolmogorov-like spectra $E(k_\|) \propto k_\|^{-5/3}$.

TABLE IV. Boundary values for solar wind parameters and turbulence quantities at 0.21 au (45.15 $R_\odot$). We assume the electron density is approximately equal to the proton density, $n_e \approx n_p$. The proton thermal pressure is determined by $P_p = n_p k_B T_p$ and the electron thermal pressure is determined by $P_e = n_e k_B T_e$, where k_B is Boltzmann's constant.[119]

Parameters	Values	Parameters	Values
$\langle z^{\infty +2} \rangle$	$35\,008$ km^2 s^{-2}	$\langle z^{* +2} \rangle$	$17\,019.3$ km^2 s^{-2}
$\langle z^{\infty -2} \rangle$	3179.6 km^2 s^{-2}	$\langle z^{* -2} \rangle$	907.96 km^2 s^{-2}
E_D^∞	-1134 km^2 s^{-2}	E_D^*	-51.3 km^2 s^{-2}
L_∞^+	1.1×10^{10} km^3 s^{-2}	L_*^+	1.14×10^9 km^3 s^{-2}
L_∞^-	1.46×10^9 km^3 s^{-2}	L_*^-	1.53×10^8 km^3 s^{-2}
L_D^∞	-6.12×10^9 km^3 s^{-2}	L_D^*	-1.72×10^8 km^3 s^{-2}
U	530 km s^{-1}	n_p	75.55 cm^{-3}
T_e	3×10^5 K	T_p	5.15×10^5 K
$\langle \rho^{\infty 2} \rangle$	60 cm^{-6}		

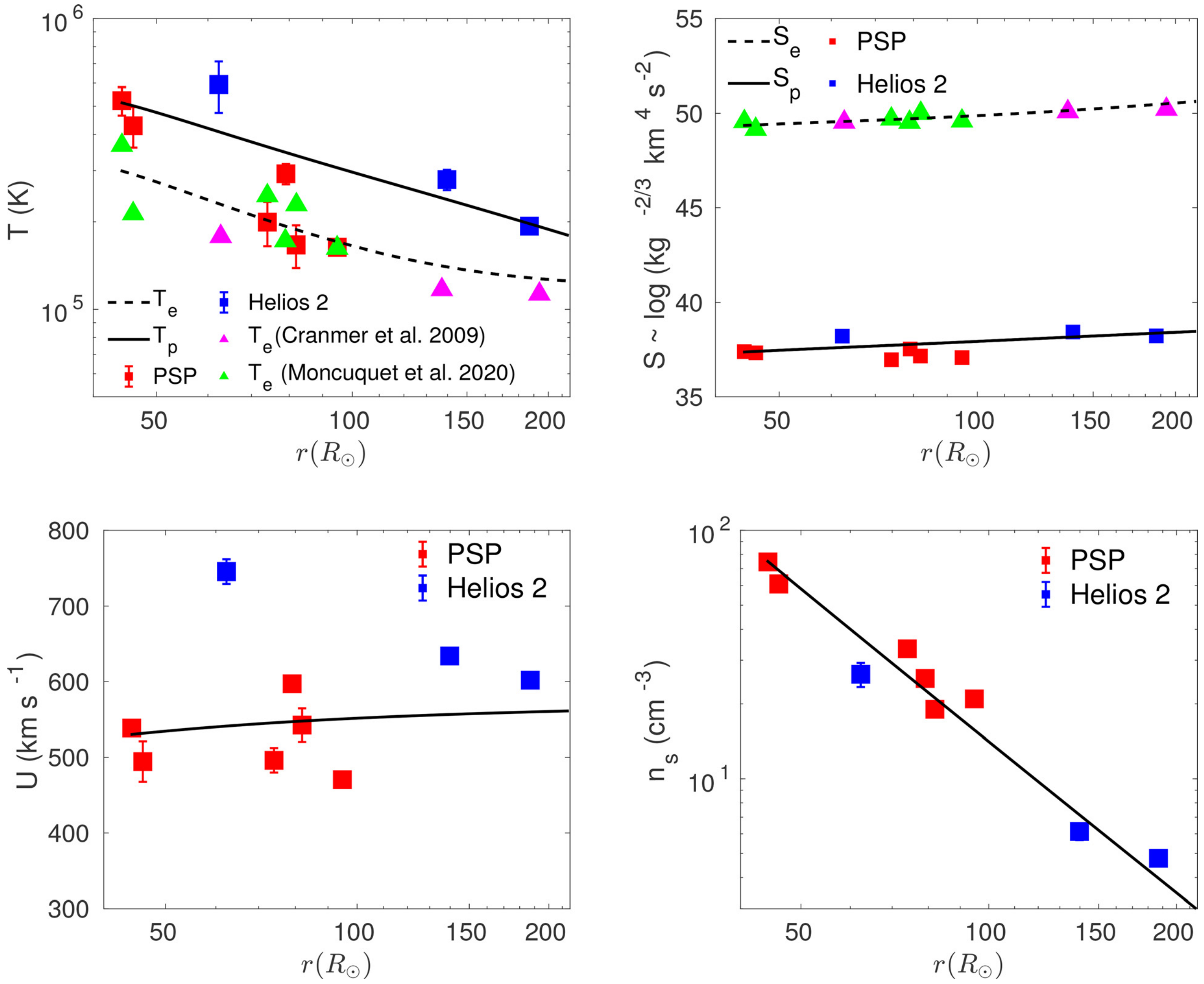

FIG. 15. PSP (red squares with error bars) and Helios 2 (blue squares) observations of solar wind plasma parameters as a function of heliocentric distance compared to a coupled proton–electron solar wind-turbulence model (solid and dashed curves). Top left: the solar wind electron and proton temperature. Top right: the solar wind proton and electron entropy. Bottom left: the solar wind speed. Bottom right: the solar wind density. Reproduced with permission from Adhikari *et al.*, Astron. Astrophys. **650**, A16 (2021).[119] Copyright 2021 EDP Sciences.

Finally, we compare the observed and theoretical correlation lengths for the forward and backward propagating modes, as shown in the left and right panels of Fig. 17. As before, the solid and dashed curves show the theoretical quasi-2D and NI/slab predictions, respectively. From the discussion above, the observationally derived PSP and Helios 2 correlation lengths should be compared to the predicted slab correlation lengths and not the quasi-2D correlation lengths, The agreement is quite satisfactory, and both the quasi-2D and slab correlation lengths increase with increasing heliocentric distance.

Shown in Fig. 18 are the corresponding figures for the fluctuating magnetic field variance $\langle B^2 \rangle$, fluctuating kinetic energy $\langle u^2 \rangle$, both for the theoretical 2D and slab components and the PSP and Helios 2 observations at different heliocentric distances. The agreement of the observed $\langle B^2 \rangle$ with the slab model is excellent, whereas the kinetic energy observations and theory are less convincing. Finally, the comparison of the observed and predicted density variance $\langle \rho^2 \rangle$ is very good. Recall that the transport of the density variance is governed by the quasi-2D velocity fluctuations and the slab-associated velocity fluctuations do not enter the theoretical passive scale transport of the entropic density fluctuations.

IV. CONCLUSIONS

Although the Parker Solar Probe has not yet crossed the Alfvén surface, plasma and magnetic measurements of turbulence are beginning to constrain coronal heating and solar wind driving models, particularly those that appeal directly to some form of turbulence dissipation to heat the solar corona. This review focused on two classes of models advanced to describe turbulence in the corona and inner heliosphere, these being a model dominated by Alfvén waves interacting nonlinearly ("slab" or Alfvénic turbulence) or one dominated by

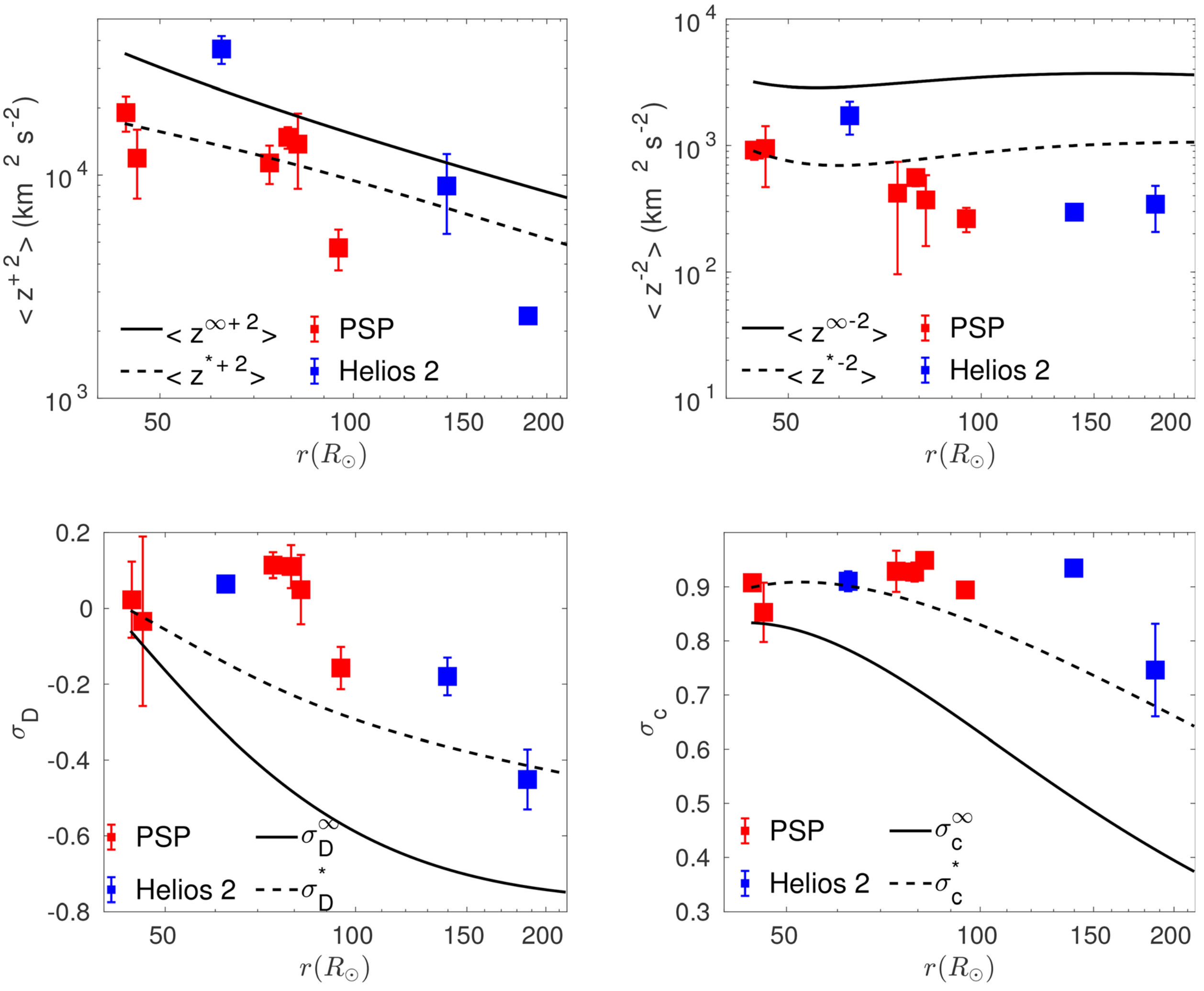

FIG. 16. Top left and right panels show the observed (squares with error bars) and predicted (solid and dashed curves) energy in forward and backward propagating modes. Bottom left and right panels show the normalized residual energy and the normalized cross-helicity. The solid curve represents the quasi-2D component and the dashed curve the slab component. Red and blue squares are PSP and Helios 2 observations with error bars, respectively. Reproduced with permission from Adhikari *et al.*, Astron. Astrophys. **650**, A16 (2021).[119] Copyright 2021 EDP Sciences.

nonpropagating quasi-2D turbulent fluctuations that interact nonlinearly plus a coupled minority slab or Alfvénic turbulence component. Before turning to how well the specific models address the new constraints introduced by PSP observations, we recapitulate the possible origin of the two classes of fluctuations. The wave-turbulence model assumes that a broad spectrum of Alfvén waves is excited by rapid displacements of open magnetic flux tubes advected by motion in the photosphere.[10] As discussed in Sec. I above, the drawback with this model is that the transition region is very effective in limiting Alfvén wave propagation from the chromosphere into the corona and so a very large Alfvénic flux needs to propagate away from the photosphere in order to achieve the canonical coronal energy flux of 5×10^5 ergs cm^{-2} s^{-1} thought to be necessary to heat the corona to temperatures high enough to drive the supersonic solar wind. The quasi-2D turbulence model is not subject to this difficulty since the majority quasi-2D component is advected by the background flowing gas and is not reflected at the transition layer. It has been argued[17] that the dynamical interaction of mixed polarity small-scale loops that rise from below the photosphere with an ∼40 h replenishment timescale[15] generate quasi-2D turbulence over some scale height about the photosphere. We mention in Sec. I a possible alternative mechanism for the generation of quasi-2D turbulence in the chromosphere due to the reflection of incident Alfvén waves by the transition region. The counterpropagating chromospheric Alfvén waves will generate 2D turbulence via the usual resonant three-wave interaction[58] of incompressible fluctuations in the inertial range. The generated 2D turbulence could be advected through the transition region and act to heat the solar corona. This process has yet to be worked out in sufficient detail.

Consider now the list of predictions for the quasi-2D and W/T turbulence models presented in the Sec. I and let us assess them in

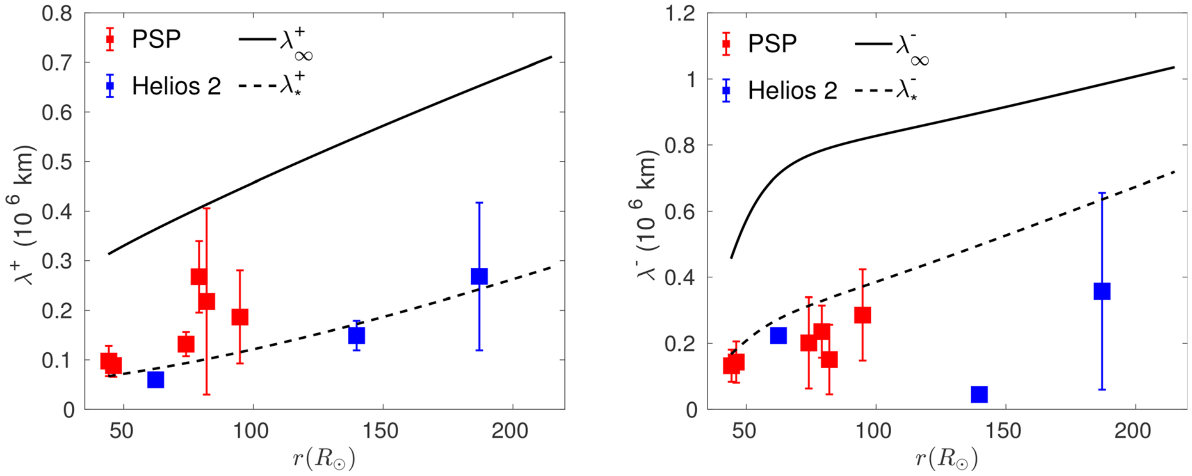

FIG. 17. Comparison between the observed (red and blue squares) and theoretical (solid and dashed curves) correlation lengths as a function of heliocentric distance. Left: the correlation length of forward propagating modes. Right: the correlation length of backward propagating modes. The solid curve refers to the quasi-2D component and the dashed to the NI/slab component. Reproduced with permission from Adhikari *et al.*, Astron. Astrophys. **650**, A16 (2021).[119] Copyright 2021 EDP Sciences.

light of the discussion presented above. We remind the reader that observations of waves and structures in the solar wind and corona is inevitably complicated by the relative alignment of the mean flow and magnetic field and the predictions and comparison of observations apply to the super-Alfvénic solar wind.

PREDICTION 1

The NI quasi-2D model predicts that the energy-containing range in both the slow wind and fast wind is a superposition of a majority quasi-2D component and a minority slab component, likely in the ratio of 80:20. The W/T model predicts that the turbulence in the energy-containing range is primarily slab with a minority 2D component generated by the interaction of counterpropagating Alfvén waves for both the fast and slow wind. Zhao *et al.*[9,96] identify small-scale flux ropes in the slow solar wind and near the heliospheric current sheet together with Alfvén waves. The magnetic fluctuation spectra in these regions depend on many parameters, such as radial distance, the alignment between solar wind flow and magnetic field, cross helicity, etc. For highly imbalanced turbulence, a Kolmogorov-like spectrum can be found. As discussed in Sec. III A 1 and Adhikari *et al.*,[132] Solar Orbiter magnetometer and SWA–PAS plasma data during the period July 7, 2020–August 31, 2020 reveal a clear dependence on the alignment of the solar wind flow such that the magnetic field and that the 2D advected component strongly dominates the slab component for forward/backward Elsässer energies, and magnetic and kinetic energy densities in both fast and slow wind intervals. Further support for the dominant 2D-minority slab superposition model comes from comparisons of the NI MHD energy-containing models of turbulent transport to the PSP plasma and magnetic field measurements made by Adhikari *et al.*[40,118,119] For the slow wind, in regions where the flow and magnetic field are not aligned, they find that the observed forward and backward Elsässer energy densities and the total energy density compare well with the predicted dominant quasi-2D energy densities as a function of heliocentric distance. The resulting dissipation of the dominant 2D turbulence

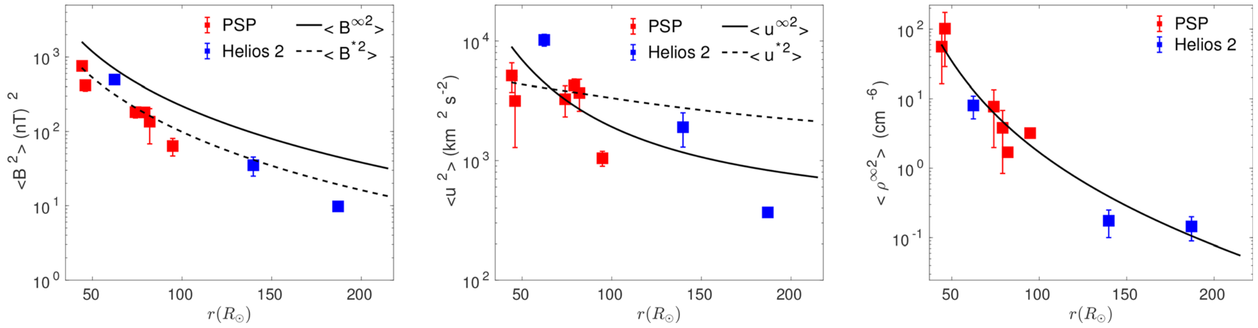

FIG. 18. Comparison between the observed (red and blue squares) and theoretical (solid and dashed curves) (left) fluctuating magnetic field variance, (center) fluctuating kinetic energy, and (right) fluctuating density variance as a function of heliocentric distance. The solid curve refers to the quasi-2D component and the dashed to the NI/slab component in the left and center figures. Reproduced with permission from Adhikari *et al.*, Astron. Astrophys. **650**, A16 (2021).[119] Copyright 2021 EDP Sciences.

is sufficient to account well for the observed heliocentric distance dependence of the plasma temperature. The corresponding observed energy densities in the magnetic field variance and the kinetic energy are also consistent with the predictions of the slow solar wind model. The various correlation lengths inferred from PSP observations are consistent too with the slow wind turbulence transport model results. For the fast solar wind in highly magnetic field aligned regions, the observed PSP energy densities (forward and backward Elsässer and total energies) are consistent with the slab energies of Adhikari *et al.*[40] and not with the predicted dominant or majority quasi-2D predictions. This is consistent with the point made repeatedly here which is that 2D fluctuations cannot be measured in a field-aligned flow unlike the Alfvénic or slab component. Hence, the quasi-2D model correctly predicts the evolution with heliocentric distance of the observed minority slab component. The incorporation of the dissipative heating associated primarily with the majority 2D component yields consistent evolution of the mean plasma radial velocity, temperature, density, and entropy. In summary, the building blocks (observed small-scale magnetic flux ropes and Alfvén waves and dominance of the 2D component over the slab component) of the NI quasi-2D turbulence description are present, and SolO and PSP observations of the heliocentric dependence and levels of the Elsässer and total energy densities in the slow and fast wind are consistent with the predictions of the NI quasi-2D energy-containing turbulence transport models. The observed energy decomposition in the energy-containing range does not meet the predictions of the W/T model.

PREDICTION 2

The NI quasi-2D model predicts that the inertial range is similarly anisotropic in both the slow and fast wind with a corresponding majority quasi-2D component and a minority slab component. The W/T model predicts that the inertial range is either isotropic or possibly possesses a Goldreich–Sridhar scaling.[72] Essentially, the same conclusions as in Prediction 1 hold for this prediction.

PREDICTION 3

The NI quasi-2D model predicts an arbitrary (normalized) cross-helicity for both the majority and minority component in both the slow and fast wind. For highly field-aligned flows, whether in the fast wind or the slow wind, it is possible that uni-directional (i.e., with high normalized cross-helicity values $|\sigma_c| \simeq 1$) Alfvén wave/slab propagation exhibiting a $k_\parallel^{-5/3}$ spectrum can occur. The W/T model predicts that the cross helicity for both fast and slow wind is small since counterpropagating Alfvén waves are essential to ensure the turbulent cascade of energy to small scales, and uni-directional Alfvén/slab propagation with a $k_\parallel^{-5/3}$ spectrum is not possible unless close to and just above the Alfvén critical surface. In the context of the W/T model, if the cross helicity is not small in the super-Alfvénic solar wind, then the fluctuations would correspond to a superposition of linear (noninteracting) Alfvén waves. It is possible that the spectrum of linear Alfvén waves would then evolve further through their resonant interaction with ions, for which quasi-linear theory predicts a k^{-2} spectrum. The analysis by Adhikari *et al.*[40,118,119,132] distinguishes between the cross helicity of the 2D and slab fluctuations. Good agreement is found between observed values of the normalized cross helicity and the predicted quasi-2D normalized cross helicity σ_c^∞ in nonaligned solar wind flow and magnetic field regions. Similarly, good agreement is found between observed values of the normalized cross helicity and the predicted slab normalized cross helicity σ_c^* in aligned solar wind flow and magnetic field regions. Zhao *et al.*[9] using PSP (slow wind) and Telloni *et al.*[8] using wind data (fast wind) observed uni-directionally propagating Alfvén waves ($|\sigma_c| \simeq 1$) with a $k_\parallel^{-5/3}$ spectrum in highly flow-magnetic field aligned intervals. This is inconsistent with the critical balance theory but is consistent with the NI MHD quasi-2D model and the spectral theory presented by Zank *et al.*[19] that shows that slab turbulence with $|\sigma_c^*| \sim 1$ possesses a Kolmogorov spectrum in the parallel wave number $k_\parallel^{-5/3}$. In nonaligned flow-magnetic field intervals, the normalized cross helicity can assume values quite different from ±1 or 0 and evolves with heliocentric distance in both the fast and slow solar wind.

PREDICTION 4

The NI quasi-2D model predicts arbitrary values of the (normalized) residual energy $\sigma_{r,}$ but it tends to evolve toward -1 in nonaligned flow-magnetic field regions, i.e., magnetic energy dominated, in the majority 2D component. The W/T model predicts that the residual energy for both the fast and slow solar wind should be close to zero since the turbulence is primarily slab. In the slow solar wind, PSP observations show that the normalized residual energy becomes increasingly negative with increasing heliocentric distance, i.e., becoming magnetic energy-dominated with distance. Because the slow wind is not typically aligned with large-scale magnetic field, the quasi-2D fluctuations are visible to the PSP. By contrast, fast solar wind flows observed by PSP are more often closely aligned with the interplanetary magnetic field than are slow flows and the normalized residual energy is typically close to 0, consistent with slab turbulence composed either of counter-propagating or uni-directionally propagating Alfvén waves. Both the slow and fast solar wind observations of the normalized residual energy are consistent with the majority 2D-minority slab NI MHD description and only the fast solar wind observations of the normalized residual energy are consistent with the W/T description.

PREDICTION 5

The NI quasi-2D model predicts that the density fluctuations are primarily advected entropy fluctuations that behave as a passive scalar (a slow and fast mode wave contribution enters only at the higher order) and have an amplitude that is ordered roughly by the turbulent Mach number $M \equiv \delta u / C_s$, where δu is a characteristic velocity of the turbulent fluctuations and C_s

is the characteristic sound speed, and that the density variance spectrum is $k^{-5/3}$. The W/T model does not include a description of density fluctuations. Histograms of density fluctuations and their linear scaling with the turbulent Mach number, both derived from PSP plasma observations, are consistent with the NI MHD superposition interpretation. A detailed discussion of the density variance spectra using PSP data has not yet been presented for the slow and fast solar wind. However, detailed comparisons of the evolving density variance based on PSP observations and an NI MHD quasi-2D model have been presented for the slow and fast wind, finding good agreement with both.[118]

In view of the convergence of the predictions listed above for a dominant quasi-2D—minority slab superposition NI MHD turbulence description and the observations being made by Parker Solar Probe and Solar Orbiter, a promising case can be made that this is the fundamental description of low-frequency turbulence in the inner heliosphere and quite possibly the corona as well.

ACKNOWLEDGMENTS

We acknowledge the partial support of an NSF EPSCoR RII-Track-1 Cooperative Agreement No. OIA-1655280, partial support from a NASA Parker Solar Probe Contract No. SV4–84017, partial support from a NASA LWS Grant No. 80NSSC20K1783, and partial support from a NASA IMAP subaward under NASA Contract No. 80GSFC19C0027. Parker Solar Probe was designed, built, and is now operated by the Johns Hopkins Applied Physics Laboratory as part of NASA's Living with a Star (LWS) program (Contract No. NNN06AA01C). Support from the LWS management and technical team has played a critical role in the success of the Parker Solar Probe mission.

DATA AVAILABILITY

The data that support the findings of this study are openly available in NASA CDAWEB: https://cdaweb.gsfc.nasa.gov/index.html/, Parker Solar Probe Science Gateway: Refs. 1–3 https://sppgway.jhuapl.edu/, and Solar Orbiter Archive: Refs. 133 and 134 http://soar.esac.esa.int/soar/#home.

REFERENCES

[1] N. J. Fox, M. C. Velli, S. D. Bale, R. Decker, A. Driesman, R. A. Howard, J. C. Kasper, J. Kinnison, M. Kusterer, D. Lario, M. K. Lockwood, D. J. McComas, N. E. Raouafi, and A. Szabo, "The Solar Probe Plus mission: Humanity's first visit to our star," Space Sci. Rev. **204**, 7–48 (2016).

[2] S. D. Bale, K. Goetz, P. R. Harvey, P. Turin, J. W. Bonnell, T. Dudok de Wit, R. E. Ergun, R. J. MacDowall, M. Pulupa, M. Andre, M. Bolton, J. L. Bougeret, T. A. Bowen, D. Burgess, C. A. Cattell, B. D. G. Chandran, C. C. Chaston, C. H. K. Chen, M. K. Choi, J. E. Connerney, S. Cranmer, M. Diaz-Aguado, W. Donakowski, J. F. Drake, W. M. Farrell, P. Fergeau, J. Fermin, J. Fischer, N. Fox, D. Glaser, M. Goldstein, D. Gordon, E. Hanson, S. E. Harris, L. M. Hayes, J. J. Hinze, J. V. Hollweg, T. S. Horbury, R. A. Howard, V. Hoxie, G. Jannet, M. Karlsson, J. C. Kasper, P. J. Kellogg, M. Kien, J. A. Klimchuk, V. V. Krasnoselskikh, S. Krucker, J. J. Lynch, M. Maksimovic, D. M. Malaspina, S. Marker, P. Martin, J. Martinez-Oliveros, J. McCauley, D. J. McComas, T. McDonald, N. Meyer-Vernet, M. Moncuquet, S. J. Monson, F. S. Mozer, S. D. Murphy, J. Odom, R. Oliverson, J. Olson, E. N. Parker, D. Pankow, T. Phan, E. Quataert, T. Quinn, S. W. Ruplin, C. Salem, D. Seitz, D. A. Sheppard, A. Siy, K. Stevens, D. Summers, A. Szabo, M. Timofeeva, A. Vaivads, M. Velli, A. Yehle, D. Werthimer, and J. R. Wygant, "The FIELDS instrument suite for solar probe plus. Measuring the coronal plasma and magnetic field, plasma waves and turbulence, and radio signatures of solar transients," Space Sci. Rev. **204**, 49–82 (2016).

[3] J. C. Kasper, R. Abiad, G. Austin, M. Balat-Pichelin, S. D. Bale, J. W. Belcher, P. Berg, H. Bergner, M. Berthomier, J. Bookbinder, E. Brodu, D. Caldwell, A. W. Case, B. D. G. Chand ran, P. Cheimets, J. W. Cirtain, S. R. Cranmer, D. W. Curtis, P. Daigneau, G. Dalton, B. Dasgupta, D. DeTomaso, M. Diaz-Aguado, B. Djordjevic, B. Donaskowski, M. Effinger, V. Florinski, N. Fox, M. Freeman, D. Gallagher, S. P. Gary, T. Gauron, R. Gates, M. Goldstein, L. Golub, D. A. Gordon, R. Gurnee, G. Guth, J. Halekas, K. Hatch, J. Heerikuisen, G. Ho, Q. Hu, G. Johnson, S. P. Jordan, K. E. Korreck, D. Larson, A. J. Lazarus, G. Li, R. Livi, M. Ludlam, M. Maksimovic, J. P. McFadden, W. Marchant, B. A. Maruca, D. J. McComas, L. Messina, T. Mercer, S. Park, A. M. Peddie, N. Pogorelov, M. J. Reinhart, J. D. Richardson, M. Robinson, I. Rosen, R. M. Skoug, A. Slagle, J. T. Steinberg, M. L. Stevens, A. Szabo, E. R. Taylor, C. Tiu, P. Turin, M. Velli, G. Webb, P. Whittlesey, K. Wright, S. T. Wu, and G. Zank, "Solar wind electrons alphas and protons (SWEAP) investigation: Design of the solar wind and coronal plasma instrument suite for solar probe plus," Space Sci. Rev. **204**, 131–186 (2016).

[4] S. D. Bale, S. T. Badman, J. W. Bonnell, T. A. Bowen, D. Burgess, A. W. Case, C. A. Cattell, B. D. G. Chandran, C. C. Chaston, C. H. K. Chen, J. F. Drake, T. D. de Wit, J. P. Eastwood, R. E. Ergun, W. M. Farrell, C. Fong, K. Goetz, M. Goldstein, K. A. Goodrich, P. R. Harvey, T. S. Horbury, G. G. Howes, J. C. Kasper, P. J. Kellogg, J. A. Klimchuk, K. E. Korreck, V. V. Krasnoselskikh, S. Krucker, R. Laker, D. E. Larson, R. J. MacDowall, M. Maksimovic, D. M. Malaspina, J. Martinez-Oliveros, D. J. McComas, N. Meyer-Vernet, M. Moncuquet, F. S. Mozer, T. D. Phan, M. Pulupa, N. E. Raouafi, C. Salem, D. Stansby, M. Stevens, A. Szabo, M. Velli, T. Woolley, and J. R. Wygant, "Highly structured slow solar wind emerging from an equatorial coronal hole," Nature **576**, 237–242 (2019).

[5] J. C. Kasper, S. D. Bale, J. W. Belcher, M. Berthomier, A. W. Case, B. D. G. Chandran, D. W. Curtis, D. Gallagher, S. P. Gary, L. Golub, J. S. Halekas, G. C. Ho, T. S. Horbury, Q. Hu, J. Huang, K. G. Klein, K. E. Korreck, D. E. Larson, R. Livi, B. Maruca, B. Lavraud, P. Louarn, M. Maksimovic, M. Martinovic, D. McGinnis, N. V. Pogorelov, J. D. Richardson, R. M. Skoug, J. T. Steinberg, M. L. Stevens, A. Szabo, M. Velli, P. L. Whittlesey, K. H. Wright, G. P. Zank, R. J. MacDowall, D. J. McComas, R. L. McNutt, M. Pulupa, N. E. Raouafi, and N. A. Schwadron, "Alfvénic velocity spikes and rotational flows in the near-Sun solar wind," Nature **576**, 228–231 (2019).

[6] S. R. Cranmer and A. A. van Ballegooijen, "Can the solar wind be driven by magnetic reconnection in the Sun's magnetic carpet?," Astrophys. J. **720**, 824–847 (2010).

[7] X. Wang, C. Tu, J. He, E. Marsch, L. Wang, and C. Salem, "The spectral features of low-amplitude magnetic fluctuations in the solar wind and their comparison with moderate-amplitude fluctuations," Astrophys. J. **810**, L21 (2015).

[8] D. Telloni, F. Carbone, R. Bruno, L. Sorriso-Valvo, G. P. Zank, L. Adhikari, and P. Hunana, "No evidence for critical balance in field-aligned alfvenic solar wind turbulence," Astrophys. J. **887**, 160 (2019).

[9] L. L. Zhao, G. P. Zank, L. Adhikari, M. Nakanotani, D. Telloni, and F. Carbone, "Spectral features in field-aligned solar wind turbulence from Parker Solar Probe observations," Astrophys. J. **898**, 113 (2020).

[10] W. H. Matthaeus, G. P. Zank, S. Oughton, D. J. Mullan, and P. Dmitruk, "Coronal heating by magnetohydrodynamic turbulence driven by reflected low-frequency waves," Astrophys. J. Lett. **523**, L93–L96 (1999).

[11] H. Alfvén and C. G. Fält hammer, *Cosmical Electrodynamics*, 2nd ed. (Clarendon, Oxford, England, 1963), Vol. 877.

[12] C. A. Ferraro and C. Plumpton, "Hydromagnetic waves in a horizontally stratified atmosphere, V," Astrophys. J. **127**, 459 (1958).

[13] J. F. McKenzie, M. Banaszkiewicz, and W. I. Axford, "Acceleration of the high speed solar wind," Astron. Astrophys. **303**, L45 (1995).

[14] D. Mullan, *Physics of the Sun* (CRC Press, 2009).

[15] A. M. Title and C. J. Schrijver, "The Sun's magnetic carpet," in *Cool Stars, Stellar Systems, and the Sun*, Astronomical Society of the Pacific Conference Series Vol. 154, edited by R. A. Donahue and J. A. Bookbinder (ASP, 1998), p. 345.

[16] A. F. Rappazzo and E. N. Parker, "Current sheets formation in tangled coronal magnetic fields," Astrophys. J. Lett. **773**, L2 (2013).

[17] G. P. Zank, L. Adhikari, P. Hunana, S. K. Tiwari, R. Moore, D. Shiota, R. Bruno, and D. Telloni, "Theory and transport of nearly incompressible magnetohydrodynamic turbulence. IV. Solar coronal turbulence," Astrophys. J. **854**, 32 (2018).

[18] G. P. Zank, L. Adhikari, P. Hunana, D. Shiota, R. Bruno, and D. Telloni, "Theory and transport of nearly incompressible magnetohydrodynamic turbulence," Astrophys. J. **835**, 147 (2017).

[19] G. P. Zank, M. Nakanotani, L. L. Zhao, L. Adhikari, and D. Telloni, "Spectral anisotropy in 2D plus slab magnetohydrodynamic turbulence in the solar wind and upper corona," Astrophys. J. **900**, 115 (2020).

[20] B. De Pontieu, S. W. McIntosh, M. Carlsson, V. H. Hansteen, T. D. Tarbell, C. J. Schrijver, A. M. Title, R. A. Shine, S. Tsuneta, Y. Katsukawa, K. Ichimoto, Y. Suematsu, T. Shimizu, and S. Nagata, "Chromospheric Alfvénic waves strong enough to power the solar wind," Science **318**, 1574 (2007).

[21] R. Erdélyi and V. Fedun, "Are there Alfvén waves in the solar atmosphere?," Science **318**, 1572 (2007).

[22] S. Tomczyk, S. W. McIntosh, S. L. Keil, P. G. Judge, T. Schad, D. H. Seeley, and J. Edmondson, "Alfvén waves in the solar corona," Science **317**, 1192 (2007).

[23] J. W. Cirtain, L. Golub, L. Lundquist, A. van Ballegooijen, A. Savcheva, M. Shimojo, E. DeLuca, S. Tsuneta, T. Sakao, K. Reeves, M. Weber, R. Kano, N. Narukage, and K. Shibasaki, "Evidence for Alfvén waves in solar x-ray jets," Science **318**, 1580 (2007).

[24] S. Tomczyk and S. W. McIntosh, "Time-distance seismology of the solar corona with CoMP," Astrophys. J. **697**, 1384–1391 (2009).

[25] G. Verth, M. Goossens, and J.-S. He, "Magnetoseismological determination of magnetic field and plasma density height variation in a solar spicule," Astrophys. J. Lett. **733**, L15 (2011).

[26] T. J. Okamoto and B. D. Pontieu, "Propagating waves along spicules," Astrophys. J. Lett. **736**, L24 (2011).

[27] D. Kuridze, R. J. Morton, R. Erdélyi, G. D. Dorrian, M. Mathioudakis, D. B. Jess, and F. P. Keenan, "Transverse oscillations in chromospheric mottles," Astrophys. J. **750**, 51 (2012).

[28] T. V. Zaqarashvili and R. Erdélyi, "Oscillations and waves in solar spicules," Space Sci. Rev. **149**, 355–388 (2009).

[29] M. Mathioudakis, D. B. Jess, and R. Erdélyi, "Alfvén waves in the solar atmosphere. From theory to observations," Space Sci. Rev. **175**, 1–27 (2013).

[30] T. Van Doorsselaere, V. M. Nakariakov, P. R. Young, and E. Verwichte, "Coronal magnetic field measurement using loop oscillations observed by Hinode/EIS," Astron. Astrophys. **487**, L17–L20 (2008).

[31] S. W. McIntosh, B. de Pontieu, M. Carlsson, V. Hansteen, P. Boerner, and M. Goossens, "Alfvénic waves with sufficient energy to power the quiet solar corona and fast solar wind," Nature **475**, 477–480 (2011).

[32] R. J. Morton and J. A. McLaughlin, "Hi-C and AIA observations of transverse magnetohydrodynamic waves in active regions," Astron. Astrophys. **553**, L10 (2013).

[33] G. Nisticò, V. M. Nakariakov, and E. Verwichte, "Decaying and decayless transverse oscillations of a coronal loop," Astron. Astrophys. **552**, A57 (2013).

[34] J. O. Thurgood, R. J. Morton, and J. A. McLaughlin, "First direct measurements of transverse waves in solar polar plumes using SDO/AIA," Astrophys. J. Lett. **790**, L2 (2014).

[35] R. J. Morton, S. Tomczyk, and R. F. Pinto, "A global view of velocity fluctuations in the corona below 1.3 $R_\odot$ with CoMP," Astrophys. J. **828**, 89 (2016).

[36] M. Velli, "On the propagation of ideal, linear Alfven waves in radially stratified stellar atmospheres and winds," Astron. Astrophys. **270**, 304–314 (1993).

[37] G. L. Withbroe, "The temperature structure, mass, and energy flow in the corona and inner solar wind," Astrophys. J. **325**, 442 (1988).

[38] R. L. Moore, A. C. Sterling, and D. A. Falconer, "Magnetic untwisting in solar jets that go into the outer corona in polar coronal holes," Astrophys. J. **806**, 11 (2015).

[39] One might speculate on how turbulence might be advected across the transition layer. Transition region spectral lines show redshifts for lines formed in the temperature range of $\sim$10 000 K to about 2.5×10^5 K. At higher temperatures, the lines are often observed to be blueshifted. An interesting set of simulations by Zacharias *et al.*[162] finds that although most of the transition region mass is cooling, the blueshifts seem to be due to both a higher percentage of upflowing mass in the upper transition region and stronger upflows than downflows. To avoid the corona "draining," upflows across the transition are clearly necessary. The upflowing material has to be heated and the process by which that happens is not yet understood. It is possible that the mechanism for producing quasi-2D turbulence through the interaction of Alfvén waves with the transition region described above will lead to the kind of heating necessary to produce the observed upflows, but we stress, this is speculative. The key point is that upflows do exist, are difficult to observe, but can be simulated. In this sense, the advection of quasi-2D turbulence across the transition region into the low corona might occur.

[40] L. Adhikari, G. P. Zank, and L. L. Zhao, "A solar coronal hole and fast solar wind turbulence model and first-orbit Parker Solar Probe (PSP) observations," Astrophys. J. **901**, 102 (2020).

[41] D. Telloni, E. Antonucci, and M. A. Dodero, "Oxygen temperature anisotropy and solar wind heating above coronal holes out to 5 $R_\odot$," Astron. Astrophys. **476**, 1341–1346 (2007).

[42] D. Telloni, S. Giordano, and E. Antonucci, "On the fast solar wind heating and acceleration processes: A statistical study based on the UVCS survey data," Astrophys. J. Lett. **881**, L36 (2019).

[43] S. Oughton, W. H. Matthaeus, P. Dmitruk, L. J. Milano, G. P. Zank, and D. J. Mullan, "A reduced magnetohydrodynamic model of coronal heating in open magnetic regions driven by reflected low-frequency Alfvén waves," Astrophys. J. **551**, 565–575 (2001).

[44] P. Dmitruk, L. J. Milano, and W. H. Matthaeus, "Wave-driven turbulent coronal heating in open field line regions: Nonlinear phenomenological model," Astrophys. J. **548**, 482–491 (2001).

[45] P. Dmitruk, W. H. Matthaeus, L. J. Milano, S. Oughton, G. P. Zank, and D. J. Mullan, "Coronal heating distribution due to low-frequency, wave-driven turbulence," Astrophys. J. **575**, 571–577 (2002), astro-ph/0204347.

[46] T. K. Suzuki and S.-I. Inutsuka, "Making the corona and the fast solar wind: A self-consistent simulation for the low-frequency Alfvén waves from the photosphere to 0.3 AU," Astrophys. J. Lett. **632**, L49–L52 (2005).

[47] S. R. Cranmer, A. A. van Ballegooijen, and R. J. Edgar, "Self-consistent coronal heating and solar wind acceleration from anisotropic magnetohydrodynamic turbulence," Astrophys. J. Suppl. Ser. **171**, 520–551 (2007).

[48] S. R. Cranmer, A. A. van Ballegooijen, and L. N. Woolsey, "Connecting the Sun's high-resolution magnetic carpet to the turbulent heliosphere," Astrophys. J. **767**, 125 (2013).

[49] Y.-M. Wang, Y.-K. Ko, and R. Grappin, "Slow solar wind from open regions with strong low-coronal heating," Astrophys. J. **691**, 760–769 (2009).

[50] B. D. G. Chandran and J. V. Hollweg, "Alfvén wave reflection and turbulent heating in the solar wind from 1 solar radius to 1 AU: An analytical treatment," Astrophys. J. **707**, 1659–1667 (2009).

[51] A. Verdini, M. Velli, W. H. Matthaeus, S. Oughton, and P. Dmitruk, "A turbulence-driven model for heating and acceleration of the fast wind in coronal holes," Astrophys. J. Lett. **708**, L116–L120 (2010).

[52] T. Matsumoto and K. Shibata, "Nonlinear propagation of Alfvén waves driven by observed photospheric motions: Application to the coronal heating and spicule formation," Astrophys. J. **710**, 1857–1867 (2010).

[53] B. D. G. Chandran, T. J. Dennis, E. Quataert, and S. D. Bale, "Incorporating kinetic physics into a two-fluid solar-wind model with temperature anisotropy and low-frequency Alfvén-wave turbulence," Astrophys. J. **743**, 197 (2011).

[54] A. V. Usmanov, W. H. Matthaeus, B. A. Breech, and M. L. Goldstein, "Solar wind modeling with turbulence transport and heating," Astrophys. J. **727**, 84 (2011).

[55] R. Lionello, M. Velli, C. Downs, J. A. Linker, Z. Mikić, and A. Verdini, "Validating a time-dependent turbulence-driven model of the solar wind," Astrophys. J. **784**, 120 (2014).

[56] A. V. Usmanov, M. L. Goldstein, and W. H. Matthaeus, "Three-fluid, three-dimensional magnetohydrodynamic solar wind model with eddy viscosity and turbulent resistivity," Astrophys. J. **788**, 43 (2014).

[57] L. N. Woolsey and S. R. Cranmer, "Turbulence-driven coronal heating and improvements to empirical forecasting of the solar wind," Astrophys. J. **787**, 160 (2014).

[58] J. V. Shebalin, W. H. Matthaeus, and D. Montgomery, "Anisotropy in MHD turbulence due to a mean magnetic field," J. Plasma Phys. **29**, 525–547 (1983).
[59] L. A. Fisk, N. A. Schwadron, and T. H. Zurbuchen, "Acceleration of the fast solar wind by the emergence of new magnetic flux," J. Geophys. Res. **104**, 19765–19772, https://doi.org/10.1029/1999JA900256 (1999).
[60] L. A. Fisk, "Acceleration of the solar wind as a result of the reconnection of open magnetic flux with coronal loops," J. Geophys. Res. **108**, 1157, https://doi.org/10.1029/2002JA009284 (2003).
[61] R. D'Amicis, L. Matteini, and R. Bruno, "On the slow solar wind with high Alfvénicity: From composition and microphysics to spectral properties," Mon. Not. R. Astron. Soc. **483**, 4665–4677 (2019).
[62] G. Nigro, F. Malara, V. Carbone, and P. Veltri, "Nanoflares and MHD turbulence in coronal loops: A hybrid shell model," Phys. Rev. Lett. **92**, 194501 (2004).
[63] G. Nigro, F. Malara, and P. Veltri, "Resonant behavior and fluctuating energy storage in coronal loops," Astrophys. J. **685**, 606–621 (2008).
[64] R. D'Amicis, R. Bruno, and B. Bavassano, "Response of the geomagnetic activity to solar wind turbulence during solar cycle 23," J. Atmos. Sol.-Terr. Phys. **73**, 653–657 (2011).
[65] L. Matteini, T. S. Horbury, M. Neugebauer, and B. E. Goldstein, "Dependence of solar wind speed on the local magnetic field orientation: Role of Alfvénic fluctuations," Geophys. Res. Lett. **41**, 259–265, https://doi.org/10.1002/2013GL058482 (2014).
[66] L. Matteini, T. S. Horbury, F. Pantellini, M. Velli, and S. J. Schwartz, "Ion kinetic energy conservation and magnetic field strength constancy in multi-fluid solar wind Alfvénic turbulence," Astrophys. J. **802**, 11 (2015).
[67] L. Adhikari, G. P. Zank, and L. L. Zhao, "Does turbulence turn off at the Alfvén critical surface?," Astrophys. J. **876**, 26 (2019).
[68] M. Dobrowolny, A. Mangeney, and P. Veltri, "Fully developed anisotropic hydromagnetic turbulence in interplanetary space," Phys. Rev. Lett. **45**, 144–147 (1980).
[69] M. Dobrowolny, A. Mangeney, and P. Veltri, "Properties of magnetohydrodynamic turbulence in the solar wind," Astron. Astrophys. **83**, 26–32 (1980).
[70] G. P. Zank, A. Dosch, P. Hunana, V. Florinski, W. H. Matthaeus, and G. M. Webb, "The transport of low-frequency turbulence in astrophysical flows. I. Governing equations," Astrophys. J. **745**, 35 (2012).
[71] L. L. Williams and G. P. Zank, "Effect of magnetic field geometry on the wave signature of the pickup of interstellar neutrals," J. Geophys. Res. **99**, 19229, https://doi.org/10.1029/94JA01657 (1994).
[72] P. Goldreich and S. Sridhar, "Toward a theory of interstellar turbulence. 2: Strong alfvenic turbulence," Astrophys. J. **438**, 763–775 (1995).
[73] Y. Lithwick and P. Goldreich, "Compressible magnetohydrodynamic turbulence in interstellar plasmas," Astrophys. J. **562**, 279–296 (2001).
[74] R. J. Leamon, W. H. Matthaeus, C. W. Smith, G. P. Zank, D. J. Mullan, and S. Oughton, "MHD-driven kinetic dissipation in the solar wind and corona," Astrophys. J. **537**, 1054–1062 (2000).
[75] S. R. Cranmer, "Ion cyclotron wave dissipation in the solar corona: The summed effect of more than 2000 ion species," Astrophys. J. **532**, 1197–1208 (2000).
[76] J. L. Kohl, G. Noci, S. R. Cranmer, and J. C. Raymond, "Ultraviolet spectroscopy of the extended solar corona," Astron. Astrophs. Rev. **13**, 31–157 (2006).
[77] W. I. Axford and J. F. McKenzie, "The solar wind," in *Cosmic Winds and the Heliosphere*, edited by J. R. Jokipii, C. P. Sonett, and M. S. Giampapa (University of Arizona Press, 1997), p. 31.
[78] R. Bruno and L. Trenchi, "Radial dependence of the frequency break between fluid and kinetic scales in the solar wind fluctuations," Astrophys. J. Lett. **787**, L24 (2014).
[79] D. Telloni, F. Carbone, R. Bruno, G. P. Zank, L. Sorriso-Valvo, and S. Mancuso, "Ion cyclotron waves in field-aligned solar wind turbulence," Astrophys. J. Lett. **885**, L5 (2019).
[80] J. V. Hollweg, "Kinetic Alfvén wave revisited," J. Geophys. Res. **104**, 14811–14820, https://doi.org/10.1029/1998JA900132 (1999).
[81] O. Pezzi, F. Malara, S. Servidio, F. Valentini, T. N. Parashar, W. H. Matthaeus, and P. Veltri, "Turbulence generation during the head-on collision of Alfvénic wave packets," Phys. Rev. E **96**, 023201 (2017).
[82] S. D. Bale, P. J. Kellogg, F. S. Mozer, T. S. Horbury, and H. Reme, "Measurement of the electric fluctuation spectrum of magnetohydrodynamic turbulence," Phys. Rev. Lett. **94**, 215002 (2005).
[83] F. Malara, G. Nigro, F. Valentini, and L. Sorriso-Valvo, "Electron heating by kinetic Alfvén waves in coronal loop turbulence," Astrophys. J. **871**, 66 (2019).
[84] During the first PSP encounter, the ratio of the solar wind speed to the Alfvén speed was $U/V_A \sim 3$–4, indicating that Taylor's hypothesis is reasonable, although perhaps marginally so. During the fourth orbit, the ratio U/V_A near the fourth perihelion is around 2 to 4—see Fig. 2.
[85] G. I. Taylor, "The spectrum of turbulence," Proc. R. Soc. London, Ser. A **164**, 476–490 (1938).
[86] J. Zheng and Q. Hu, "Observational evidence for self-generation of small-scale magnetic flux ropes from intermittent solar wind turbulence," Astrophys. J. Lett. **852**, L23 (2018).
[87] K. G. Klein, J. C. Perez, D. Verscharen, A. Mallet, and B. D. Chandran, "A modified version of Taylor's hypothesis for solar probe plus observations," Astrophys. J. **801**, L18 (2015).
[88] C. Chen, S. Bale, J. Bonnell, D. Borovikov, T. Bowen, D. Burgess, A. Case, B. Chandran, T. D. de Wit, K. Goetz *et al.*, "The evolution and role of solar wind turbulence in the inner heliosphere," Astrophys. J. Suppl. Ser. **246**, 53 (2020).
[89] L. Burlaga, E. Sittler, F. Mariani, and R. Schwenn, "Magnetic loop behind an interplanetary shock: Voyager, Helios, and IMP 8 observations," J. Geophys. Res. **86**, 6673–6684, https://doi.org/10.1029/JA086iA08p06673 (1981).
[90] M. B. Moldwin, J. L. Phillips, J. T. Gosling, E. E. Scime, D. J. McComas, S. J. Bame, A. Balogh, and R. J. Forsyth, "Ulysses observation of a noncoronal mass ejection flux rope: Evidence of interplanetary magnetic reconnection," J. Geophys. Res. **100**, 19903–19910, https://doi.org/10.1029/95JA01123 (1995).
[91] W. H. Matthaeus, M. L. Goldstein, and C. Smith, "Evaluation of magnetic helicity in homogeneous turbulence," Phys. Rev. Lett. **48**, 1256–1259 (1982).
[92] D. Telloni, R. Bruno, R. D'Amicis, E. Pietropaolo, and V. Carbone, "Wavelet analysis as a tool to localize magnetic and cross-helicity events in the solar wind," Astrophys. J. **751**, 19 (2012).
[93] D. Telloni, S. Perri, R. Bruno, V. Carbone, and R. D. Amicis, "An analysis of magnetohydrodynamic invariants of magnetic fluctuations within interplanetary flux ropes," Astrophys. J. **776**, 3 (2013).
[94] L. L. Zhao, G. P. Zank, Q. Hu, Y. Chen, L. Adhikari, J. A. leRoux, A. Cummings, E. Stone, and L. F. Burlaga, "ACR proton acceleration associated with reconnection processes beyond the heliospheric termination shock," Astrophys. J. **886**, 144 (2019).
[95] L. L. Zhao, G. P. Zank, L. Adhikari, Q. Hu, J. C. Kasper, S. D. Bale, K. E. Korreck, A. W. Case, M. Stevens, J. W. Bonnell, T. Dudok de Wit, K. Goetz, P. R. Harvey, R. J. MacDowall, D. M. Malaspina, M. Pulupa, D. E. Larson, R. Livi, P. Whittlesey, and K. G. Klein, "Identification of magnetic flux ropes from Parker Solar Probe observations during the first encounter," Astrophys. J. Suppl. Ser. **246**, 26 (2020).
[96] L. L. Zhao, G. P. Zank, Q. Hu, D. Telloni, Y. Chen, L. Adhikari, M. Nakanotani, J. C. Kasper, J. Huang, S. D. Bale, K. E. Korreck, A. W. Case, M. Stevens, J. W. Bonnell, T. Dudok de Wit, K. Goetz, P. R. Harvey, R. J. MacDowall, D. M. Malaspina, M. Pulupa, D. E. Larson, R. Livi, P. Whittlesey, K. G. Klein, and N. E. Raouafi, "Detection of small magnetic flux ropes from the third and fourth Parker Solar Probe encounters," Astron. Astrophys. **650**, A12 (2021).
[97] M. L. Cartwright and M. B. Moldwin, "Heliospheric evolution of solar wind small-scale magnetic flux ropes," J. Geophys. Res. **115**, A08102, https://doi.org/10.1029/2009JA014271 (2010).
[98] T. S. Horbury, M. Forman, and S. Oughton, "Anisotropic scaling of magnetohydrodynamic turbulence," Phys. Rev. Lett. **101**, 175005 (2008).
[99] J. Podesta, "Dependence of solar-wind power spectra on the direction of the local mean magnetic field," Astrophys. J. **698**, 986 (2009).
[100] J. A. Tessein, C. W. Smith, B. T. MacBride, W. H. Matthaeus, M. A. Forman, and J. E. Borovsky, "Spectral indices for multi-dimensional interplanetary turbulence at 1 au," Astrophys. J. **692**, 684 (2009).
[101] X. Wang, C. Tu, J. He, E. Marsch, and L. Wang, "The influence of intermittency on the spectral anisotropy of solar wind turbulence," Astrophys. J. Lett. **783**, L9 (2014).

[102] Y. Huang, F. G. Schmitt, Z. Lu, and Y. Liu, "An amplitude-frequency study of turbulent scaling intermittency using empirical mode decomposition and Hilbert spectral analysis," Europhys. Lett. **84**, 40010 (2008).

[103] C. Y. Tu, Z. Y. Pu, and F. S. Wei, "The power spectrum of interplanetary Alfvénic fluctuations: Derivation of the governing equation and its solution," J. Geophys. Res. **89**, 9695–9702, https://doi.org/10.1029/JA089iA11p09695 (1984).

[104] Y. Zhou and W. H. Matthaeus, "Models of inertial range spectra of interplanetary magnetohydrodynamic turbulence," J. Geophys. Res. **95**, 14881–14892, https://doi.org/10.1029/JA095iA09p14881 (1990).

[105] Y. Zhou and W. H. Matthaeus, "Remarks on transport theories of interplanetary fluctuations," J. Geophys. Res. **95**, 14863–14871, https://doi.org/10.1029/JA095iA09p14863 (1990).

[106] E. Marsch and C.-Y. Tu, "Dynamics of correlation functions with Elsasser variables for inhomogeneous MHD turbulence," J. Plasma Phys. **41**, 479–491 (1989).

[107] G. P. Zank, W. H. Matthaeus, and C. W. Smith, "Evolution of turbulent magnetic fluctuation power with heliospheric distance," J. Geophys. Res. **101**, 17093–17108, https://doi.org/10.1029/96JA01275 (1996).

[108] B. Breech, W. H. Matthaeus, J. Minnie, J. W. Bieber, S. Oughton, C. W. Smith, and P. A. Isenberg, "Turbulence transport throughout the heliosphere," J. Geophys. Res. **113**, A08105, https://doi.org/10.1029/2007JA012711 (2008).

[109] G. P. Zank and W. H. Matthaeus, "Waves and turbulence in the solar wind," J. Geophys. Res. **97**, 17189, https://doi.org/10.1029/92JA01734 (1992).

[110] G. P. Zank and W. H. Matthaeus, "Nearly incompressible fluids. II—Magnetohydrodynamics, turbulence, and waves," Phys. Fluids **5**, 257–273 (1993).

[111] P. Hunana and G. P. Zank, "Inhomogeneous nearly incompressible description of magnetohydrodynamic turbulence," Astrophys. J. **718**, 148–167 (2010).

[112] L. Adhikari, G. P. Zank, P. Hunana, D. Shiota, R. Bruno, Q. Hu, and D. Telloni, "II. Transport of nearly incompressible magnetohydrodynamic turbulence from 1 to 75 au," Astrophys. J. **841**, 85 (2017).

[113] G. P. Zank, L. Adhikari, L. L. Zhao, P. Mostafavi, E. J. Zirnstein, and D. J. McComas, "The pickup ion-mediated solar wind," Astrophys. J. **869**, 23 (2018).

[114] L. L. Zhao, L. Adhikari, G. P. Zank, Q. Hu, and X. S. Feng, "Cosmic ray diffusion tensor throughout the heliosphere derived from a nearly incompressible magnetohydrodynamic turbulence model," Astrophys. J. **849**, 88 (2017).

[115] L.-L. Zhao, L. Adhikari, G. P. Zank, Q. Hu, and X. S. Feng, "Influence of the solar cycle on turbulence properties and cosmic-ray diffusion," Astrophys. J. **856**, 94 (2018).

[116] E. N. Parker, "Topological dissipation and the small-scale fields in turbulent gases," Astrophys. J. **174**, 499 (1972).

[117] E. N. Parker, "Nanoflares and the solar X-ray corona," Astrophys. J. **330**, 474–479 (1988).

[118] L. Adhikari, G. P. Zank, L. L. Zhao, J. C. Kasper, K. E. Korreck, M. Stevens, A. W. Case, P. Whittlesey, D. Larson, R. Livi, and K. G. Klein, "Turbulence transport modeling and first orbit Parker Solar Probe (PSP) observations," Astrophys. J. Suppl. Ser. **246**, 38 (2020).

[119] L. Adhikari, G. P. Zank, L. L. Zhao, M. Nakanotani, and S. Tasnim, "Modeling proton and electron heating in the fast solar wind," Astron. Astrophys. **650**, A16 (2021).

[120] R. Grappin, U. Frisch, A. Pouquet, and J. Leorat, "Alfvenic fluctuations as asymptotic states of MHD turbulence," Astron. Astrophys. **105**, 6–14 (1982).

[121] R. Grappin, J. Leorat, and A. Pouquet, "Dependence of MHD turbulence spectra on the velocity field-magnetic field correlation," Astron. Astrophys. **126**, 51–58 (1983).

[122] L. Adhikari, G. P. Zank, Q. Hu, and A. Dosch, "Turbulence transport modeling of the temporal outer heliosphere," Astrophys. J. **793**, 52 (2014).

[123] L. Adhikari, G. P. Zank, R. Bruno, D. Telloni, P. Hunana, A. Dosch, R. Marino, and Q. Hu, "The transport of low-frequency turbulence in astrophysical flows. II. Solutions for the super-Alfvénic solar wind," Astrophys. J. **805**, 63 (2015).

[124] P. Hunana, G. P. Zank, and D. Shaikh, "Nearly incompressible fluids: Hydrodynamics and large scale inhomogeneity," Phys. Rev. E **74**, 026302 (2006).

[125] A. Bhattacharjee, C. S. Ng, and S. R. Spangler, "Weakly compressible magnetohydrodynamic turbulence in the solar wind and the interstellar medium," Astrophys. J. **494**, 409–418 (1998).

[126] J. W. Bieber, W. Wanner, and W. H. Matthaeus, "Dominant two-dimensional solar wind turbulence with implications for cosmic ray transport," J. Geophys. Res. **101**, 2511–2522, https://doi.org/10.1029/95JA02588 (1996).

[127] J. Saur and J. W. Bieber, "Geometry of low-frequency solar wind magnetic turbulence: Evidence for radially aligned Alfénic fluctuations," J. Geophys. Res. **104**, 9975–9988, https://doi.org/10.1029/1998JA900077 (1999).

[128] R. T. Wicks, T. S. Horbury, C. H. K. Chen, and A. A. Schekochihin, "Power and spectral index anisotropy of the entire inertial range of turbulence in the fast solar wind," Mon. Not. R. Astron. Soc. **407**, L31–L35 (2010).

[129] M. A. Forman, R. T. Wicks, and T. S. Horbury, "Detailed fit of 'critical balance' theory to solar wind turbulence measurements," Astrophys. J. **733**, 76 (2011).

[130] X. Wang, C. Tu, and J. He, "2D isotropic feature of solar wind turbulence as shown by self-correlation level contours at hour timescales," Astrophys. J. **871**, 93 (2019).

[131] Z. B. Pine, C. W. Smith, S. J. Hollick, M. R. Argall, B. J. Vasquez, P. A. Isenberg, N. A. Schwadron, C. J. Joyce, J. M. Sokół, M. Bzowski, M. A. Kubiak, K. E. Hamilton, M. L. McLaurin, and R. J. Leamon, "Solar wind turbulence from 1 to 45 au. III. Anisotropy of magnetic fluctuations in the inertial range using voyager and ace observations," Astrophys. J. **900**, 93 (2020).

[132] L. Adhikari, G. P. Zank, L. L. Zhao, D. Telloni, T. S. Horbury, H. O'Brien, V. Evans, V. Angelini, C. J. Owen, P. Louarn, and A. Fedorov, "Evolution of anisotropic turbulence in the fast and slow solar wind: Theory and solar orbiter measurements," Astron. Astrophys. (published online, 2021).

[133] T. S. Horbury, H. O'Brien, I. Carrasco Blazquez, M. Bendyk, P. Brown, R. Hudson, V. Evans, T. M. Oddy, C. M. Carr, T. J. Beek, E. Cupido, S. Bhattacharya, J. A. Dominguez, L. Matthews, V. R. Myklebust, B. Whiteside, S. D. Bale, W. Baumjohann, D. Burgess, V. Carbone, P. Cargill, J. Eastwood, G. Erdös, L. Fletcher, R. Forsyth, J. Giacalone, K. H. Glassmeier, M. L. Goldstein, T. Hoeksema, M. Lockwood, W. Magnes, M. Maksimovic, E. Marsch, W. H. Matthaeus, N. Murphy, V. M. Nakariakov, C. J. Owen, M. Owens, J. Rodriguez-Pacheco, I. Richter, P. Riley, C. T. Russell, S. Schwartz, R. Vainio, M. Velli, S. Vennerstrom, R. Walsh, R. F. Wimmer-Schweingruber, G. Zank, D. Müller, I. Zouganelis, and A. P. Walsh, "The solar orbiter magnetometer," Astron. Astrophys. **642**, A9 (2020).

[134] C. J. Owen, R. Bruno, S. Livi, P. Louarn, K. Al Janabi, F. Allegrini, C. Amoros, R. Baruah, A. Barthe, M. Berthomier, S. Bordon, C. Brockley-Blatt, C. Brysbaert, G. Capuano, M. Collier, R. DeMarco, A. Fedorov, J. Ford, V. Fortunato, I. Fratter, A. B. Galvin, B. Hancock, D. Heirtzler, D. Kataria, L. Kistler, S. T. Lepri, G. Lewis, C. Loeffler, W. Marty, R. Mathon, A. Mayall, G. Mele, K. Ogasawara, M. Orlandi, A. Pacros, E. Penou, S. Persyn, M. Petiot, M. Phillips, L. Přech, J. M. Raines, M. Reden, A. P. Rouillard, A. Rousseau, J. Rubiella, H. Seran, A. Spencer, J. W. Thomas, J. Trevino, D. Verscharen, P. Wurz, A. Alapide, L. Amoruso, N. André, C. Anekallu, V. Arciuli, K. L. Arnett, R. Ascolese, C. Bancroft, P. Bland, M. Brysch, R. Calvanese, M. Castronuovo, I. Čermák, D. Chornay, S. Clemens, J. Coker, G. Collinson, R. D'Amicis, I. Dandouras, R. Darnley, D. Davies, G. Davison, A. De Los Santos, P. Devoto, G. Dirks, E. Edlund, A. Fazakerley, M. Ferris, C. Frost, G. Fruit, C. Garat, V. Génot, W. Gibson, J. A. Gilbert, V. de Giosa, S. Gradone, M. Hailey, T. S. Horbury, T. Hunt, C. Jacquey, M. Johnson, B. Lavraud, A. Lawrenson, F. Leblanc, W. Lockhart, M. Maksimovic, A. Malpus, F. Marcucci, C. Mazelle, F. Monti, S. Myers, T. Nguyen, J. Rodriguez-Pacheco, I. Phillips, M. Popecki, K. Rees, S. A. Rogacki, K. Ruane, D. Rust, M. Salatti, J. A. Sauvaud, M. O. Stakhiv, J. Stange, T. Stubbs, T. Taylor, J. D. Techer, G. Terrier, R. Thibodeaux, C. Urdiales, A. Varsani, A. P. Walsh, G. Watson, P. Wheeler, G. Willis, R. F. Wimmer-Schweingruber, B. Winter, J. Yardley, and I. Zouganelis, "The solar orbiter solar wind analyser (SWA) suite," Astron. Astrophys. **642**, A16 (2020).

[135] J. W. Belcher and L. Davis, "Large-amplitude Alfvén waves in the interplanetary medium, 2," J. Geophys. Res. **76**, 3534, https://doi.org/10.1029/JA076i016p03534 (1971).

[136] Y. Chen, Q. Hu, L. Zhao, J. C. Kasper, S. D. Bale, K. E. Korreck, A. W. Case, M. L. Stevens, J. W. Bonnell, K. Goetz, P. R. Harvey, K. G. Klein, D. E. Larson, R. Livi, R. J. MacDowall, D. M. Malaspina, M. Pulupa, and P. L. Whittlesey, "Small-scale magnetic flux ropes in the first two Parker Solar Probe encounters," Astrophys. J. **903**, 76 (2020).

[137] L. F. Burlaga, "Micro-scale structures in the interplanetary medium," Sol. Phys. **4**, 67–92 (1968).

[138] L. F. Burlaga, *Interplanetary Magnetohydrodynamics* (Oxford University Press on Demand, 1995), Vol. 3.

[139] J. E. Borovsky, "Flux tube texture of the solar wind: Strands of the magnetic carpet at 1 AU?," J. Geophys. Res. **113**, A08110, https://doi.org/10.1029/2007JA012684 (2008).

[140] G. P. Zank, G. Li, V. Florinski, W. H. Matthaeus, G. M. Webb, and J. A. Le Roux, "Perpendicular diffusion coefficient for charged particles of arbitrary energy," J. Geophys. Res. **109**, A04107, https://doi.org/10.1029/2003JA010301 (2004).

[141] W. H. Matthaeus, G. P. Zank, C. W. Smith, and S. Oughton, "Turbulence, spatial transport, and heating of the solar wind," Phys. Rev. Lett. **82**, 3444–3447 (1999).

[142] C. W. Smith, W. H. Matthaeus, G. P. Zank, N. F. Ness, S. Oughton, and J. D. Richardson, "Heating of the low-latitude solar wind by dissipation of turbulent magnetic fluctuations," J. Geophys. Res. **106**, 8253–8272, https://doi.org/10.1029/2000JA000366 (2001).

[143] D. Ruffolo, W. H. Matthaeus, R. Chhiber, A. V. Usmanov, Y. Yang, R. Bandyopadhyay, T. N. Parashar, M. L. Goldstein, C. E. DeForest, M. Wan, A. Chasapis, B. A. Maruca, M. Velli, and J. C. Kasper, "Shear-driven transition to isotropically turbulent solar wind outside the Alfvén critical zone," Astrophys. J. **902**, 94 (2020).

[144] A. R. Barakat and R. W. Schunk, "Transport equations for multicomponent anisotropic space plasmas: A review," Plasma Phys. **24**, 389–418 (1982).

[145] G. P. Zank, *Transport Processes in Space Physics and Astrophysics*, Lecture Notes in Physics, Springer Vol. 877 (Springer-Verlag Berlin, New York, Heidelberg, Dordrecht, London, 2014).

[146] S. R. Cranmer, W. H. Matthaeus, B. A. Breech, and J. C. Kasper, "Empirical constraints on proton and electron heating in the fast solar wind," Astrophys. J. **702**, 1604–1614 (2009).

[147] B. Tang, G. P. Zank, and V. I. Kolobov, "Numerical modeling of suprathermal electron transport in the solar wind: Effects of whistler turbulence," Astrophys. J. **892**, 95 (2020).

[148] W. G. Pilipp, K. H. Muehlhaeuser, H. Miggenrieder, H. Rosenbauer, and R. Schwenn, "Large-scale variations of thermal electron parameters in the solar wind between 0.3 and 1 AU," J. Geophys. Res. **95**, 6305–6329, https://doi.org/10.1029/JA095iA05p06305 (1990).

[149] L. Spitzer and R. Härm, "Transport phenomena in a completely ionized gas," Phys. Rev. **89**, 977–981 (1953).

[150] R. J. Leamon, W. H. Matthaeus, C. W. Smith, and H. K. Wong, "Contribution of cyclotron-resonant damping to kinetic dissipation of interplanetary turbulence," Astrophys. J. Lett. **507**, L181–L184 (1998).

[151] B. Breech, W. H. Matthaeus, S. R. Cranmer, J. C. Kasper, and S. Oughton, "Electron and proton heating by solar wind turbulence," J. Geophys. Res. **114**, A09103, https://doi.org/10.1029/2009JA014354 (2009).

[152] G. G. Howes, "A prescription for the turbulent heating of astrophysical plasmas," Mon. Not. R. Astron. Soc. **409**, L104–L108 (2010).

[153] G. G. Howes, "Prediction of the proton-to-total turbulent heating in the solar wind," Astrophys. J. **738**, 40 (2011).

[154] N. E. Engelbrecht and R. D. T. Strauss, "A tractable estimate for the dissipation range onset wavenumber throughout the heliosphere," Astrophys. J. **856**, 159 (2018).

[155] A. Dosch, L. Adhikari, and G. P. Zank, "The transport of low-frequency turbulence in astrophysical flows: Correlation lengths," AIP Conf. Proc. **1539**, 155–158 (2013).

[156] D. Shiota, G. P. Zank, L. Adhikari, P. Hunana, D. Telloni, and R. Bruno, "Turbulent transport in a three-dimensional solar wind," Astrophys. J. **837**, 75 (2017).

[157] J. F. Drake, M. Swisdak, H. Che, and M. A. Shay, "Electron acceleration from contracting magnetic islands during reconnection," Nature **443**, 553–556 (2006).

[158] G. P. Zank, J. A. le Roux, G. M. Webb, A. Dosch, and O. Khabarova, "Particle acceleration via reconnection processes in the supersonic solar wind," Astrophys. J. **797**, 28 (2014).

[159] H. Che and G. P. Zank, "Electron acceleration from expanding magnetic vortices during reconnection with a guide field," Astrophys. J. **889**, 11 (2020).

[160] R. Bruno, "Inner heliosphere observations of MHD turbulence in the solar wind: Challenges to theory," in *Solar Wind Seven*, COSPAR Colloquia Series Vol. 3, edited by E. Marsch and R. Schwenn (Pergamon Press, Oxford, New York, 1992), pp. 423–428.

[161] Some care in the interpretation of the comparison is necessary because we compare models with measurements of the proton temperature and density that are not necessarily exclusively proton core distribution, possibly possessing a beam component that should be filtered. Thus, the predicted radial evolution of the temperature and density can be slightly different from that observed.

[162] P. Zacharias, V. H. Hansteen, J. Leenaarts, M. Carlsson, and B. V. Gudiksen, "Disentangling flows in the solar transition region," Astron. Astrophys. **614**, A110 (2018).